INVESTIGATION OF THE POTENTIAL APPLICATIONS OF SHAPE MEMORY ALLOYS FOR SPACE DEBRIS REMEDIATION APPLICATIONS

Louis Wei-Yu Feng

Master's Dissertation
in the Department of Electrical Engineering
Faculty of Engineering and the Built Environment
University of Cape Town

December 2017

SL17 - 04M

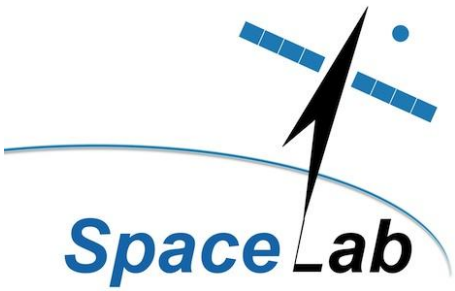

Declaration

I, Louis Wei-yu Feng, hereby:

a) grant the University of Cape Town free licence to reproduce this thesis in whole or in part, for the purpose of research;

b) declare that:

i) I know the meaning of plagiarism and declare that all the work in the document, save for that which is properly acknowledged, is my own.

ii) neither the substance nor any part of this thesis has been submitted in the past, or is being, or is to be submitted for a degree at this University or at any other university.

This thesis is presented for examination in partial fulfilment of the requirements for the degree of Master of Philosophy in Space Studies.

Signed by candidate

Louis Wei-yu Feng

November 22, 2017

Abstract

Active debris removal is becoming an important area of research due to the rapid growth of space debris and the need for some form of debris remediation. Recent studies have suggested that around five large space debris should be removed from Low Earth orbit (LEO) per year starting in 2020 in order to stabilize the space object population growth. Debris remediation concepts fall into two general categories: contact-based and contactless. Contact-based schemes for debris capture have to overcome the challenges of capturing a non-cooperating object in space with no pre-designed attachment points. Various schemes involving, inter alia, nets and harpoons have been proposed. In this research we explore the potential to use shape-memory alloys as a technological basis for a debris capturing solution that can be used multiple times. A proof-of-concept prototype named MEDUSA (Mechanism for Entrapment of Debris Using Shape memory Alloy) was designed at the University of Cape Town to capture target debris of size equivalent to a 1-U CubeSat. This prototype has been designed as a demonstration payload for a CubeSat test platform. MEDUSA uses the shape-memory alloy ninitol, which gives it the ability to assume pre-programmed "open" and "closed" shapes. Each of the five arms of MEDUSA can attain both pre-programmed shapes to allow reversible operations. This prototype lays a proof-of-concept foundation for future small-scale debris capturing devices based on shape memory alloys.

Acknowledgements

My sincere gratitude goes to:

Professor Peter Martinez for his constant support and guidance throughout this project. His positive criticisms and challenging questions motivated me to achieve what I thought was impossible.

Mr Samuel Ginsberg for all the discussions we had which led to innovative ideas for this project. The useful recommendations he provided made MEDUSA a better system.

My brother Kai-Yu Feng and Yean-Tser Hsu. A special thanks for all the assistance, care and thoughtful ideas you provided all along. I truly appreciate everything you have done for me.

Mr Brendon Daniels and Mr Justin Pead for their assistance with instrumentation, 3D printing and laser-cutting.

Dane Du Plessis, Randy Po-Kai Cheng, my old friends. I am glad and proud to have finished undergraduate and master's with you. Thank you for all the encouragement and motivation that inspired me all along this project.

Ryan Wolf, Yang Sheng and Dewald Whitelab thanks for all the assistance you provided during this project.

Michael Dropmann and Manfred Ehresmann, for their contributions towards the MEDUSA project during my time at the IRS.

Prof Georg Herdrich from the IRS for his hospitality and for accommodating me in the IRS.

To all my friends and colleagues at SpaceLab; it has been a great privilege to complete this difficult and challenging but fruitful journey with all of you. I wish you all the best for your future endeavours.

"If I have seen further than the others it is by standing upon the shoulder of a giant" - Issac Newton

Contents

List of Acronyms

A . . . . . Ampere
ADCS . . . . Attitude Determination and Control System
ADR . . . . . Active Debris Removal
AOCS . . . . Attitude and Orbital Control System
DC . . . . . Direct Current
DLR . . . . . German Aerospace Centre
ESA . . . . . European Space Agency
GNC . . . . . Guidance Navigation and Control
HDT . . . . . Heat Deflection Temperature
ISS . . . . . International Space Station
JAXA . . . . Japan Aerospace eXploration Agency
LEO . . . . . Low Earth Orbit
MATLAB . . Matrix Laboratory
MEDUSA . . Mechanism for Entrapment of Debris Using Shape memory Alloy
NiTi . . . . . Nitinol
NORAD . . . North American Aerospace Defence Command
PLA . . . . . polylactic acid
PMD . . . . . Post-Mission Disposal
POD . . . . . PicoSatellite Orbital Deployer
PWM . . . . Pulse Width Modulation
RGB . . . . . Red, Green, Blue
SMA . . . . . Shape Memory Alloy
STK . . . . . Systems Tool Kit
TRL . . . . . Technology Readiness Level
U . . . . . CubeSat Unit (10 cm $\times$ 10 cm $\times$ 10 cm)
UHF . . . . . Ultra High Frequency
UNCOPUOS United Nations Committee on the Peaceful Uses of Outer Space
V . . . . . Volts

Chapter 1

Introduction

1.1 The growing problem of orbital debris

Since the launch of first satellite "Sputnik" 1 by the USSR in 1957, more than 4800 additional launches have placed over 5000 satellites in space. However only a fraction of these satellites are in active use. At present approximately only 1000 out of 5000 satellites in orbit are operational. A rough estimation of the launched mass suggests that nearly 6000 tonnes of launched mass are currently in space, out of which only 6% are operational spacecraft, 28% are de-commissioned satellites and 66% of that 6000 tonnes of mass are fragments produced by break-ups and on-orbit collisions. Currently there are several hundred thousand pieces of space debris larger than 1 cm orbiting in low Earth orbit (LEO) imposing a serious threat to operational spacecraft. To date, there have been four documented collisions between space debris and operational spacecraft. The most recent collision was in 2009, when the active Iridium-33 satellite collided with the defunct Cosmos-2251 satellite. [1]

1.1.1 Distribution of space objects in different orbits

Currently, four main orbital regions are heavily exploited by humankind. These four regions are differentiated mainly based on their altitude: Low Earth Orbit (LEO), Medium Earth Orbit (MEO), Geostationary Orbit (GEO) and High Earth Orbit (HEO). Table 1.1 outlines the main attributes and applications of these orbital regions.

Because of the different altitude and orbital period requirements for every space mission these orbits are vital for current and future space applications. However, these orbital regions are now becoming increasingly congested, raising concerns that the long-term sustainable use of the Earth's orbital space environment is now under threat by the growing population of orbital "space debris".

Table 1.1 *Main Earth orbit types and their associated space applications.*

Zone	Popular application orbit	Altitude	Period	Primary usage	Description
LEO	Circular	100 to 2000 km	84 to 127 min	EO[a], Com[b]	Satellites at altitude lower than 160 km experience rapid orbital decay.
	Polar	Typically 700 km to 800 km	98 to 102 min	EO	Global coverage, but not continuous.
	Sun-synchronous	800 km	102 min	EO	Same solar illumination conditions on Earth's surface.
MEO	Medium Earth Orbit	1000 to 35786 km	Typically 2 hours to 12 hours	PNT[c]	GPS satellites placed at 20200km with orbiting period of 12 hours at 55° inclination.
GEO	Geo-stationary	35786 km	24 hours	EO, Com	Satellites placed in GEO are "fixed" above a given position on Earth, e.g. Weather satellites, Broadcasting.
HEO	Highly Elliptical	Perigee <1000 km and Apogee >36000 km	Varies	Com	
	Molniya	Perigee <1000 km and Apogee >36000	12 hours	Com	Primarily exploited by USSR and Russia due to apogee drift, inclination chosen to compensate for secular perturbation of orbit because of effects of non-spherical Earth.
	Highly Elliptical Geosynchronous	Perigee less <1000 km and Apogee >36000 km	24 hours	Com	Apogee dwells over a chosen area of Earth. Example: Sirius satellite radio.

[a]Earth Observation, [b]Communication, [c]Position Navigation and Timing.

1.1.2 Sources of debris

Space debris has no legal definition. Generally the term "space debris" is used to describe any non-communicative and non-cooperative man-made space object that does not serve a useful purpose and poses a threat to functioning spacecraft in orbit.

Sources of space debris can be classified into four categories:

- **Non-functional spacecraft**- These spacecraft may either have completed their operational missions or may have failed on launch or at some point during their mission.
- **Abandoned launch vehicle stages**- These are spent upper stages used to deploy spacecraft, or launch vehicle components jettisoned to deploy spacecraft. An example is a Briz-M upper stage from a launch failure in August 2011, which is still intact in orbit.
- **Mission related debris**- Debris created during a mission, such as cast-off decouplers, deployable covers or any items ejected by spacecraft during a mission.
- **Fragmentation debris**- Debris created by collisions between orbital objects or by spacecraft that have exploded in orbit. An example of this was a 20-year-old military weather satellite launched by the U.S. as part of the Defence Meteorological Satellite Program (DMSP) that exploded in orbit on the 3rd of February in 2015.

The current debris population growth in LEO is depicted in Figure 1.1. Evidently, fragmentation debris outnumbers other sources of debris. Two on-orbit incidents in 2007 and 2009 that generated rapid debris population increases are visible in Figure 1.1. The two incidents were different in nature.

- In 2007, China conducted a controversial anti-satellite (ASAT) test on its retired Fong-Yun satellite in LEO at an altitude of 865 km. This retired weather satellite was destroyed by a missile fired from Earth and resulted in the creation over 2300 pieces of space debris – the biggest amount of debris generated due to a single orbital incident up to date.
- In 2009, a collision occurred between the operational commercial satellite Iridium 33 and the defunct Russian satellite Cosmos 2251. This collision created over 1500 space debris, which further endangered future space missions operating in low Earth orbit.

Table 1.2 ranks debris into three categories based on their size, danger level and trackability [2]. Satellite operators hoping to avoid collisions with debris rely on the availability of tracking information for debris. Organisations like NORAD possess tracking capabilities and provide data on catalogued objects that is freely accessible by the general public. However, the debris monitoring facilities operated by NORAD are currently limited to tracking debris larger than 10 cm in size. This means that space debris that are less than 10 centimetres are barely trackable or not trackable at all. The non-trackable debris pose a great risk to operational space missions and space applications in the near future.

Table 1.2 *Debris trackability and potential impact effects.*

Debris Size	Estimated Population	Impact	Trackability	Danger Level
Greater than 10 cm in diameter	19,000+	Source of new debris	Trackable	Catastrophic
Between 1 to 10 cm in diameter	Several hundred thousand	"Bullets" which hit larger objects and create more debris	Potentially trackable	Dangerous. Likely to seriously disrupt ongoing mission.
Less than 1 cm in diameter	Millions	Threat to active satellites	Untrackable	Bearable. Mission may be impaired.

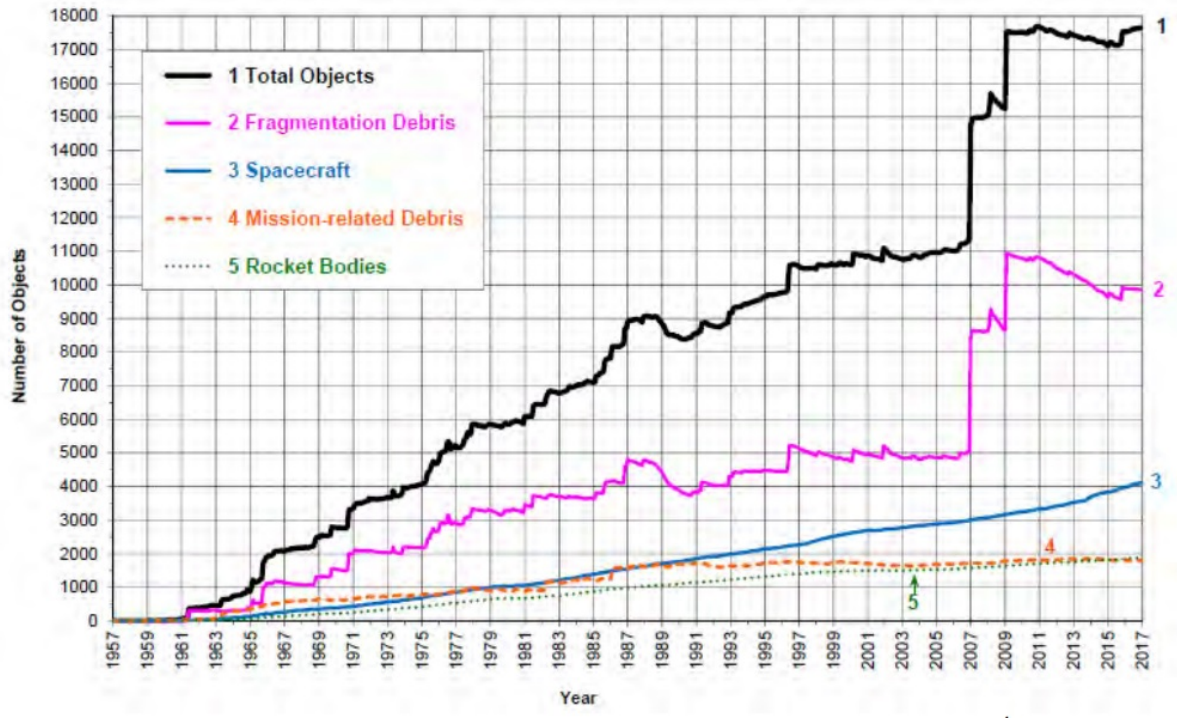

Figure 1.1 Catalogued space objects in LEO. Source: NASA [3]

1.1.3 Three debris congested regions in LEO

Space debris is mainly distributed in the LEO and geosynchronous orbits. Currently there are approximately 15000 objects with a diameter larger than 10 cm residing in the three most debris-congested orbits in LEO.[4]

The three regions in LEO with dense debris populations are:
1. Altitude: $800 \pm 100km, i = 99° \pm 1°$
- This region includes Sun-synchronous orbit, depicted as Region 1 (blue) in Figure 1.2.

2. Altitude: $850 \pm 100km, i = 71° \pm 1°$
- Depicted as Region 2 (white) in Figure 1.2.

3. Altitude: $1000 \pm 100km, i = 82° \pm 1°$
-Depicted as Region 3 (light blue) in Figure 1.2.

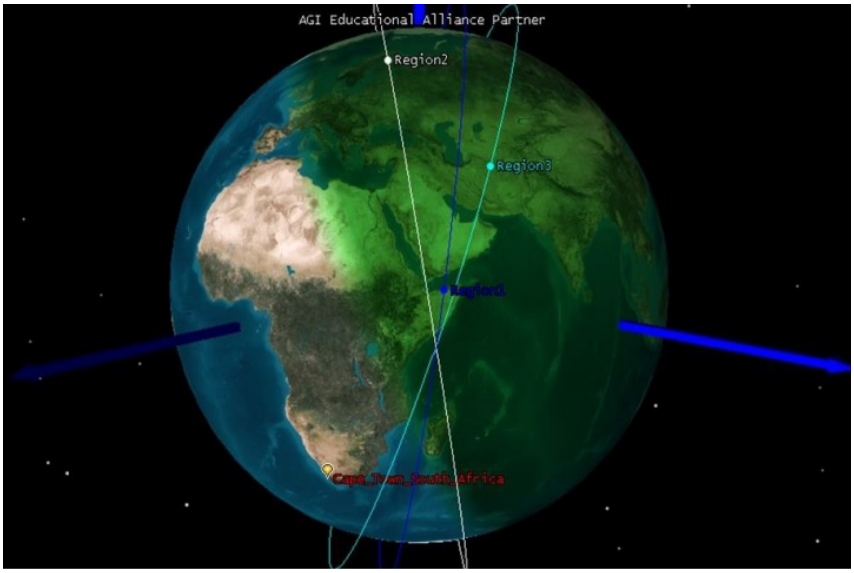

Figure 1.2 Three LEO orbital regions with high debris population depicted schematically in STK.

1.1.4 Proliferation of small satellite missions

Before the invention of CubeSats space missions were accessible only to national space agencies and large commercial space companies. Participation by universities in space activities was usually limited to providing payloads for missions developed by these larger actors. However, Cubesats have lowered the entry barrier to active participation in space activities and have thus become a game changer, enabling many universities and small companies to become space actors. CubeSats are typically built with commercial off-the-shelf components, reducing both development cost and time. Moreover, the cost to build and launch a CubeSat is much lower compared to the cost of building and launching traditional small satellites. CubeSats also have access to more launch opportunities, such as being launched as a secondary payload or from the ISS. Together, these characteristics make CubeSats an ideal platform for educational purposes at universities and even

high schools. Furthermore, CubeSats are now also considered as platforms for scientific research. For example, the QB50 mission that was launched in late 2016 is a CubeSat constellation in LEO proposed by the von Karman Institute in Belgium to study the thermosphere. These examples demonstrate how CubeSats are starting to transform the space ecosystem, especially in LEO. There are already numerous proposals to deploy CubeSats for lunar and planetary exploration missions in future.

However, we must examine clearly both positive and negative effects of this disruptive technology. Evidently because cost of the building and launching much lower, the population of CubeSats in LEO is increasing exponentially. CubeSats often have an on-orbit operational lifespan that is much, much shorter than their orbital life span. Many CubeSats are placed in orbit without a clear end-of-life disposal strategy.

Many CubeSats in LEO have completed their orbital missions and may now be classified as passive "space debris" adding to the trackable space debris category in Table 1.2, which could potentially be a source of new debris through collisions with other debris or active satellites. Table 1.3 below lists the number of CubeSats launched from 2013 to 2016.

Table 1.3 *CubeSats launched from 2013 to 2016. Source: [5]*

Year	**Quantity**	**Category**
2013	79	[a]Educational:33, [b]Military:21, [c]Civil:16, [d]Commercial:9
2014	102	Educational:18, Military:2, Civil:5, Commercial:77
2015	125	Educational:23, Military:10, Civil:15, Commercial:77
2016	77	Educational:19, Military:0, Civil:5, Commercial:53

[a] Educational: A University or other educational institution, including high schools, [b] Military: A government military / defence organization (e.g the US Air Force), [c] Civil: Civilian government organization (e.g NASA, JAXA, ESA), [d] Commercial: A private organization.

Figure 1.3a and 1.3b traces the growth of Cubesats from 2000 to end of July in 2016, broken down into various categories of users. From Figure 1.3a we can clearly see that CubeSats began to attract serious commercial interest from 2014 onwards. Since 2014, more than half of the CubeSats launched per year have come from commercial organizations. Universities have also been a consistent user of CubeSats. Roughly 10-20 CubeSats have been launched per year by universities worldwide in recent years to conduct scientific and technical experiments.

The overall performance of all CubeSats placed on orbit is depicted in Figure 1.3b. According to an analysis by Swartwout [5] 48,7 % of all CubeSats placed in orbit did not serve a useful purpose; they were either dead on arrival, failed early in orbit or did not reach their designated orbit due to launch failure. Only 51,7 % of all CubeSats launched since 2000 have completed their stated mission or are still in their operational phase. Thus, the current success rate of just slightly greater than 50 % indicates that CubeSats still have a lot of room for improvement and will take time to reach technological maturity.

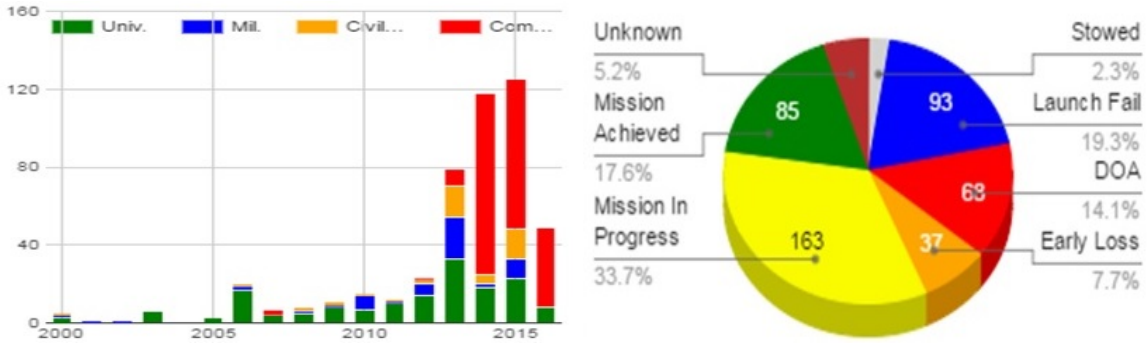

(a) CubeSats launched from 2000 to 2016 by Educational, Military, Civil and Commerical actors. Source: [5]

(b) Mission status for Cubesats launched from 2000 till end of July in 2016. Source: [5]

Figure 1.3 Analysis of Cubesats launched from 2000 to end of July in 2016. Source: [5]

1.1.5 Kessler syndrome

Debris population growth is no news to the space community, and the cascading effect of a constantly growing debris population is referred to as the "Kessler Syndrome", named after the NASA scientist Donald Kessler, who first described this cascading effect. Orbital debris travelling at a very high speed contains an energy release to mass ratio of 1250:1. When it collides with another object it is certain that both objects will break into pieces, and the resulting debris will continue to collide with other debris to generate more debris and impose higher collision risks on orbiting spacecraft. For instance, a debris fragment of 240 grams in mass will catastrophically destroy a 300 kilogram satellite due to its high orbital speed. Furthermore, this cascading effect increases the debris population density, directly increasing the probability of further collisions. Debris travelling in highly populated orbits have a higher chance to collide with other space objects, which creates more debris, further increasing collision risks in these densely populated zones. As time proceeds, if nothing is done to halt the debris population growth, eventually space missions in LEO will no longer be feasible.

The current spatial density of debris in different altitudes depicted in Figure 1.4. Aavailable studies [4] suggest that space debris poses a major threat to future space missions and that the debris population growth has to be mitigated by a series of regulatory and technical measures. Regulatory measures include the implementation of IADC or UN-COPOUS space debris mitigation guidelines. Technical measures can be either passive (e.g. shielding, cross-redundancy) or active (e.g. passivation, de-orbiting or collision avoidance). Although active collision avoidance reduces addition of debris to the orbit it does not reduce the number of debris that is already in place.

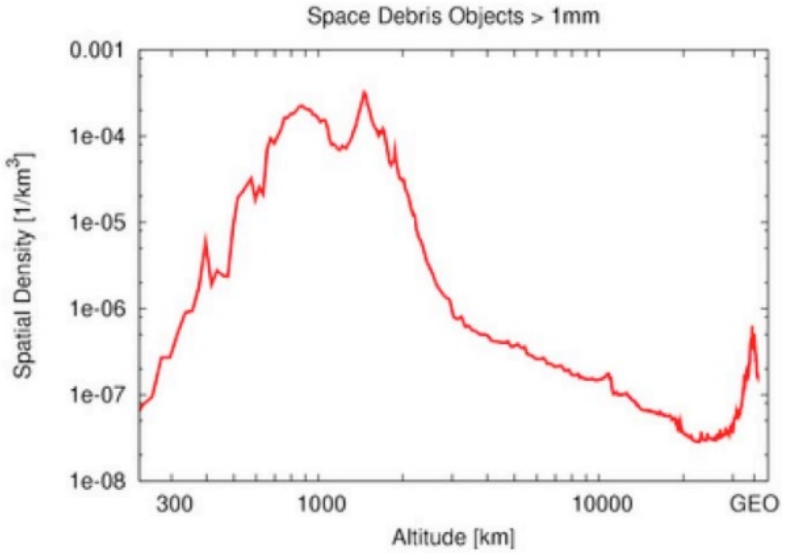

Figure 1.4 Spatial density of debris objects larger than 1 mm and their distribution in various altitudes. The high-density region in low Earth orbit, and the local peak at geosynchronous orbit are both evident. Source: [6]

1.1.6 The need for remediation

Several debris evolution models point to the catastrophy of debris population growth under no mitigation measures. For example, LEGEND, a LEO-to-GEO ENvironment Debris model developed at NASA, simulated the projected outcome of non-linear growth of space debris in LEO [7]. The model shows that in order to decrease the existing debris population, a combination of collision avoidance, post-mission disposal and active debris removal has to take place to stabilize the debris growth. Other independent models produce similar results.

Post-Mission Disposal (PMD) typically requires satellites in LEO to re-enter the atmosphere to burn up whereas satellites in GEO would move to a higher "grave yard" orbit that is about 300 kilometres above the GEO ring.

In 2007, a set of Space Debris Mitigation Guidelines was published by the Inter-Agency Space Debris Coordination Committee (IADC) [8], advising space-faring nations to not contribute towards the growing debris population. The guidelines cover the overall environmental impact due to space missions and focus on the following:

1. Limitation of debris release during normal operations.
2. Minimisation of the potential for on-orbit break-ups.
3. Post-mission disposal.
4. Prevention of on-orbit collisions.

In 2008, the United Nations Committee on the Peaceful Uses of Outer Space (UNCOPOUS) adapted the mitigation guidelines published by the IADC and introduced the

UN Space Debris Mitigation Guidelines [9] aimed to mitigate the effects of space debris through practical measures to be applied on a voluntary basis by UN member States. Seven such measures were recommended:

1. Limit debris release during operations.
2. Minimise the potential of break-ups during operations.
3. Limit the probability of accidental collisions in orbit.
4. Avoid intentional destruction and activities harmful to the environment.
5. Minimise potential of post-mission break-ups activated by stored energy.
6. Limit the long-term presence of spacecraft and launch vehicle stages in LEO region after the end of mission.
7. Limit the long-term presence of spacecraft and launch vehicle stages in GEO region after the end of mission.

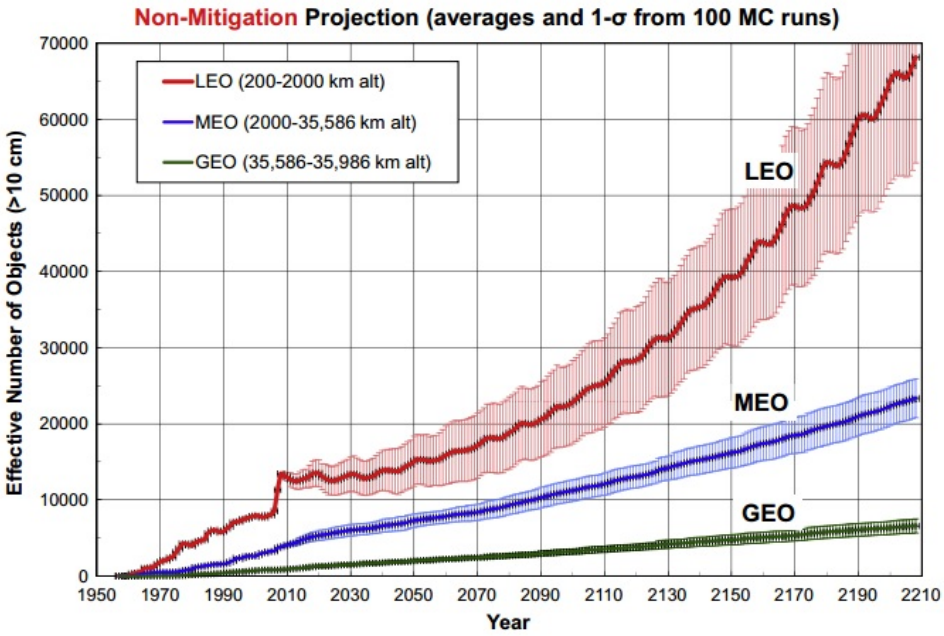

Figure 1.5 A simulation of projected debris growth in LEO, MEO and GEO under the scenario of no mitigation taking place in each orbital region. Low Earth orbit shows a far worse growth of debris than MEO and GEO. An average of 83 catastrophic collisions are expected to occur in LEO within the next 200 years. This number far exceeds the four incidents that have already occurred since the beginning of the space age in 1957. Source: [10]

Post-mission-disposal (PMD) will certainly help to reduce the rate of debris population growth, but on its own it will not arrest debris growth. This is the case even if we cease all launch activities immediately. In other words, the growth of the debris population will only be arrested or mitigated by removing objects from orbit.

The concept of Active Debris Removal (ADR) was proposed over 25 years ago. The underlying idea behind ADR is to identify a target in orbit, send a spacecraft with specific technology to actively remove the selected target from its current orbit and to de-orbit it to burn up on reentry[1]. In order to arrest growth of debris in LEO the models indicate that it would be sufficient to remove five large objects per year. Figure 1.6 [10] shows the effect of implementing such an ADR strategy in LEO starting from 2020 with three mitigation scenarios:

(a) Regular launches with 90% PMD.

(b) Regular launches with 90% PMD and active removal of two large space objects per year.

(c) Regular launches with 90% PMD and active removal of five large space objects per year.

As can be seen from the simulations, scenario (c) almost arrests debris growth for the coming decades.

In the past few years, ESA has studied several pushing or pulling technologies for controlled de-orbiting of defunct satellites. Three conditions were identified to make debris removal outcomes efficient in terms of the number of collisions prevented per object removed [1]. The three conditions for the selection of candidate targets for removal are:

1. Objects of high mass which inherently have the largest impact on the environment in a case of an orbital collision.

2. Objects with high collision probabilities, mainly those in densely populated regions.

3. Objects placed in high-altitude orbits, where their debris orbital lifespan is much longer than the 25 years recommended by the IADC.

Studies show that ADR target size selection depends on the objective of the ADR strategy.[12]

If the objective is to reduce *collision threat* for active satellites in the short-term, then ADR priority should be removing bullet-like objects. These are debris objects 1 to 10 cm in size with high probability of collision with large objects.

If the objective is to *stabilize the long-term growth* in the debris population, then priority should be given to removing large debris.

[1] Active debris removal can also be ground-based, An example is Project Orion proposed by NASA in the 1980s that used ground-based sensors and lasers for orbital debris removal. [11]

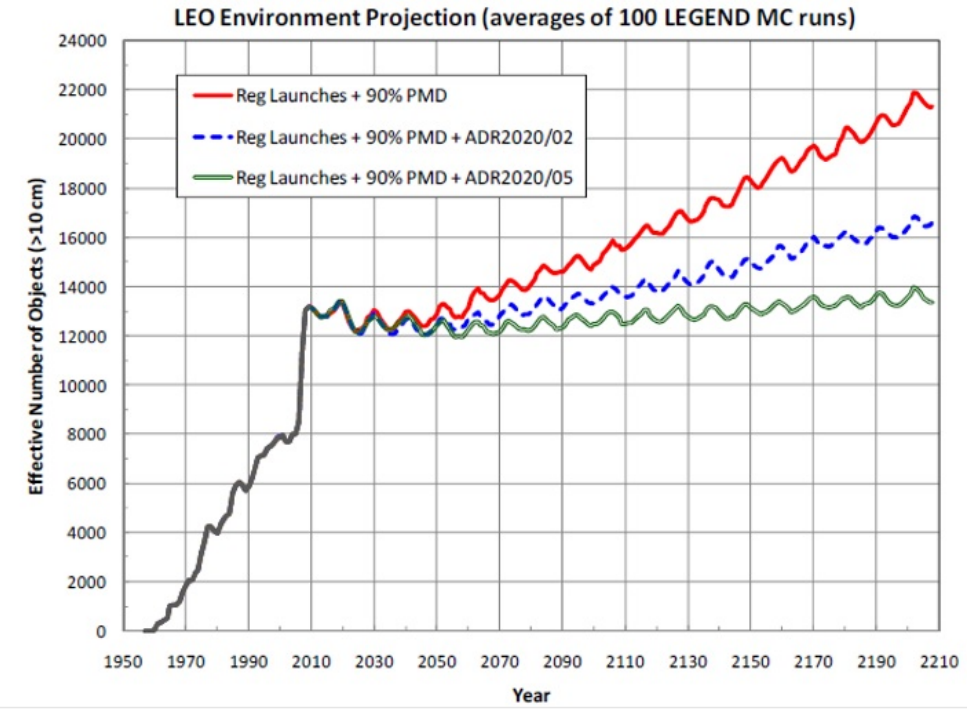

Figure 1.6 Projected increase of the future LEO populations for objects bigger than 10 cm. The simulation was done based on three different mitigation scenarios: (a) Regular launches with 90% PMD. (b) Regular launches with 90% PMD and active removal of two large space objects per year. (c) Regular launches with 90% PMD and active removal of five large space objects per year. Source: [7]

1.1.7 Main challenges in active debris removal

Active Debris Removal (ADR) faces financial, legal and technical challenges. From the financial perspective, up to five large objects have to be removed per year. The challenge lies in how to make it affordable and finding who is willing to pay for it.

From the legal perspective, international space law does not distinguish between operational satellites and non-operational space debris - all are regarded with an equal legal status as "space objects". Moreover, these space objects remain under the responsibility of the launching State, which has absolute liability for damage that these space objects may cause to the space objects of other nations. This poses a legal challenge for debris removal as only the launching State is entitled to remove its space debris. The high cost for no commercial return, as well as the technical and legal risks associated with debris removal missions, discourage launching States from acting responsibly to remove their debris. To date, there have been no successful active debris removal missions.

There is also considerable debate on the legality of removing debris objects where State of origin, or jurisdiction, is unknown. The debate centres on whether a mission target can be selected independently of the launching state, in other words, whether country A has the right to remove a space object launched by an unknown country B. This issue

is currently under discussion, and there have been several voices proposing that ADR operations should considered in a wider international perspective.

Technically, ADR has to overcome the challenges associated with changing the orbital parameters of a passive non-cooperating space object with no inherent propulsive capability of its own. Over the years, a wide range of methods have been proposed, ranging from using ground-based lasers to impart small velocity changes to debris of 1-10 cm size over a number of orbits, to various on-orbit technologies to capture and de-orbit larger space objects. To date, none of these concepts have been proven operationally in space.

Debris capture technology is grouped into two main categories: contact and contactless. The operational principle of contact methods is to connect a chaser spacecraft directly to a target during and after capturing and then to de-orbit both.

The challenges associated with target capturing require that the chaser spacecraft must be very flexible, adaptable to different targets and may require pre-knowledge of target shape, size, configuration, tumbling rate and spin axis. Hence, it is important to have a one size fits all solution that does not rely on specific characteristics or interfaces on the target.

A major challenge encountered during the capturing phase is where a large target has both a tumbling motion and the presence of numerous structures that protrude from the target. Appendages could potentially touch the capturing mechanism during the capturing process and push the target away. Hence without prior knowledge of the target, the chaser spacecraft becomes heavily dependent on image processing to recognize the target configuration and its appendages, such as protruding antennae or booms.

The target has to be flown around, approached, then connected to, requiring the design of a sophisticated system to achieve complex rotational and translational movements with short response time from the chaser spacecraft. This requires a higher capability of propulsion and Guidance Navigation and Control (GNC) than what is usually installed in spacecraft operating in LEO.[1]

To sum up, the close-proximity orbital operations and capture operations need to work flawlessly to avoid a collision between the target and the chaser spacecraft, which would lead to further debris proliferation, thus totally negating the objective of an ADR mission.

Contactless technologies tend to have lower requirements on the chaser spacecraft GNC capabilities since less complex propulsion systems are needed. However, many of the contactless technologies cannot manage a controlled trajectory during de-orbiting. Examples of such contactless ADR technologies include ion beam technology [13] that creates pressure on a target to change its trajectory and polyurethane foam technology [14] developed by the University of Bologna in which the chaser spacecraft shoots a stream polyurethane foam onto the target. Once the foam lands on the target it expands into a larger surface area that increases the atmospheric drag on the target leading to a faster de-orbit.

1.2 Evaluation of existing capturing concepts and proposal of a novel capturing concept

In this section we will examine the capturing technologies currently under investigation [1]. The challenge that any capturing technology was confront is targeted debris is usually classified as unprepared for capture and uncooperative. Very often, the target will not have a mechanical feature for the chaser to grasp, unlike a conventional rendezvous, say with the ISS, where a robotic arm is equipped to grab onto predetermined attachment points.

Numerous capturing mechanisms have been developed to date. Therefore it is worthwhile to conduct a thorough investigation and analysis of these capturing mechanisms to assess their Technology Readiness Level (TRL) for actual deployment.

The capturing mechanisms currently under investigation fall into four generic categories. They are the robotic arm, net, harpoon and flexible gripper.

Capturing mechanism concept 1. Robotic arm
A multi-sectioned 5 Degrees-Of-Freedom (DOF) robotic arm capturing mechanism known as the DEOS (Deutsch Orbital Servicing Mission) has been proposed by the German Aerospace Centre (DLR) [15] . The advantage of a robotic arm is the integration of many space applications in one device. In addition to capturing targets, it can also support other space mission applications such as on-orbit servicing and refuelling.

Capturing mechanism concept 2. Net
Net-capturing is the most promising capturing mechanism studied by ESA [1]. In this hard-capturing technique the chaser spacecraft casts a net onto the target to form a connection between target and chaser.

Capturing mechanism concept 3. Harpoon
The harpoon mechanism developed by Airbus Defence and Space performs a hard catch of target debris. The chaser spacecraft will fire a 2.5 kg harpoon projectile at 20 m/s onto a target and remain tethered to it after a successful capture [16]. Typical concerns with this technology are the penetrating ability of the harpoon and potential generation of additional fragments during the penetration.

Capturing mechanism concept 4. Flexible gripper
In this ADR concept the target is grasped by a number of flexible “fingers”. An example of this concept is the Dielectric Elastomer Minimum Energy Structure (DEMES) developed by the Swiss Space Centre.[17]

The actuator of the capturing mechanism consists of thin elastomer membrane coated on both sides with compliant electrodes. High voltage applied to the electrodes causes electrostatic pressure on the membrane. The elastomer film contracts in the thickness direction and expands in the plane direction. The elastomer moves back to its original position when the voltage is turned off. [17]

The four above-mentioned mechanisms are compared in Table 1.4. Mechanisms are compared based on major factors that lead to a successful capturing mission including: possibility of target capturing, target pre-knowledge requirements, possibility of debris proliferation and hardware manufacturing.

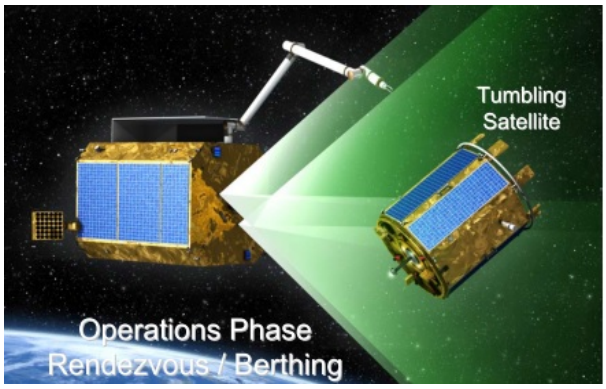

(a) Mechanism 1 - Robotic arm for debris capturing in the Deutsche Orbital Servicing Mission. Source: [18],[19]

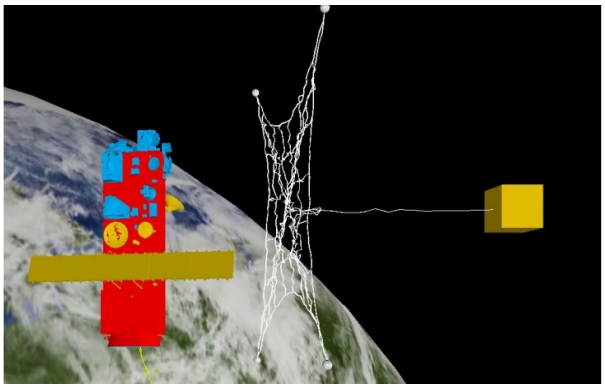

(b) Mechanism 2 - Net fired onto a target. Source:[1]

Figure 1.7 Capturing mechanisms 1 and 2 - Robotic Arm and Net.

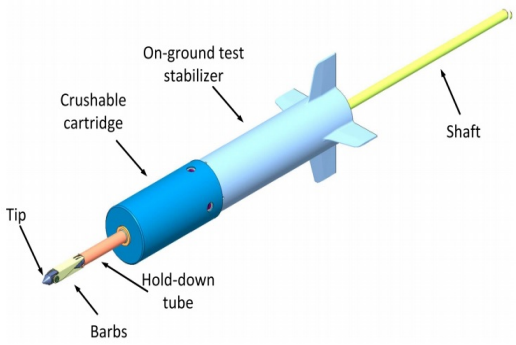

(a) Mechanism 3 - Harpoon capturing system for heavy space debris. Source:[20]

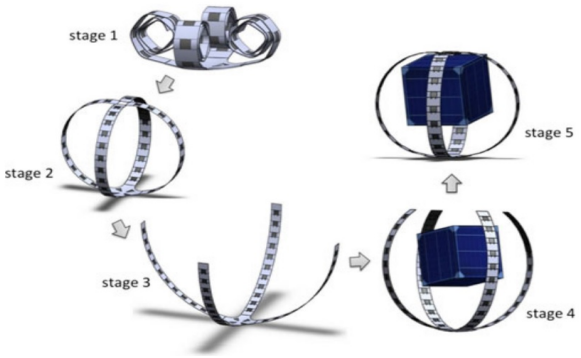

(b) Mechanism 4 - Dielectric Elastomer Minimum Energy Structure (DEMES). [17]

Figure 1.8 Capturing mechanisms 3 and 4 - Harpoon and Flexible Gripper.

Table 1.4 *Advantages and disadvantages of different capturing mechanisms.*

Capturing mechanisms	**Advantages**	**Disadvantages**
(a) Robotic Arm	This mechanism can be precisely manipulated by controlling the multiple joints. Other space missions that require docking can be supported with the same robotic arm.	To conduct space missions successfully a robotic arm requires high level of image processing and pre-knowledge of the shape and features of the target to identify a "grabable spot". Also complexity in design which could lead to high cost in development.
(b) Net	This capturing method could work without pre-knowledge of target. The net approach can work without knowing many features of a target such as target-size, shapes, attitude and tumbling rate.	The net approach allows only a single attempt to capture a single target, which limits capturing capacity per mission. Secondly, if the net does not reach its full designed opening area, this could directly result in mission failure, as seen in Kounotori-6 mission by JAXA in January 2017.
(c) Harpoon	This is a one shot capturing strategy. Forms a tethered connection with target once the harpoon penetrates the target and the barbs on harpoon then deploy to lock onto the edge of the penetrated target's surface.	High concerns in many aspects that could lead to mission failure and proliferation of debris. Aspects that could lead to mission failure include: penetrating ability; resistive strength of tether when pulling; potentially generation of additional fragments during penetration.
(D) Flexible gripper	DEMES is a soft gripper that allows multiple attempts on a single target or several targets, and presents only a small risk of generating additional debris. According to literature [17] the materials used to actuate DEMES are dielectric elastomer actuators and their response does not vary substantially over the temperature ranges and radiation levels found in LEO.	Requires complex and sophisticated rendezvous to align chaser spacecraft and the target within a finite distance of 1 m to begin the capturing process. High demands on propulsion capability and satellite attitude control could make design process complicated.

The above capturing concepts like the robotic arm require a detailed knowledge of the target object and an accessible attachment point, which may be difficult to grasp on a tumbling target. The net and harpoon capturing concepts are not as sensitive to tumbling and don't need an attachment point, but they are "one-shot" attempts, to capture the target, with no possibility to reuse the mechanism again.

In this thesis we have tried to come up with a debris capturing concept that does not require the existence of a pre-defined attachment point on the target object and that is also not sensitive to tumbling of the object (at least during the capture manoeuvre). We also wanted to explore a concept with the potential to be re-used.

The concept we come up with utilizes shape memory alloys to define a capturing volume around a target object. The concept is described in a bit more detail below.

Capturing mechanism concept 5. Cage
To "cage" a target is the novel capturing concept developed in this thesis. We aim to design a prototype to perform a soft-capture of a non-cooperating space object in a non-contacting manner, and then to de-orbit the captured target in a pushing manoeuvre. The prototype known as MEDUSA (Mechanism for Entrapment of Debris Using Shape memory Alloy) was designed to enclose and release a capturing volume multiple times to enhance the success rate of capture. MEDUSA is designed to embrace the target before touching it and once captured target debris is confined in a limited space.

Advantages of MEDUSA: An enlarged capturing volume is used to confine a target without touching appendages such as protruding antennas. Less contact with a tumbling target minimizes the disturbing effects of rotational motions during the capturing process and after.

Disadvantages of MEDUSA: A high capability in the attitude control sub-system might be needed to handle a collision avoidance manoeuvre with a target.

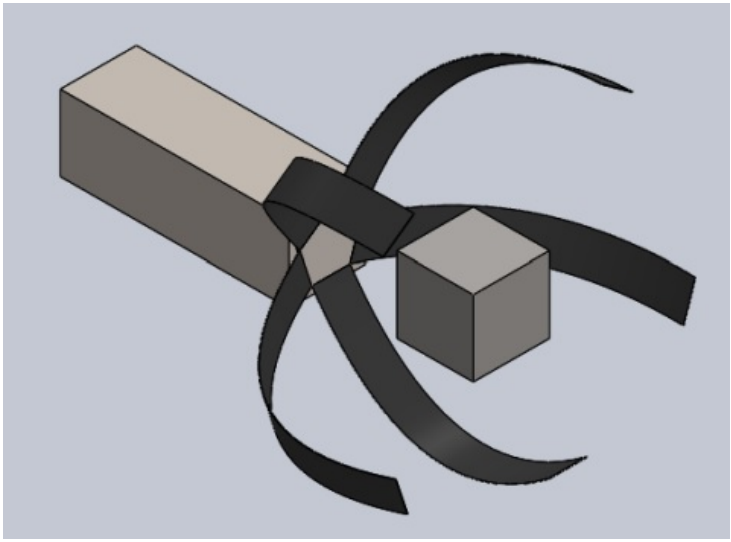

Figure 1.9 Mechanism 5 - Mechanism for Entrapment of Debris Using Shape memory Alloy (MEDUSA).

1.3 Project objectives and scope

The primary objective of this project is to design and demonstrate a proof-of-concept prototype in order to explore the potential to use shape memory alloys as a technological basis for a debris capturing solution that can be used multiple times. A secondary objective is to identify the technical issues that would need to be solved to use a CubeSat platform to evaluate the performance of such a concept prototype for a non-contact capture of non-cooperating space objects.

1.3.1 Targeted scale for prototype

MEDUSA has been designed to conform to the CubeSat form factor, so as to facilitate an eventual proof-of-concept demonstration in space.

1.3.2 Targeted technology readiness level

The conceptual prototype is to be developed up to a Technology Readiness Level (TRL) of 4, which validates the MEDUSA prototype in a terrestrial laboratory environment. The full scale of TRLs can be found in Table 1.5.

TRL	Description
1	Basic principle observed.
2	Technology concept and/or application formulated.
3	Analytical and experimental critical function and/or characteristic proof-of-concept.
4	Component and/or breadboard validation in laboratory environment.
5	Component and/or breadboard validation in relevant environment.
6	System/subsystem model or prototype demonstration in a relevant environment (Ground or Space).
7	System prototype demonstration in space environment.
8	Actual system completed and 'flight qualified' through test and demonstration (Ground or Flight).
9	Actual system 'flight proven' through successful mission operations.

Table 1.5 *Technology Readiness Level hierarchy used by NASA. Source:[21]*

1.4 Conclusion

In this chapter we have described the growing space debris crisis and outlined certain measures that have to be employed in order to achieve long-term sustainable use of outer space. We described studies showing that a combination of PMD and ADR are the most promising mechanisms to avoid the cascading effect of the Kessler Syndrome. We then discussed some of the common debris capturing concepts under development, such as robotic arms, harpoons and nets. The aim of this thesis is to develop a debris capturing mechanism for non-cooperating targets based on shape memory alloys that allows for multiple capturing attempts.

Among all the concepts for debris capturing mechanisms, not much work has been done to investigate the potential use of shape memory alloys for such applications. We have therefore decided to focus our research on these materials.

Chapter 2 provides an overview of requirements definition, as a preliminary stage to identify all the necessary characteristics in the design. Chapter 3 demonstrates four conceptual designs of MEDUSA: Spaghetti, Octopus, Cat's Tongue and Venus Flytrap. The advantages and disadvantages of each are described and then compared and rated in a scoring matrix. Chapter 4 describes the detail design of MEDUSA. Chapter 5 describes the manufacturing of MEDUSA. Chapter 6 displays test results conducted in vacuum and atmosphere laboratory environments, accompanied with analysis of each tests. Finally in Chapter 7 we present our conclusions and recommendations for future work.

Chapter 2

Requirement definitions for MEDUSA

In this Chapter, we define the high-level requirements for MEDUSA. These requirements provide guidance for the conceptual designs to be considered in Chapter 3 and also serve as a check list for next design phase.

2.1 Preliminary requirement definitions

Our high-level requirements specification is premised on the notion that we are seeking a debris removal concept that:

i) Does not rely on the existence of predetermined attachment points on the target object.

ii) Will define a capture volume around the target object.

iii) Can be used in multiple capturing attempts.

As this is a proof-of-concept design, our target for the purpose of demonstration is defined to be a 1U CubeSat with no appendages that project more than 10 cm from the satellite.

From the requirements stated above we proposed five high-level system requirements considering factors typically associated with target capturing missions. Factors considered were the possibility of target escape the limited time window for deployment, maximizing the number of capture attempts and lastly, a method to suppress the transfer of rotational kinetic energy from tumbling debris to the chaser spacecraft.

System Requirement 1. A spherical capturing volume equivalent to a 5-U CubeSat
A capturing volume of $5000cm^3$ was envisaged, which is approximately five times larger than the envisioned target size of a 1-U CubeSat to maximize the chance of successful capture.

Caging a target in a capturing volume is a soft-capturing method introduced in this research. Soft-capture by definition restrains a target within a confined space, without rigidly locking onto it. Enclosing the target within a larger capturing volume without physically touching it also eliminates the necessity of an on-board tumbling motion analysis system and decreases the possibility of the target being pushed away by the capturing mechanism during the capturing phase. Lastly, the maximum gap between the arms enclosing the capturing volume must be smaller than 7 centimetres to make the system more error tolerant and eliminate the possibility of target escape.

System Requirement 2. Response time less than 10 seconds
The allowable duration of a capturing attempt was defined to be 10 seconds to practise a successful target capture within a limited time window. This can be used as a requirement baseline for the respective AOCS system of the chaser spacecraft to maintain desired attitude while deploying the capture arms and capturing the target.

System Requirement 3. 10 attempts allowed for capture and release
Many of the capturing mechanisms existing at the moment such as harpoons and nets merely allow a single capture attempt. MEDUSA is designed to allow several capture attempts by adding a release function into the system. Following an unsuccessful capture attempt the user can open up the capturing volume again by activating the release function and proceed to the next capture attempt.

System Requirement 4. Easily adaptable mechanical interface for quick installation
MEDUSA is designed as a simple product without the need for complex interface hardware. MEDUSA is designed to be easily installable on a CubeSat through a plug-and-play approach similar to a USB drive.

System Requirement 5. Dampening of vibration and suppression of angular momentum transfer
Rotational kinetic energy transferred onto the chaser spacecraft from tumbling debris could possibly occur during direct contact with a target. Torque caused by rotational kinetic energy will be transferred to the chaser spacecraft and disturb its attitude state if no countering measures are taken. Hence MEDUSA needs to have damping ability to suppress undesired angular momentum transfer.

In Table 2.1 we break the system requirements down into three main requirement categories to examine each in further detail. The three main requirements categories are: functional, materials and compatibility. The requirements listed in Table 2.1 will guide the development of conceptual designs and the detailed design development to be presented in Chapters 3 and 4 respectively.

Table 2.1 *Functional and technical requirements. Requirements are ranked as follows: 1 - Essential; 2 - Highly desirable; 3 - Additional functionality desired.*

Requirement Category	Requirement Number	Rank	Requirement Specification
1. Functional	1.1) Open / close mode	1	Device must have an open (release) and closed (capture) state.
	1.2) Mode switch	2	Device must be able to switch between capture and release modes easily and smoothly, without additional control requirements.
	1.3) Repeatable results	1	Device must have repeatable capture and release motions up to 10 times.
	1.4) 5-U Capturing volume	1	Device must be able to envelope a 5-U spherical volume to entrap the target.
	1.5) Response time less than 10 seconds	1	Device must be able to fully enclose the capturing volume within 10 seconds.
	1.6) Operating temperature	1	Device must be able to operate between the temperature range of -40 ^0C to +90 ^0C outlined in [22] as thermal requirement for CubeSat components.
	1.7) Induced rotation	2	During deployment (opening or closing), device must not introduce undesired torquing onto chaser spacecraft.
	1.8) Dampening of rotation	1	Device must be able to suppress undesired rotation transferred onto chaser spacecraft bought by target debris.

Continued on next page

Table 2.1 – *Continued from previous page.*

Requirement Category	Requirement Number	Rank	Requirement Specification
2. Materials	2.1) Material selection	1	All materials used to construct the device must comply to the list of space approved materials published by NASA.
	2.2) Out-gassing	1	Out-gassing should not degrade material to an unusable stage.
3. Compatibility	3.1) Adaptable to any-U CubeSat	1	Device must conform to a 1U form factor and be easily installed onto any-U CubeSat used as test rig. (Plug and play).
	3.2) Compliance to CubeSat standard regulations	1	Electrical, power mass and volume dimensions must conform to CubeSat standard.
	3.3) Easily adaptable mechanical interface	1	Device must be able to install onto chaser spacecraft using simple mechanical interface without the need for complex interface hardware.

Chapter 3

Conceptual Design of MEDUSA

The basic idea of MEDUSA is encapsulated in System Requirement 1, namely that the target object is entrapped within a spherical capture volume. Several conceptual approaches to implement such a mode of capture were considered. These conceptual approaches are presented in this chapter.

Given that the capturing mechanism must envelope a spherical volume equivalent to 5U and at the same time it should stow within a 1U form factor, this excludes any solid "clamshell" type designs. Furthermore, there is no need to fill completely the surface of the capturing volume. The fully deployed capture volume surface may have any number of gaps in it as long as none of these gaps is large enough to allow a 1U CubeSat to pass through. Taking the above factors into consideration, a system of "ribs" attached to a common base seems to be the simplest approach to enclosing a capture volume with minimal structure.

In Section 3.1 we consider several variants of this basic concept and in Section 3.2 we discuss the advantages and disadvantages of each concept. In Section 3.3 we score the four conceptual designs against seven rating criteria, namely: collapsibility, power consumption, tumbling tolerance, perturbation possibility, target size tolerance, cost and complexity. These scores are then used to populate a concept scoring matrix and the highest scoring concept is selected for further detailed design development. In order to guide the detailed design development of the chosen concept, in Section 3.4 we define a series of attributes (e.g. mass, volume, power, etc.) with target values and acceptable values.

3.1 Four preliminary conceptual designs

In this section we present the four preliminary design concepts we considered.

3.1.1 Spaghetti

The first conceptual design, "Spaghetti", consists of 16 capturing arms with holes drilled through them for weight reduction and higher agility in the arms during the capturing process. Such a dense arrangement of arms reduces the size of inter-arm gaps, but it also raises concerns about the risks of so many arms getting tangled during deployment. Moreover, the large number of capturing arms in this design could be tangled during stowage which could cause difficulties when deploying the arms. Lastly, the narrow capturing arms may only offer limited ability to suppress tumbling motions of the target during capturing operations.

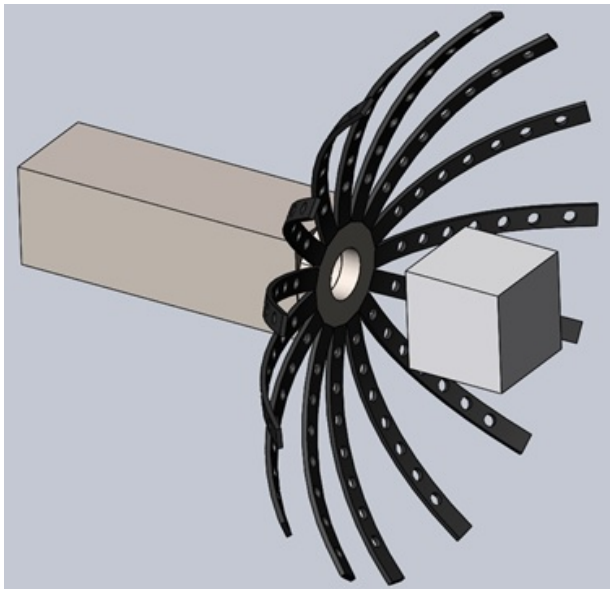

Figure 3.1 Conceptual design "Spaghetti", generated using Solidworks.

3.1.2 Octopus

The "Octopus" design has 8 capturing arms on which small magnets are attached. The width of each capturing arm is doubled compared to the "Spaghetti" design. The magnets are used to provide attractive forces for ferrous metal components on target debris. For example, Supra 50 [23], which is made of 48% nickel and 52% iron, is used to manufacture magnetic torquer rods [24], and UHF antenna structures are often made out of ferrous materials. However, this design raises concerns about the potential for interference of the magnets with other systems on the chaser spacecraft, particularly while the arms are in the stowed configuration.

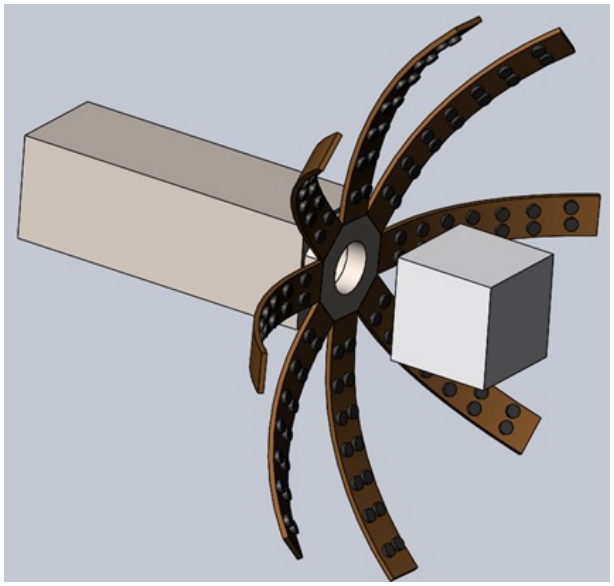

Figure 3.2 Conceptual design "Octopus", generated using Solidworks.

3.1.3 Cat's Tongue

The "Cat's Tongue" conceptual design has 4 broad capturing arms with small embedded hooks facing inwards. This design was inspired by the tiny backward-facing barbs (papillae) on the tongue of a cat. These barbs are used in grooming and also for rasping meat off the bones of prey. We use multiple and smaller hooks instead of bigger ones to minimize the possibility of hooks pre-contacting with debris before the capturing volume is fully enclosed. However, an obvious disadvantage associated with using hooks is that, if the hooks touch the edges of debris, it is possible to push the targets away instead of grabbing them into the capturing volume.

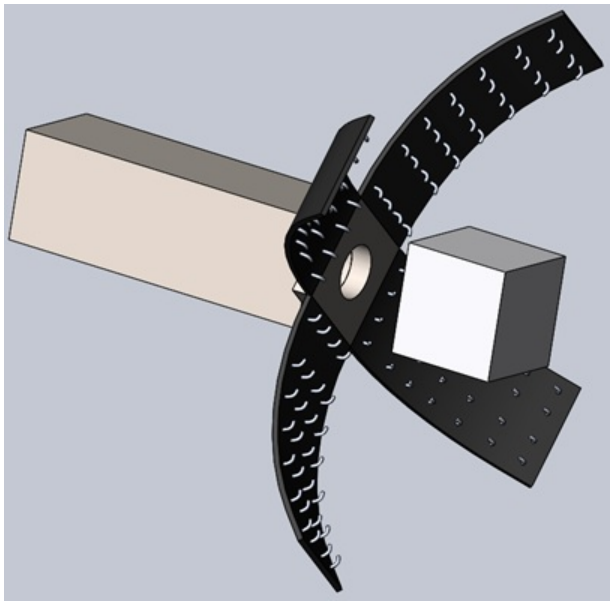

Figure 3.3 Conceptual design "Cat's Tongue", generated using Solidworks.

3.1.4 Starfish

The "Starfish" design consists of 5 capturing arms with narrow cut-outs for weight reduction and improved flexibility, covered by sheath made out of light reflective materials. It has no extra features to facilitate the capturing such as magnets and hooks. This concept merely uses the capturing arms to embrace the target without touching during capturing. To perform capture actions with such demanding precision, a high flexibility and agility is needed from capturing arms. This agility is achieved through a series of weight-saving cut-outs along the length of each arm.

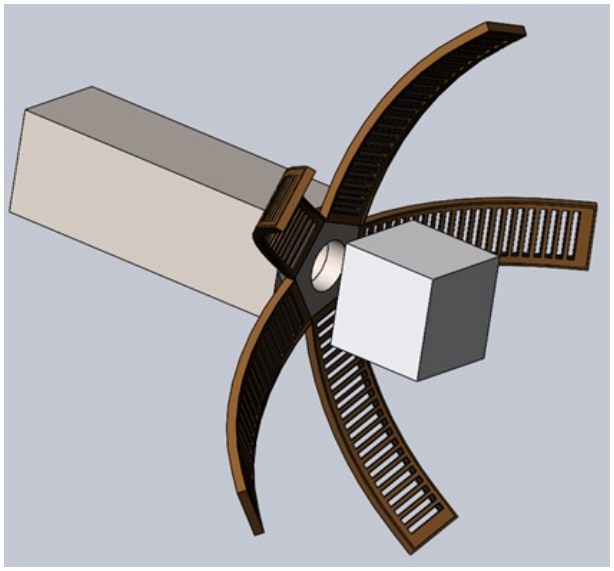

Figure 3.4 Conceptual design "Starfish", generated using Solidworks.

3.2 Comparison of the various preliminary design concepts

The advantages and disadvantages of each concept are discussed in the Table 3.1 below.

Table 3.1 *Advantages and disadvantages of different conceptual designs.*

Conceptual design	Advantage	Disadvantage
1.Spaghetti	This design has the most capturing arms to enclose the given capturing volume. Multiple arms ensure minimal gaps once capturing volume is enclosed.	Thin arms might not be able to provide sufficient stiffness when it comes to suppressing tumbling space debris. The actuation of multiple arms places a burden on chaser spacecraft's power system.

Continued on next page

Table 3.1 – *Continued from previous page.*

Conceptual design	Advantage	Disadvantage
2.Octopus	Magnets on capturing arms will attract ferrous metal components as the capturing volume is enclosing the target object.	The magnetic field generated by magnets might interfere with electronic systems onboard of a chaser spacecraft. Also standard non-ferrous materials commonly used to manufacture satellite structures and other components onboard will not be attracted to magnets (e.g. CubeSat structures made of aluminium).
3.Cat's Tongue	The small hooks facing inwards on the capturing arms provide a higher chance of "hooking" onto protuberances on the target object. Also, a larger capturing arm surface provides a higher force to suppress tumbling motions of target debris.	Finer proximity operation may be required, as well as a stronger actuation mechanism to drive bigger capturing arms. Furthermore, this design could possibly require higher electrical input to actuate larger capture arms. A higher power input requirement places a burden on the power systems onboard of a chaser spacecraft.
4.Starfish	This concept drives capturing arms designed with high flexibility to envelope the target before touching it during capturing, which minimizes the risk of pushing the target away before or during capturing.	As this concept has smooth arms with no barbs or magnets it may have higher risk of pushing the target out of the capture volume in the event of premature contact with the target.

3.3 Concept scoring matrix

In this section we discuss seven rating criteria to evaluate the concepts listed in Table 3.1. We used a qualitative technique known as the Pugh concept scoring matrix [25] to rank

the multi-dimensional options out of a conceptual design set. The criteria are expressed as equally weighted scores in the concept scoring matrix shown in Table 3.2. The criteria are briefly explained below.

Collapsibility - This is a measure of the ease with which the design concepts can be collapsed for compact stowage in a 1U form factor. Preliminary calculations show that all four designs require similar volumes for stowage. The 16 arms in the Spaghetti design have a higher possibility of arm entanglement when rolled up in the stowage state. Secondly the hooks on the Cat's Tongue design allow the possibility of hooks catching onto each other when the arms are rolled up, leading to an unsuccessful arm deployment from the stowage state.

Power Consumption - The electrical power needed to complete one capturing action. Spaghetti and the Cat's tongue might consume more power than the other designs because of having more capturing arms or larger capturing arms in the design.

Tumbling Tolerance - The ability of each concept to suppress tumbling motions based on mechanical characteristics, i.e stiffness. Besides the Spaghetti concept all other three concepts should have equivalent ability to suppress tumbling motions of the target.

Perturbation Possibility - The possibility of perturbing the target before it is fully enclosed in the capturing volume, thus pushing it away. Starfish has a higher possibility to confine the target without touching it because of numerous cut outs in the design which give it higher flexibility and agility.

Target Size Tolerance - The smallest target that fits into the capturing volume without escaping. Spaghetti and Octopus have the ability to confine smaller targets because both have more arms, which leads to smaller gaps in between arms.

Cost - The number of components used in the design directly affects the cost of production. The cost assessment is based on number of features each design contains. Octopus and Cat's tongue might score less in this category due to magnets and hooks attached onto arms.

Complexity - The difficulty to manufacture the arm designs in the four different concepts. Capturing arms in the Spaghetti and Starfish designs can be easily manufactured by laser-cutting whereas in the Octopus and Cat's tongue design one would have to calculate the size of magnets and hooks to be used as well as determine the positions of each appendages to fully utilize their advantages without causing difficulties during arm deployment or interfering with the electrical components on the chaser spacecraft.

Table 3.2 shows that "Starfish" is the highest rated concept and therefore most likely to satisfy the requirements. Hence the Starfish concept was selected for further design considerations shown in Section 3.4.

Table 3.2 *Concept scoring matrix, where concepts are rated on a scale of + or - compared to a baseline of 0 chosen arbitrarily in several categories, with + being above the baseline and most likely to satisfy the requirements and - being below the baseline and least likely to satisfy the requirements. In the concept rating columns α denotes the Spaghetti concept, β for Octopus, γ for Cat's Tongue and δ for Starfish.*

Rating Criteria	**Concept Rating**			
	α	β	γ	δ
Collapsibility	-	0	-	+
Power Consumption	-	0	-	+
Tumbling Tolerance	0	+	+	0
Perturbation Possibility	0	+	+	-
Target Size Tolerance	+	+	-	0
Cost	0	-	-	+
Complexity	+	0	0	+
Score	0	+2	-2	+3
Rank	3	2	4	1

3.4 Device functionality specification

In this section we present a list of device target specifications for mass, power and volume to help guide the detailed design of the Starfish concept. Table 3.3 lays down all attributes directly related to hardware design. The relative importance of each attribute is ranked on a scale of 1-5, with 5 being the most important. The acceptable values can later be used during the detailed design to decide between possible design trades.

Table 3.3 *Attributes for device functionality*

Attribute	**Importance**	**Units**	**Target Value**	**Acceptable Value**
Mass of device	4	*gram*	≤ 500	≤ 300
Volume for storage	4	*U*	<0.7	<1
Energy Consumption	4	*joules*	<1800	<2000

Chapter 4

Detailed design of MEDUSA

In this chapter, the detailed design and development of MEDUSA is discussed. Section 4.1 discusses the determination of the number of capturing arms required to enclose the debris capturing volume. Section 4.2 shows the determination of capturing arm lengths and shapes required. Section 4.3 shows the detailed design process for the capturing arms, including material selection and laser cutting pattern for the body of the capturing arms. Section 4.4 shows the design of an integrated base unit that serves as an interface between the chaser spacecraft and the capturing arms. Section 4.5 shows the electrical design, including the control circuit used to drive MEDUSA. Lastly in Section 4.6, we show the design of a functional flowchart for the operation of the MEDUSA system.

4.1 Determination of the number of capturing arms required

In Chapter 2, we specified that MEDUSA should have a 5U spherical capture volume. Table 4.1 lists the relevant parameters of this capture volume that must be taken into consideration in the detailed design.

Table 4.1 *Dimensions of the envisaged 5U spherical capturing volume.*

Parameters	**Spherical Capturing Volume**
Radius	10,61 cm
Diameter	21,22 cm
Circumference	66,66 cm
Surface Area	1414,6 cm^2
Volume	5000 cm^3

The MEDUSA concept envisages a 5-U spherical capturing volume that is defined by a number of arms. To work out the number of capturing arms required we first divide circumference of the spherical capturing volume into the segments containing arms and segments comprising the inter-arm gaps. To simplify the calculation we assume the arms

all have equal width and are evenly spaced around the circumference of the capture volume.

With these assumptions, we can readily relate the number of arms and gaps to the circumference of the capturing volume as follows:

$$N.W_{arm} + N.W_{gap} = C_{5U} = 66,66cm \tag{4.1}$$

where N is the number of arms, W_{arm} is the width of an arm, W_{gap} is the width of a gap and C_{5U} is the circumference of a 5-U equivalent sphere.

As the MEDUSA device is envisaged to be mounted on a Cubesat platform, the widths of the capturing arms are constrained by the Cubesat form factor of 10 cm by 10 cm. The second condition sets a numerical constraint on the width of the capturing arms (W_{arm}) and the width of gaps (W_{gap}). We set W_{gap} to be less than 7 centimetres at all times to prevent a 1-U target escaping between the arms. In addition, the maximum width of the arms must be such that they do not overlap each other as they are closing.

$$W_{gap} \leq 7cm \tag{4.2}$$

The size of the base of MEDUSA that can be used to mount the capturing arms is limited by the CubeSat form factor of 10 cm by 10 cm. The arms are mounted to a mounting plate that can be circular, square, pentagonal, hexagonal, etc, but which must fit within this form factor. Furthermore, the widths of all the arms, when placed side by side, cannot exceed the circumference of the mounting plate.

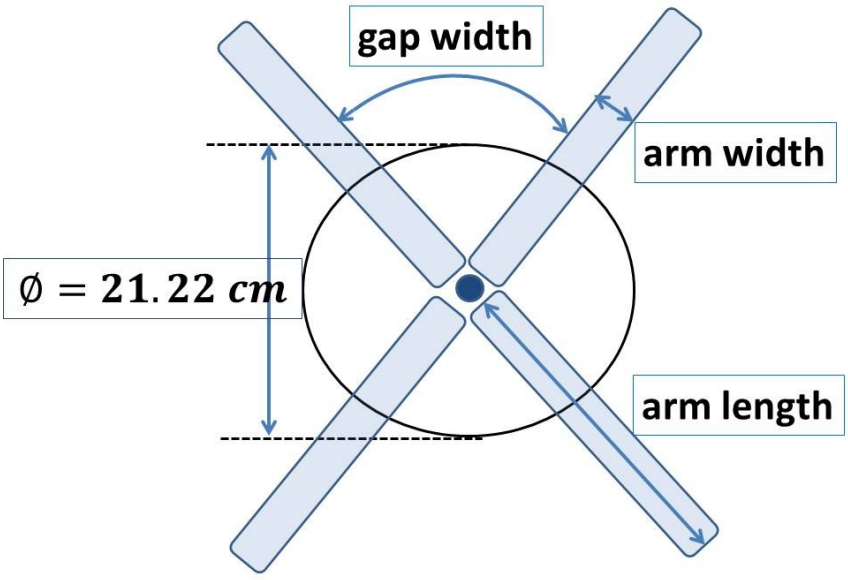

Figure 4.1 Illustration of arm width and gap width. The circle in the centre is the circumference of the capturing volume.

Table 4.2 lists a variety of possible configurations that satisfy the above conditions. Each configuration has its associated power requirements and design and manufacturing complexity.

Table 4.2 *Detail of design options available for various configurations of the number and width of arms needed enclose a 5-U equivalent spherical volume.*

Configuration	**Minimum width per arm**	**Maximum width per arm**	**Number of gaps**	**Minimum width per gap**	**Maximum width per gap**
4 arms	8.66 cm	10.66 cm	4	6 cm	7 cm
5 arms	5.53 cm	7.33 cm	5	6 cm	7 cm
6 arms	2.33 cm	5.11 cm	6	6 cm	7 cm
7 arms	1.52 cm	3.52 cm	7	6 cm	7 cm
8 arms	0.33 cm	2.33 cm	8	6 cm	7 cm

Examining the configurations listed in Table 4.2, we can see that the minimum arm widths for the 4-arm configuration exceeds the length of a 1U form factor. For the 6-arm configuration, although the total width required seems small enough to fit onto the MEDUSA base easily, the difficulties associated with manufacturing due to small arm widths makes this configuration less desirable. The same constraint applies to the 7-arm configuration and the 8-arm configuration. Hence the 5-arm configuration is the most feasible choice, as it represents a balance between ease of manufacturing and width limitations.

We then averaged the maximum and minimum width of the arms in the 5-arm configuration. This led to a number close to 6 cm and we round it off to 6 cm and proceed to next design phase with this value. The total width of 30 cm for the 5 capturing arms fits into the 1U form factor stated previously. Consequently, the maximum gap width lies between 6 cm and 7 cm. This gap width is acceptable, as it is smaller than the envisaged 1U target object.

4.2 Determination of capturing arm lengths and shapes required

To calculate the required length of each capturing arm, we divide the capturing volume circumference into two identical semicircular portions of 33.32 cm each. That means each arm has to be longer than 33.32 cm in order to fully enclose the capturing volume. To this length we add another 3 cm of clearance to connect the arm to the MEDUSA base. This gives a total length required for a single capturing of 36.32 cm; we round it off to 37 cm to simplify the precisions required during manufacturing.

In order to place the MEDUSA device on a CubeSat, the base of MEDUSA must fit within a 10 cm by 10cm square that defines the top face of a 1U CubeSat. This leads to an additional numerical constraint of 31.42 cm as the largest circle to accommodate the width of all the capturing arms.

The shape of the capturing arms is designed to have an appearance of a semi-circle that resembles the letter "C" when viewed from the side. The diameter of the semi-circle is calculated by halving the circumference of the capturing volume and then adding the 3 cm clearance length determined previously. Then we multiply 36.32 cm by 2 to get the entire circumference of 72.64 cm. Lastly, divide 72.64 cm by pi(π) to get an answer of 24 cm. Parameters used for calculations are shown in Figure 4.2.

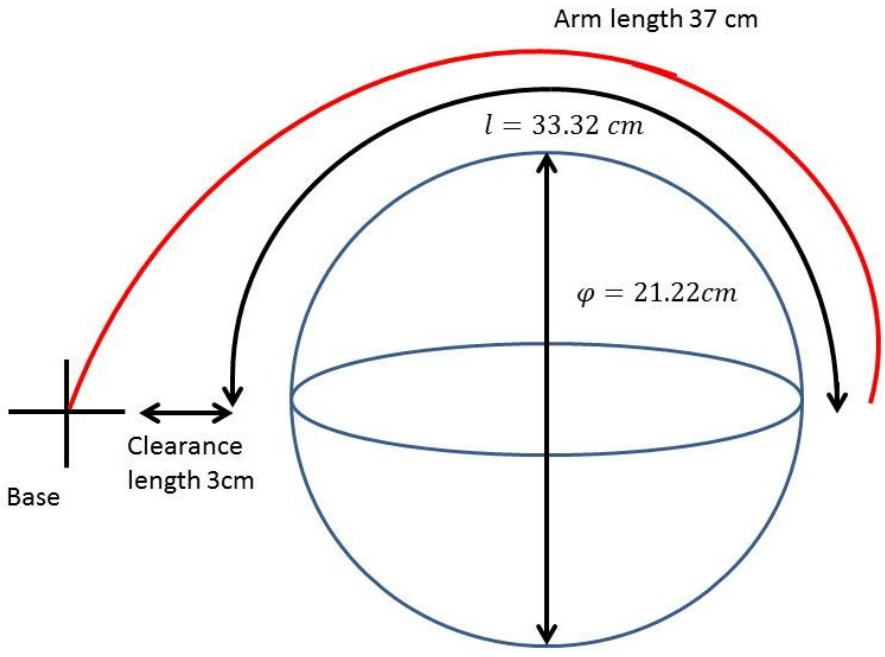

Figure 4.2 Illustration of arm length and shape required to envelope a 5-U equivalent sphere.

4.3 Detailed design of the capturing arm

This section is divided into six subsections that describe the detailed design process of the capturing arms on MEDUSA. Material selection for the skeleton, body and skin is discussed in Section 4.3.1. Technical details of the skeleton, body and skin of the capturing arm are discussed in Section 4.3.2, Section 4.3.3 and Section 4.3.5. The cut out pattern to reduce the arm's mass and increase its flexibility is discussed in Section 4.3.4. Then finally we show the complete conceptual design in Section 4.3.6.

4.3.1 Material selection

The materials selected to manufacture the capturing arm need to provide the necessary mechanical strength and stiffness to capture the target object, while having the necessary flexibility to enable agile operations. The materials must also survive in the harsh space environment. From the functional perspective the arms must be able to enclose a 5-U equivalent spherical capturing volume in less than 10 seconds and also damp tumbling motions and suppress vibrations. After closing, the arms must also be able to reopen and to carry out these closing/opening motions tasks with high repeatability.

To simplify the material selection process, a list of materials approved by NASA[26] was consulted to identify candidate materials that have been flown previously in space missions. The geometrical parameters of the capturing arms are listed in Table 4.3.

Table 4.3 *Geometrical parameters of MEDUSA capturing arms.*

Parameter	**Value**
Number of capturing arms required	5
Number of nitinol wires per capturing arm	4
Length	37 cm
Width	6 cm
Shapes required to conduct capture/release	"C-Shape" and "L-Shape"

4.3.2 Nitinol - The skeleton of the capturing arm

The primary mechanism to enclose a spherical capturing volume is based on using a shape memory alloy (SMA). SMAs are well known for their ability to recover a pre-programmed shape after distortion. Nitinol (NiTi) is a SMA that consists of 45% nickel and 55% titanium. It is commonly used in spacecraft, mainly as the structure of an ultra-high frequency (UHF) antenna. It is a material approved by NASA for space applications as listed in [26].

To allow multiple capturing attempts during a space mission, the capturing arm must be able to reverse the capturing operation and open up the capturing volume for the next capture attempt. The project requirement states that the capturing action must be repeatable for at least 10 times.

Nitinol can be mechanically distorted and restored to a programmed shape numerous times by heating the material to induce a state transition from a Martensite state to an Austenite state. During the state transition a large recovery force can be generated from a small dimension and weight of this material. Therefore we selected nitinol from the family of SMA materials and use it as the skeleton of the capturing arm. The standard properties of nitnol are listed in Table 4.4.

In the MEDUSA application, the repeatability of capture and release actions is achieved through the installation of two nitinol wire frames differently programmed onto a single capturing arm. As discussed in Section 4.2 the "C" shape programmed nitinol wire frame encloses the target, and the "L" shape programmed nitinol wire frame releases the target. To conclude the design, each capturing arm will contain 2 "C" shaped nitinol wires and 2 "L" shaped nitinol wires, to have sufficient forces generated to execute the capture and release actions.

The state transition of nitinol is purely temperature driven. Depending on its temperature, nitinol can be in one of two phases, known as Austenite or Martensite. Austenite is the stronger, higher temperature phase and Martensite is the weaker, cooler temperature phase. When the nitinol wire is in its Martensite phase it is easily deformed and will remain deformed until it is heated to its transformation temperature to the Austenite phase, where it recovers its previous shape with great force. Figure 4.3 shows the hysteresis loop of nitinol. Hysteresis is the temperature difference between a material's phase transformations upon heating or cooling. Below the activation temperature the state of nitinol will remain at the state of finished Martensite M_f. When it is excited by a heat source, the state transformation begins from M_f to the start of the Austenite state A_s. The material then continues to transform until it reaches the finished state Austenite A_f. At the state of A_f no further shape restoration will occur beyond the shape it is currently holding. When the heat source is removed and the nitinol starts to cool down it will transform from A_f to the start of Martensite state M_s and then move towards the end of the Martensite transition M_f as it cools down more. Once the nitinol state is at M_f it is back to the starting point on the hysteresis loop shown in Figure 4.3.

During a debris capture operation the capture arms of MEDUSA would be activated and driven by current that causes the nitinol temperature to rise. We noticed a difference in the resistivity value in the two states of nitinol. The resistivity value of the higher temperature state (Austenite state A_f) was approximately 8% higher than the lower temperature state (Martensite state M_f). This characteristic could potentially change the heating profile when heated using constant current. Input power converted into heat gain of nitinol was calculated by the equation $P = I^2R$. Over a specific time period the total input electrical energy is $E = I^2 \cdot R \cdot t$. Hence a slight change in resistivity would lead to an increase in the required electrical energy.

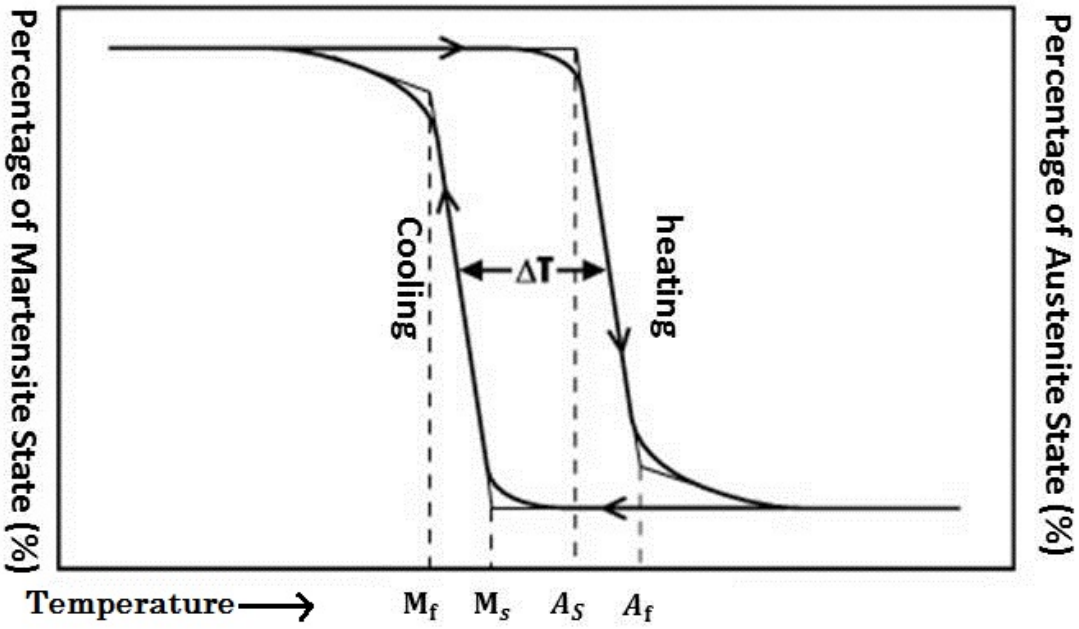

Figure 4.3 Hysteresis loop of nitinol[27]. A_s is the temperature where the material begins to transform to Austenite upon heating. A_f is the temperature where the transformation to Austenite has finished upon heating. M_s is the temperature where the material begins to transform to the Martensite phase on cooling. M_f is the temperature where the transformation to Martensite has finished on cooling.

Table 4.4 *Standard mechanical and thermal properties of nitinol. Source: [28],[29]*

Characteristics	**Value**
Density	6.45 $\frac{g}{cm^3}$
Thermal Conductivity	10 $\frac{W}{m \cdot K}$
Specific Heat	322 $\frac{J}{kg \cdot K}$
Latent Heat	24200 $\frac{J}{kg}$
Ultimate Tensile Strength	750 - 960 MPa
Elongation to Failure	15,5 %
Resistivity in Austenite state	82 $\frac{\mu\Omega}{cm}$
Resistivity in Martensite state	76 $\frac{\mu\Omega}{cm}$
Yield Strength in Austenite State	500 MPa
Young's Modulus in Austenite State	75 GPa
Yield Strength in Martensite State	100 MPa
Young's Modulus in Martensite State	28 GPa

4.3.3 Polyamide - The body of the capturing arm

Polyamide was selected as the material for the body of the capturing arm as it is also included in the list of materials approved by NASA [26]. Polyamide is a polymer product widely used in the aerospace industry for having robust thermal properties and resistance to the ageing effects experienced by many other polymers.

The thermal properties of polyamide lie within the temperature range experienced in LEO space missions. Its long-term service temperature can range from -40 °C to 110 °C and its melting point is 260 °C.

Moreover, polyamide inherently damps vibrations, which is an advantage in this application when physical contact with a tumbling object occurs during capturing. Lastly, the electrical insulation property of polyamide prevents short-circuits through the material.

Polyamide's material characteristics and their values considered during the design process are listed below in Table 4.5. The detailed material characteristics can be found in Appendix A.2.

Table 4.5 *Standard mechanical and thermal properties of Polyamide.*

Characteristics	**Value**
Density	1.15 $\frac{g}{cm^3}$
Tensile Strength	75 MPa
Elongation at Break	45 %
Thermal Conductivity	0.25 $\frac{W}{m.K}$
Long Term Service Temperature	-40 °C to 110 °C
Short Term Service Temperature	170 °C
Heat Deflection Temperature	95 °C
Melting Temperature	260 °C

4.3.4 Laser cut pattern design

In order to reduce the stiffness of the polyamide arms to the bending forces generated by the nitinol wires, and also to reduce the mass of the arms, we introduced a series of cut-out slots along the length of the arm. A unique cut-out pattern was calculated to create channels for holding the nitinol wires while allowing their free movement in actuation.

In order to secure the polyamide strips to the nitinol wire frames, we cut out a series of "arrows" that could be rolled up to form loops by pressing the polyamide arrowheads through the strip. The nitinol wire frames were then threaded through these loops along the one side of the length of the arm, through a pair of eyelets in the free end of the arm, and then through the loops running along the length of the opposite side of the arm. The loops have sufficient clearance to allow the nitinol wires to move freely through them as the arm is actuated.

The slots and arrows were laser cut to ensure consistent behaviour of the arms. Figure 4.4 shows the laser cutting pattern which was developed through trial and error and testing of several prototypes. The final design was laid out to use the material as efficiently as possible.

After laser cutting 43% of the original polyamide mass was extracted, leaving 57% residual mass in a 6 cm x 37 cm rectangular strip. The resulting polyamide strips are much more flexible and agile after the excess material was removed and consequently less force is required for actuation.

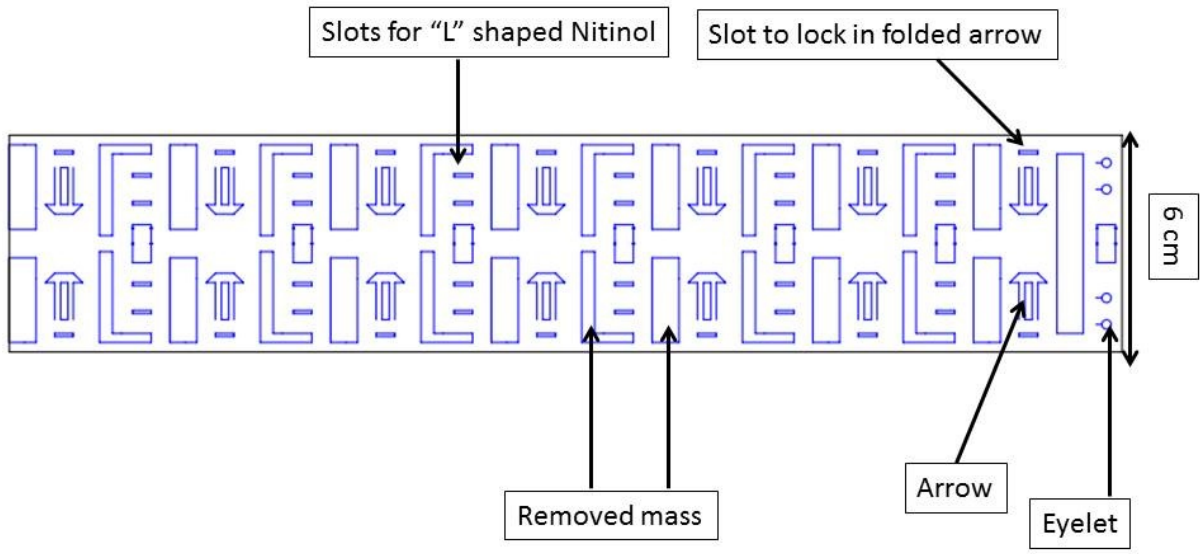

Figure 4.4 Laser cutting pattern for the polyamide arm.

4.3.5 Kapton HN (Polyimide) - The skin of the capturing arm

In the space environment, the nitinol wire frames and the polyamide body of the capturing arms will be subjected to extreme thermal variations that could result in a distortion of the arm shapes. Hence we introduced a sheath made out of light-weight reflective material to protect the nitinol and polyamide from solar radiation.

Kapton HN is widely used for thermal protection on spacecraft especially in structures exposed to direct solar radiation. An example would be the sun shield on James Webb Space Telescope.

Light reflective covers produced from Kapton HN film are wrapped around each capturing arm. This protective sheath reduces solar radiation heating of the capturing arms. The data sheet of Kapton HN is attached in Appendix A.3.

4.3.6 Finalized capturing arm design

The completed capturing arm comprises two “C” shaped nitinol loops and two “L” shaped nitinol loops, threaded through the laser-cut polyamide strips. The “C” shaped loop is the capture loop and the “L” shaped loop is the release loop. The arm is encased in a protective sheath made out of Kapton HN.

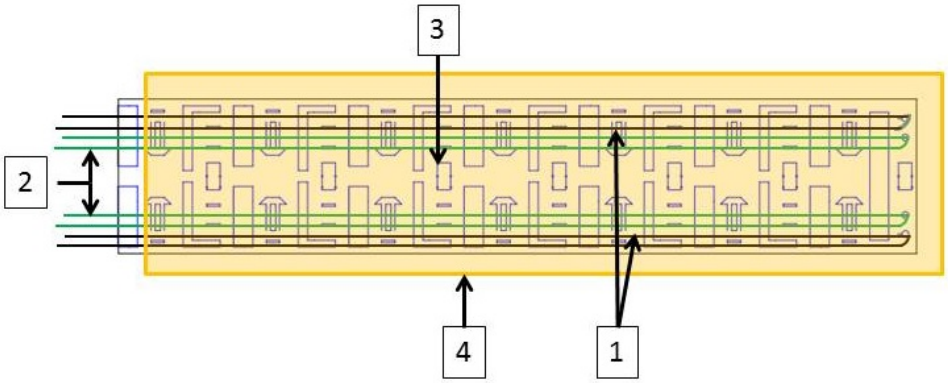

Figure 4.5 Schematic diagram of the design of a Capturing Arm design. 1- “C” shaped nitinol, 2- “L” shaped nitinol, 3- “body” made out of polyamide and 4- “sheath” made out of polyimide.

4.4 Design of an integrated base unit for the capture arms

In this section we discuss the design of an integrated base unit to anchor the arms of MEDUSA. This important component anchors the arms mechanically and allows electrical cables to pass through for power needed for the capture and release operations. The base must also provide a means to decouple the rotation of the target, once it is captured, from the chaser spacecraft. Lastly, the base unit must also be manufactured out of materials appropriate to its function and operation in space. In the following subsections we address each of these considerations.

4.4.1 Square-base design

The square-base is the foundation for the integrated base unit; it is the mechanical interface between MEDUSA and the chaser spacecraft. It is designed to mechanically fit onto the 1U top face of the chaser spacecraft. The design is finished with a cylinder placed on the square-base with co-aligned centers to accommodate a ball-bearing.

Figure 4.9b shows the geometrical design of the square base. The engineering drawing of this component is attached in Appendix B.1 and B.2.

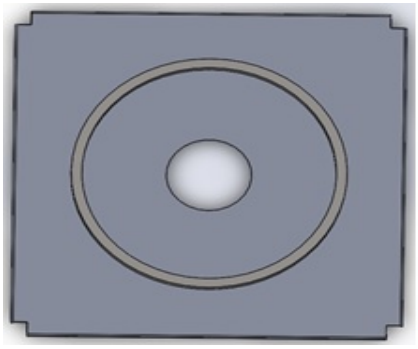

(a) Square-base in top view. Length 90 mm per side with a 1mm by 1mm square removed from the four corners. The central circular hole has a 20mm diameter. The cylindrical collar placed in the middle has inner diameter (ID) 56mm, outer diameter (OD) 61mm and is 15mm in height.

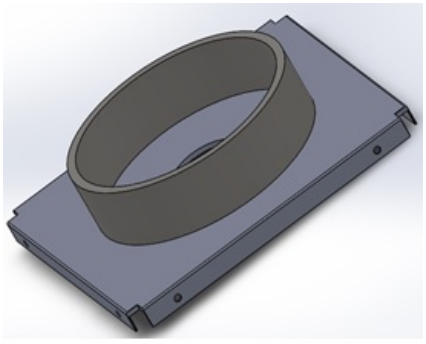

(b) Square-base in 45^0 inclined view. Two 2 millimetre holes (ϕ_{2mm}) are drilled per side. These serve as mounting points to fix the square base to the host satellite.

Figure 4.6 Geometric design of the square-base.

4.4.2 Arm mounting plate design

The arm mounting plate is a pentagonal shape with each side providing mechanical and electrical attachment points for one of MEDUSA's arms. Four holes are drilled per side to accommodate the C- and L-shaped nitinol wires. The C-shaped nitinol wires pass through the two outer holes and the L-shaped nitinol wires pass through the two inner holes. Each hole is 2 millimetres in diameter, which is 1 millimetre wider than the diameter of the nitinol wires used. This is to provide sufficient clearance for the nitinol to move freely while executing the capturing or releasing motions.

The cross-section of the arm-mounting plate is smaller than the square-base, so it can be stowed properly without touching the inner surface of a CubeSat POD launcher. The engineering drawing of this component is attached in Appendix B.3.

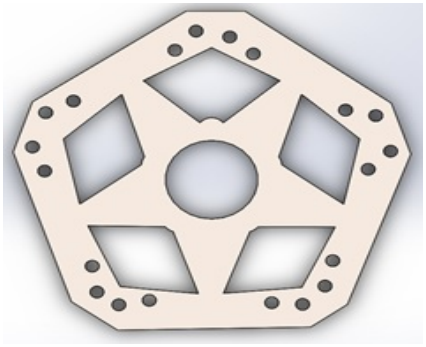

(a) Arm mounting plate in top view.

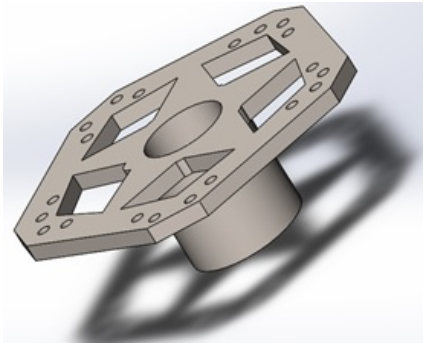

(b) Arm mounting plate in 45^0 inclined view.

Figure 4.7 Geometric design of the arm mounting plate.

4.4.3 Rotational decoupler design

In order to decouple the rotation of the captured target object from the chaser spacecraft, a sealed ball-bearing is placed between the arm mounting plate and the square-base. In an ideal scenario, the ball-bearing isolates the capturing arms from the square-base and absorbs rotational kinetic energy in one axis. Decoupling the chaser spacecraft from the capturing mechanism minimizes disturbances acting on the attitude of the chaser spacecraft.

(a) Unsealed ball-bearing in top view, OD 55mm, ID 31 and 12mm in height.

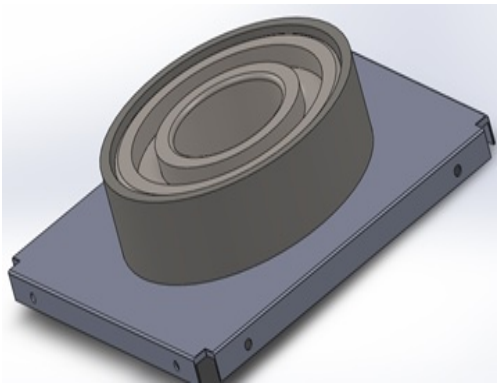

(b) Ball-bearing placed in cylinder on the square-base. The ball-bearing is the only connection between the arm-mounting plate and the square-base.

Figure 4.8 Geometric design of the rotational decoupler.

4.4.4 Integrated base unit assembly

All three components presented above form the integrated base unit. The integrated base unit comprises the square base at the bottom, the ball-bearing placed in the cylindrical collar, and the arm mounting plate connected to the inner ring of the ball-bearing.

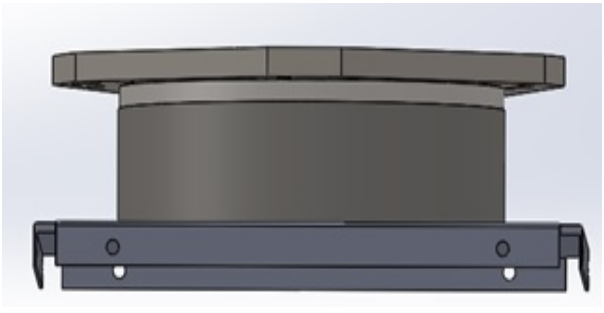

(a) Integrated base unit in front view.

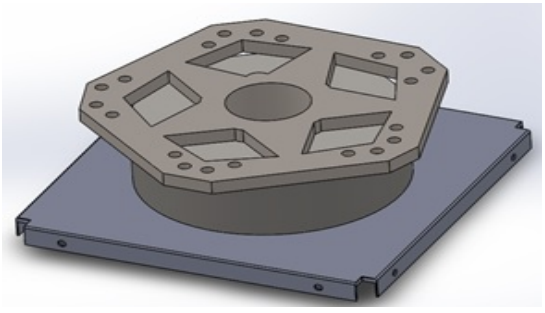

(b) Integrated base unit in 45^0 inclined view.

Figure 4.9 Geometric design of the integrated base unit.

4.4.5 Material selection for the integrated base unit

A wide range of materials was considered to identify the ideal candidate material for each part. Our material choices were guided by the following considerations:

- Thermal properties – The selected material must allow the relevant component to operate smoothly in a temperature range from -10^{0}C to 110 ^{0}C.
- Out-gassing – The selected material must not out-gas in a vacuum environment. For prototyping purposes, we tested materials that are easily purchased, low cost and require short processing time.
- Ease of manufacturing - The selected material must be readily available and must be easily worked with standard workshop machines and laboratory equipment.

Not all materials identified are easily attainable on the open market, hence for concept validation purposes we proposed several substitute materials to construct MEDUSA prototypes, as shown in Table 4.6.

As it contains moving parts, the rotational decoupler requires particular attention with regard to material properties. The ball-bearing must be immune to out-gassing and cold welding. Cold welding occurs when the lubricant evaporates in vacuum and causes two metal surfaces to come into direct contact and adhere to each other. Cold-welding effects do not occur in ceramic ball-bearings and thus it is an ideal candidate. However, for concept validation purposes, a readily available metal ball-bearing was used to test the concept of decoupling the chaser spacecraft rotationally from a tumbling target.

Table 4.6 *Material selection for integrated base unit construction.*

Component Name	**Preferred Materials**	**Prototype Material Used**	**Reason**
Square Base	Aluminium Stainless Steel Titanium	3-D printed PLA Chemically processed bamboo Polyamide	Low Cost Low technical requirement on manufacturing Short manufacturing time
Arm mounting plate	Space graded high temperature plastic Ceramic Glass fibre	3-D printed PLA	Low Cost Low technical requirement on manufacturing Short processing time
Rotational decoupler	Ceramic	Standard metal ball-bearing	Low cost Readily available

4.5 Electrical circuit design

The circuit design considers a few contingencies that could lead to a failure of the target capturing mission. One contingency is when the five capturing arms do not deploy simultaneously. A resultant torque will be caused by unbalanced forces during deployment and act on the chaser spacecraft and disturb its attitude state. Thus, we must design a control system based on hardware capabilities that acts on all capturing arms concurrently. This is achieved by using parallel circuits that supply power to all capturing arms simultaneously.

The control system of MEDUSA consists of two series branches connected in parallel that operate the capture and release functions. Each of the five capturing arms has 4 loops of nitinol wires, two for the capture circuit and two the release circuit. The total length of each wire loop is 0.78 m, which is threaded through the polyamide arm as shown in Fig 4.4. The capture circuit contains 10 nitinol loops and the release circuit also contains 10 nitinol loops, leading to a total of 20 nitinol loops used in MEDUSA.

The results presented in Table 4.7 show the power consumption and efficiency of each circuit. Input voltage and current values were taken from lab test results shown in Chapter 6.

The resistivity(ρ) value used in the calculations was 0.8 $\frac{\mu.\Omega}{m}$. According to the nitinol data sheet in Appendix A.1, the resistivity value lies between 0.5 $\frac{\mu.\Omega}{m}$ and 1.1 $\frac{\mu.\Omega}{m}$. Hence we take a representative average value of 0.8 $\frac{\mu.\Omega}{m}$ and then verify it against measured results shown in Chapter 6.

Table 4.7 *Electrical parameters of MEDUSA circuits.*

Parameter	**Single Nitinol Loop**	**Capture Circuit**	**Release Circuit**	**Determined by**
Nitinol length	0,78 m	7,8 m	7,8 m	*Measurement*
Input Voltage	8 V	18 V	18 V	*Measurement*
Input Current	5,11 A	10,22 A	10,22 A	*Measurement*
Resistance	0,74 Ω	1,85 Ω	1,85 Ω	R=$\frac{\rho \cdot l}{A}$
Power Consumption	18,27 W	193 W	193 W	$P = I^2 \cdot R$
Efficiency	44,71 %	95.2 %	95.2 %	e=$\frac{I^2 \cdot R}{V_{IN} \cdot I}$

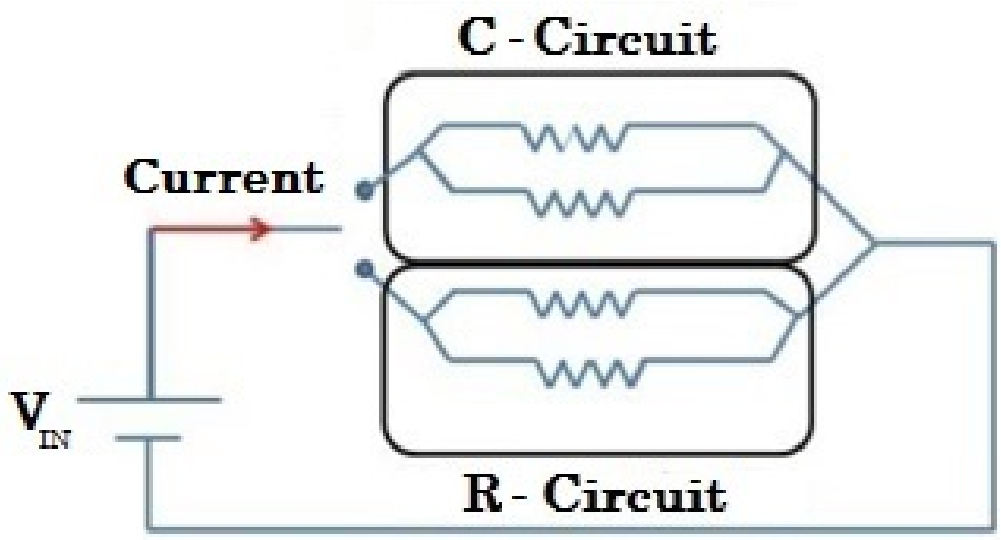

Figure 4.10 Control circuit of MEDUSA. Each resistor represents five nitinol loops wired in series, with a combined resistance of 3.48 Ω. The total resistance for the capture circuit and release circuit is 1.85 Ω each.

4.6 Design of a functional flowchart

Figure 4.11 below depicts the functional flowchart of MEDUSA. The functional flow sequence goes from the stowed state to deployment in the release configuration, from release to capture, and from capture back to release when instructed.

In its stowed configuration, the capturing arms will be folded into a volume of less than 1-U and remain packed until deployment. When the deployment command is received, current will flow through the release circuit (R-circuit) containing the L-shaped nitinol wires and the arms will unfurl to the open (release) state of the capturing volume. To capture the target, current must be passed through the Capture circuit (C-circuit) containing C-shaped nitinol wires, which activates the nitinol's pre-programmed memory to enclose a 5-U capturing volume.

After this soft-capturing motion is performed, the target will be trapped inside the capture volume. In the event of a miss-capture or an unsuccessful partial capture, the capturing volume can be opened up again, simply by passing current through the R-circuit. The capturing volume will open up to allow the next capturing attempt. This process can be repeated until the target is successfully captured.

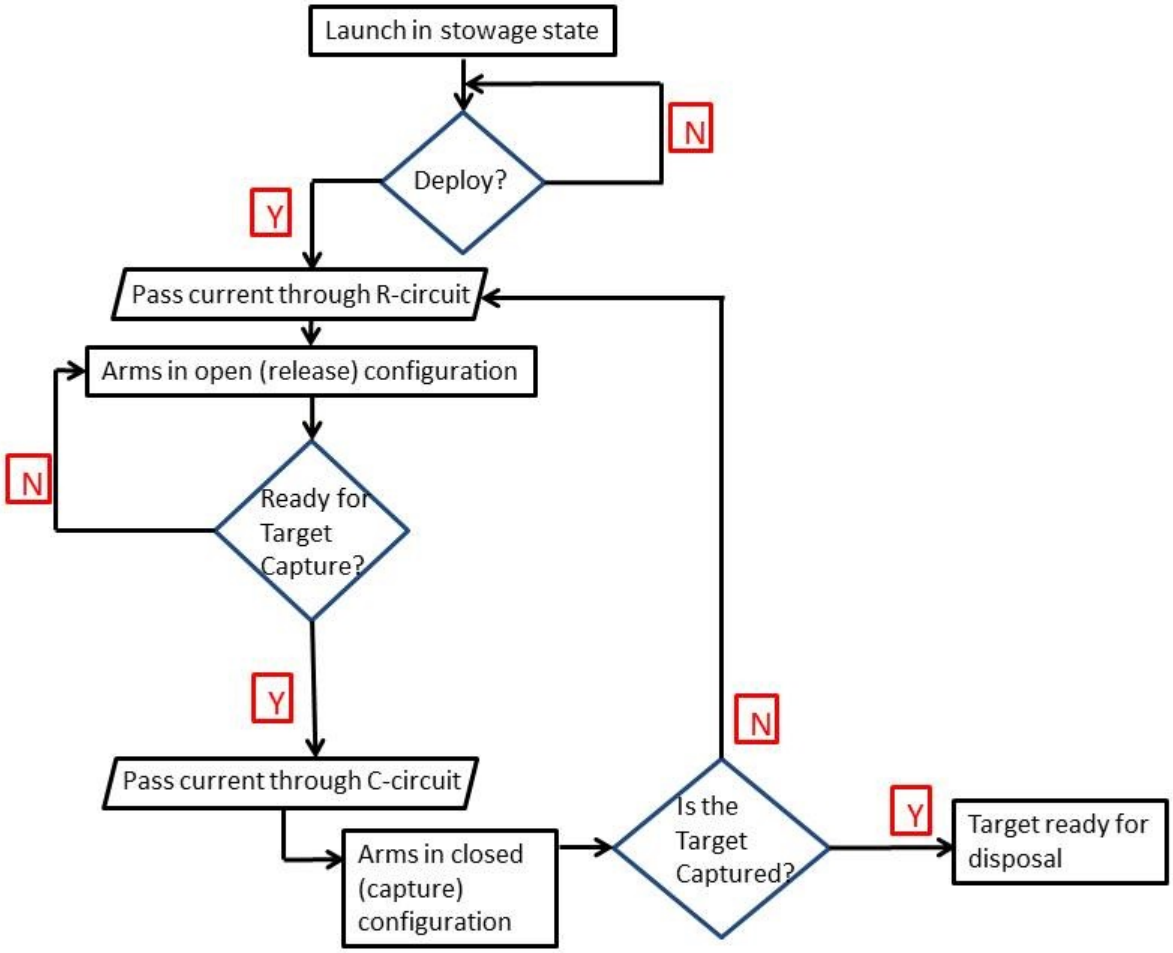

Figure 4.11 Functional flowchart of MEDUSA. Rectangular boxes indicate a state of MEDUSA, parallelograms indicate an action of MEDUSA, and the diamond-shaped boxes represent decision points to alter those states.

Chapter 5

Manufacturing of MEDUSA

In this chapter we describe the steps to manufacture the MEDUSA capturing arms. The development of the manufacturing process involved several iterations of trial-and-error. Once a single capturing arm was manufactured, we then duplicated the manufacturing process another four times. Each capturing arm consists of four components: two nitinol wire frames, a polyamide arm body and a Kapton HN sheath. Nitinol programming is described in Section 5.1 and a thorough investigation into the hysteresis effect inherent in nitinol is discussed in Section 5.2. At the end of this investigation an over-programming correction factor was calculated and applied to counter the hysteresis effect in nitinol wires. In Section 5.3 we show the laser cutting process on polyamide. The detailed process to assemble the arms is shown in Section 5.4. In Section 5.5 we demonstrate how the Kapton HN sheaths were made and a completed capturing arm is shown in Section 5.6. Finally, we show the manufacturing process of the arm mounting plates in Section 5.7.

5.1 Nitinol programming

Shape recovery tests were conducted on several nitinol wire frames with different dimensions in order to select the optimal wire gauge for the MEDUSA application. The purpose of these tests was to ascertain the recovery strengths and the required input current. After several laboratory experiments, measurements proved that nitinol wire of 1mm in diameter was capable of producing sufficient recovery forces with an amount of electrical power within the capabilities of the power system of a typical nanosatellite. The recovery force generated by the 1 mm nitinol wire was capable of enclosing the capturing volume in a laboratory environment of one g.

To ensure the precise and repeatable execution of capturing and release actions during operations, the activation temperature of the nitinol needs to be well defined to act sharply and only on demand. The activation temperature is customizable by most commercial providers of nitinol [30]. The activation temperature of the nitinol wire used for MEDUSA was selected based on the standard operating temperature range required by nanosatellite components to operate in LEO [31], also considering the external heat disturbances that

could possibly interfere with the MEDUSA system in the space environment, such as solar radiation.

After comparing different temperature ranges of nanosatellite components, the activation temperature for state transition was selected at 70°C. Once nitinol reaches the transition temperature, the state switches from a Martensite state to an Austenite state and during the state transition a recovery force is generated.

The nitinol wire had to be programmed at high temperature in a furnace. For this prupose we produced two programming moulds, one for the capturing circuit (closed arms configuration) with a "C" shaped profile, and the other with an "L" shaped profile for the release circuit (open arms configuration). These two program shapes were introduced in the mould by milling "C" and "L" shaped grooves into two flat mild steel plates, which comprised one half of each mould. Another flat mild steel plate was screwed to each grooved plate to close off the moulds. The standard operating temperature of mild steel goes up to 800°C, which covers the temperature range required to program nitinols.

The nitinol wires were carefully channelled into the grooves of the moulds. We then secured the shaped nitinol wire in the groove with Kapton tape to hold it firmly in place during shape programming. The cover plate was then placed on the grooved plate and the two plates were screwed together tightly.

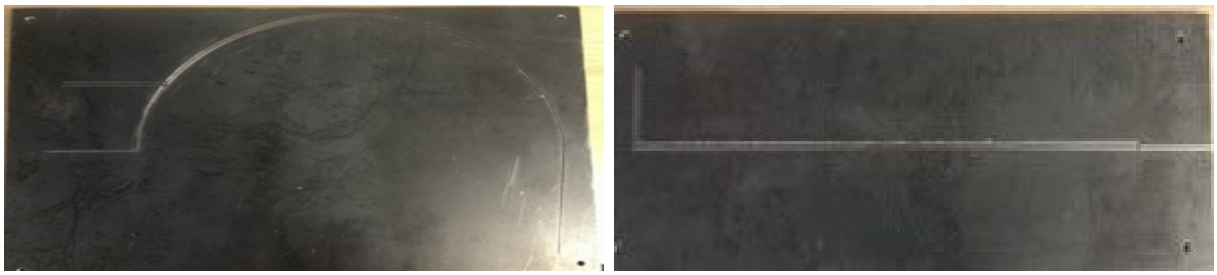

(a) "C" shape groove milled on mild steel plate to program nitinol for capture action.

(b) "L" shape groove milled on mild steel plate to program nitinol for release action.

Figure 5.1 Mild steel moulds made for nitinol programming.

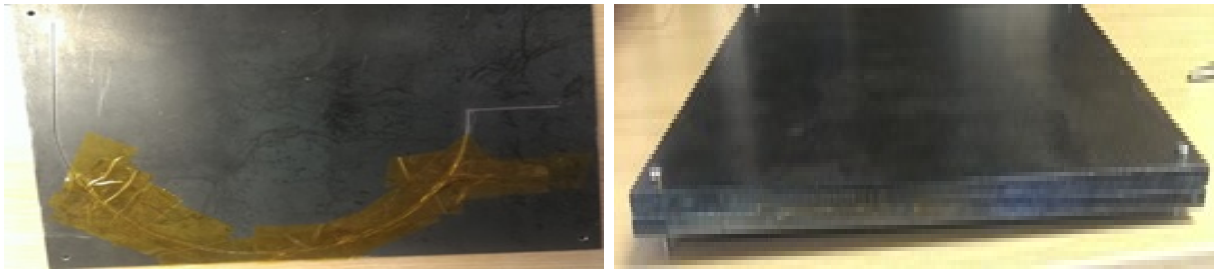

(a) Nitinol in mould secured with Kapton tape.

(b) Nitinol placed between the two mould plates, and secured with bolts and fasteners in the four corners.

Figure 5.2 Nitinol wires installed into "C" shape groove milled into mild steel plates for programming.

The procedure to program the nitinol wires is as follows. Once nitinol is completely fixed between two mould plates, it is placed in a furnace at standard room temperature. To begin the shape programming, we ramp up the furnace temperature from room temperature to 450 °C over a period of 45 minutes. We then maintain the furnace temperature at 450 °C for 90 minutes. It takes approximately 2 hours and 15 minutes to program one pair of "C" and "L" shaped nitinol wires.

Once the heating process completes, we take the mould out of furnace carefully, then place it in a room temperature environment to cool down gradually for 120 minutes. The air cooling is necessary for the nitinol to retain its flexibility. Rapid cooling, such as quenching in water, introduces a thermal shock that makes nitinol brittle and liable to snap when it is bent.

After the mild steel mould reaches room temperature, we separate the two plates, remove the remnants of burnt Kapton tape with a damp cloth and take out the programmed nitinol. Freshly programmed nitinol has an oxidization layer formed on the nitinol surface during heat programming, which must be removed. The oxidization layer is removed by abrading the nitinol with fine-grained sand paper. Removal of the oxidization layer is essential in order to form good electrical connections.

We then conduct a shape restoration test, done by passing an electrical current through the programmed nitinol. If the shape recovery is satisfactory we then place a new set of nitinols into the moulds for the next round of programming. This process is repeated until 10 "C" shaped nitinol loops and 10 "L" shaped nitinol loops are produced to make up the five capturing arms.

(a) Furnace used for shape programming.

(b) Once shape programming is completed and the mould has air cooled to room temperature, we remove the burned Kapton tape with a wet cloth.

Figure 5.3 Final two steps to complete nitinol shape programming.

5.2 Investigation of hysteresis effect and nitinol over-programing

With repeated deformation and recovery, nitinol gradually starts losing its ability to recover fully to the programmed shape (an effect known as hysteresis) and this worsens with time. The hysteresis effect causes degraded shape recovery to approximately only 80% of the original programmed shape.

During the course of many tests, we established that the hysteresis effect manifests mainly in the distal half of the capturing arm. Even after 20 to 30 actuations we could not discern any deviation in the shape recovery in the proximal part of the arm (Fig 5.4). The "Deviation Point" refers to the point of the arm at which the hysteresis effect is discernible.

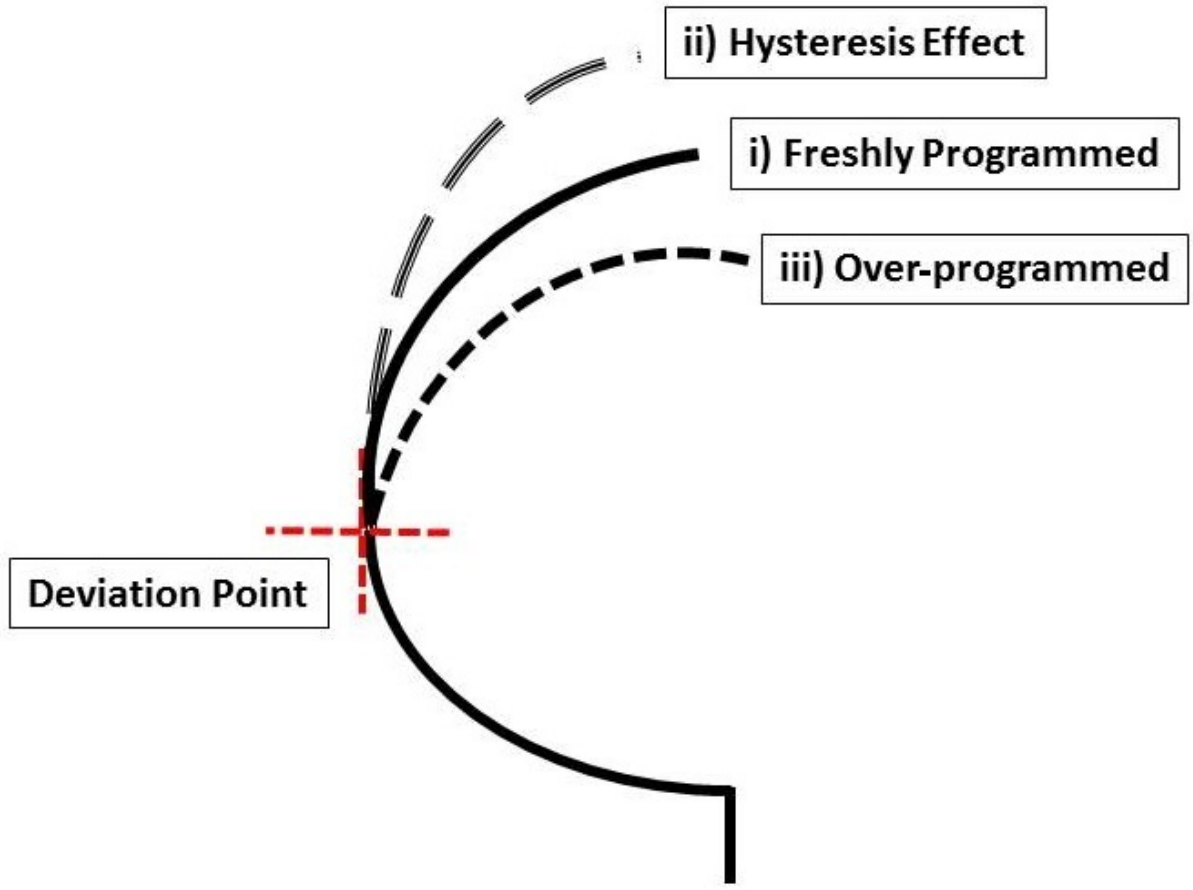

Figure 5.4 Comparison of three capturing shapes of nitinol: (i) Freshly programmed nitinol, (ii) Degraded nitinol due to the hysteresis effect and (iii) Over-programmed nitinol. The shape restoration degradation due to hysteresis starts at the deviation point and the over-programming is used to rectify this degradation.

Table 5.1 records the differences between the programmed profile and the achieved profiles caused by the hysteresis effect. These values were measured on degraded nitinol wires and compared to shape recovery of freshly programmed nitinol before measurable hysteresis started to take place.

To ensure the calculated capturing volume can be enclosed after 10 activations with hysteresis taking place we calculated a correction factor and applied it in the shape programming (Fig 5.5). The correction factor over-programs the capturing nitinol, which shrinks the capturing volume at first, but after several deployments the hysteresis will take place and return the shrunk capturing volume back to the initial target capturing volume. Correction factors are calculated by:

$$y_c = (y_d - 1) \cdot 0.8 \tag{5.1}$$

where y_c is the required over-programming correction and y_d is the degraded vertical position.

Table 5.1 *Deflection of nitinol due to the hysteresis effect was measured and compared to the ideal vertical position and the vertical position after a correction factor has applied. These values were measured using a nitinol loop after* > 20 *activations.*

Position along length of wire	l	0	1	2	3	4	5	6	7	8	9	10	11	12
Ideal vertical position [cm] **(Freshly programmed)**	y_i	0	0.5	1	1.3	1.5	1.6	1.8	2	2.2	3	3.4	4	4.4
Degraded vertical position [cm] **(Hysteresis)**	y_d	0	1.5	1.6	1.8	1.9	2	2.2	2.7	3	3.5	4.2	4.3	4.6
Required over programming correction **(Over programmed)** [cm]	y_c	0	0.42	0.48	0.6	0.66	0.72	0.84	1.14	1.32	1.62	2.1	2.1	2.28

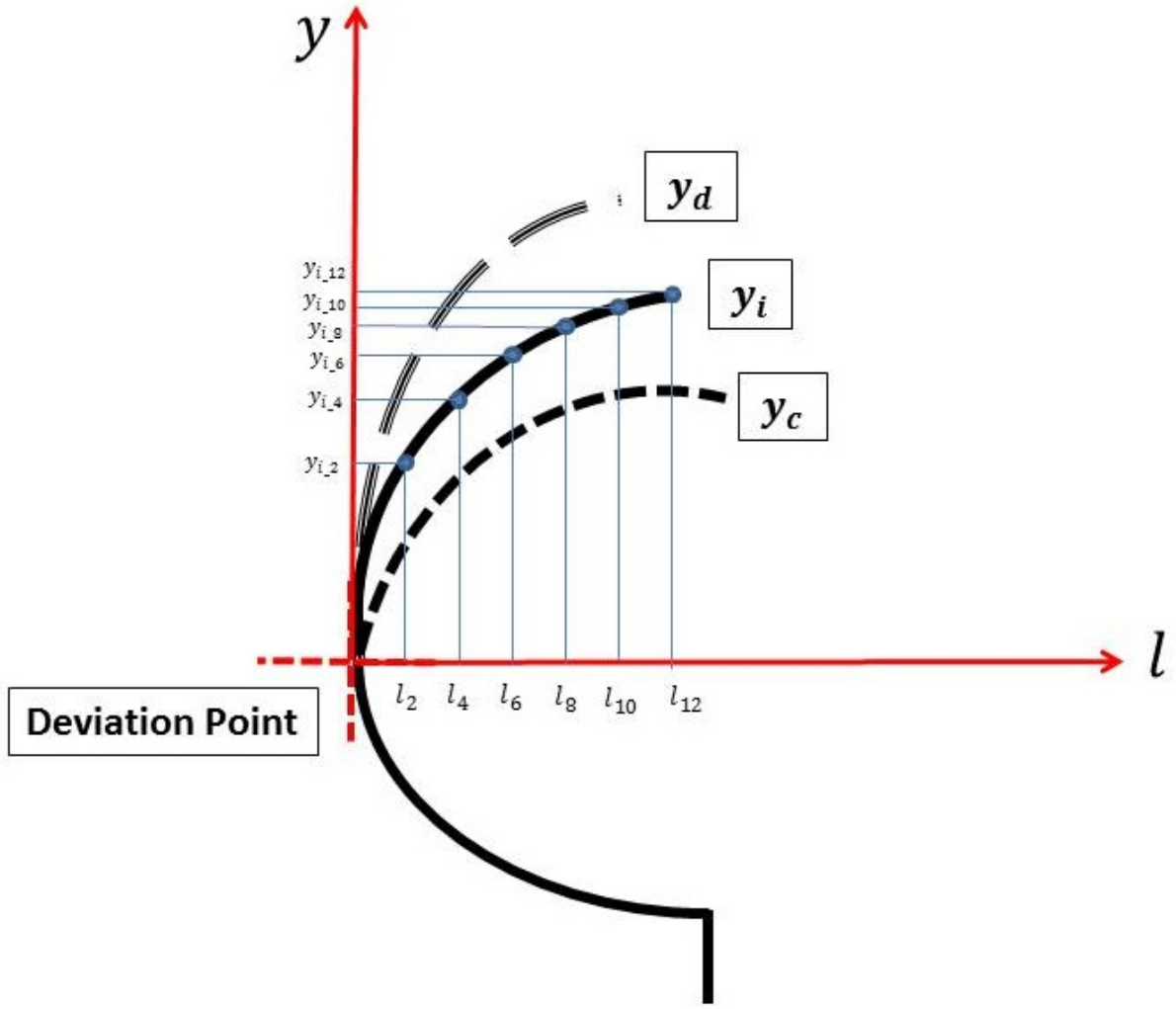

Figure 5.5 Indication of l points along the horizontal axis with corresponding y values on the vertical axis. This figure shows horizontal and vertical values of segments of lengths along a freshly programmed nitinol wire.

5.3 Polyamide laser cutting

The pattern designed in Section 4.3.4 was laser-cut on a rectangular polyamide strip of dimension 6 cm by 37 cm, and thickness of 0.5 mm. After discovering that the edges of the polyamide burned after laser cutting, a dimension bigger than required was extracted from a sheet of polyamide to provide extra room for a neater laser cutting process.

Figure 5.6 Laser-cutting removes 43% of the initial mass from the polyamide strip of dimension of 6 cm by 37 cm. The laser cut arrows are folded into designated slots to form loops through which the nitinol wires are threaded.

5.4 Component integration

To begin component integration four programmed nitinol wires are threaded through the loops in a polyamide strip. At the base of a capturing arm the nitinol wires are connected electrically to the power system with clamps. These are 4 connections per arm, two for the R-circuit and two for the C-circuit. We connect the electrical wires to the nitinol by clamping both with a metal joint, which provides a rigid attachment point for these components. This form of clamped connection mechanism is preferred rather than soldering because nitinol is difficult to solder, even after the oxidization layers are removed. Solder joints with nitinol tend to break and thus create unreliable connections. The electrical connections are shown in Fig 5.7.

(a) Nitinol embedded into laser-cut polyamide. Channels to secure the nitinol were formed by folding the laser-cut arrows into slots.

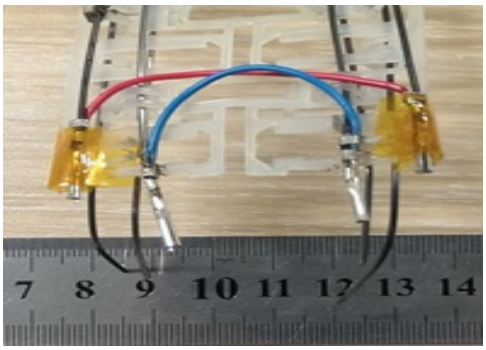

(b) Electrical connections of the nitinol wire frames with the power system. Total width: 6 cm.

Figure 5.7 Nitinol wire frame threaded through the polyamide arm and electrical connections

Lastly, to strengthen the clamped connection between the nitinol wire and electrical wire, we apply an epoxy mixed with hardener at a ratio of 100 : 20. This liquid is applied onto every joint on the capturing arms. It takes approximately eight hours to dry. Once dried, it is no longer possible to separate the connections.

Figure 5.8 Epoxy resin and hardener mixed at a 100:20 ratio measured on a precise digital scale. This liquid also insulates the metal joints electrically.

5.5 Manufacturing of Kapton HN sheaths

We use Kapton HN sheets with a thickness of 25μm to manufacture the protective sheaths that encase the arms. Kapton HN is well known for its high melting point, and its thermal and electrical insulation ability. Furthermore, Kapton HN is difficult to penetrate; it protects the capturing arm from possible damage of sharp corners or protruding components from target debris.

The Kapton HN sheet is cut into strips of 40 cm by 14 cm in dimension, folded over and sealed with Kapton tape. Each capturing arm is covered by an identically made Kapton sheath.

The datasheet for Kapton is included in Appendix A.4.

5.6 Final assembly of a capturing arm

A completed capturing arm shown in Figure 5.9b, which may be compared comparing to the conceptual design schematic shown in Figure 5.9a. One capturing arm takes approximately three days to manufacture. Component manufacturing takes two days and assembling all the components together takes roughly one day. To assemble all the electrical and mechanical connections takes about three hours, but it takes eight hours for the epoxy to dry.

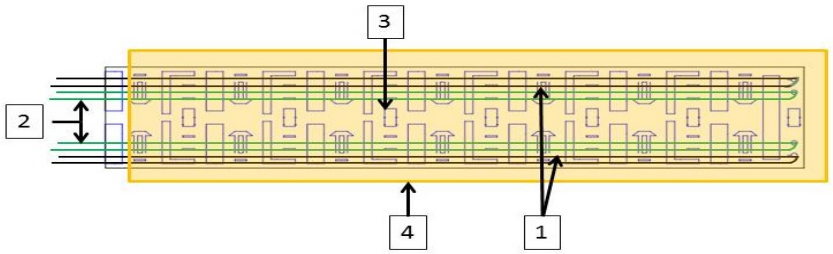

(a) Integrated conceptual design of the MEDUSA arm. 1- "C" shaped nitinol frame, 2- "L" shaped nitinol frame, 3- "body" made out of polyamide and 4- "sheath" made out of polyimide.

(b) A completed capturing arm of MEDUSA.

Figure 5.9 Comparison between the conceptual design of a MEDUSA capturing arm with the actual manufactured capturing arm.

5.7 Manufacturing of the arm mounting plates

The arm mounting plate provides a rigid attachment point for the capturing arms. It also provides an attachment point for the electrical connections that supply power to the arms.

We considered several possible materials for this component, namely PLA, chemically processed bamboo, and polyamide. Prototypes were constructed from each of these materials. Mk-1 (Figure 5.10) was constructed from laser-cut polyamide. Mk-2 (Figure 5.11) was constructed from chemically processed bamboo and Mk-3 (Figure 5.12) was constructed from 3-D printed PLA. Table 5.2 shows the mass properties of these three prototypes.

We tested these three prototypes with an experimental capture and release test to assess their performance. Observations recorded during the experimental tests are documented in Table 5.3.

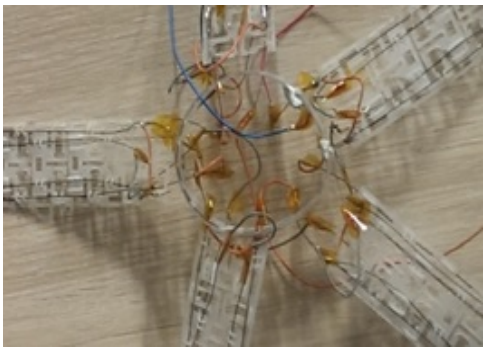

(a) Arm mounting plate-Mk1 shaped with polyamide.

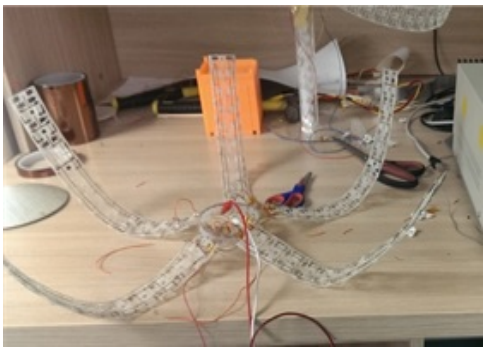

(b) Arm mounting plate-Mk1 in release mode. This version had a circular arm-mounting plate with five capturing arms. This prototype was made solely with polyamide.

Figure 5.10 MEDUSA arm mounting plate-Mk1.

(a) Arm mounting plate-Mk2 made with chemically processed bamboo.

(b) Arm mounting plate-Mk2 in release mode: Chemically processed bamboo plate connected to the 5 capturing arms.

Figure 5.11 MEDUSA arm mounting plate-Mk2.

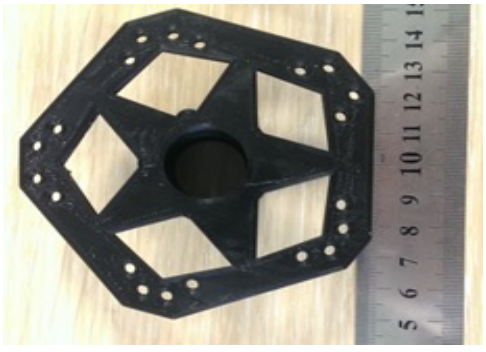

(a) Arm mounting plate-Mk3 made with 3-D printed PLA.

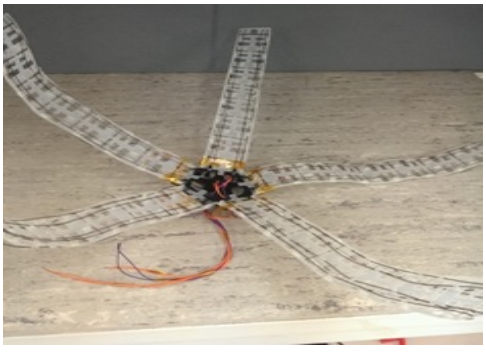

(b) Arm mounting plate-Mk3 in release mode: 3-D printed PLA arm-mounting plate connected to the five capturing arms.

Figure 5.12 MEDUSA arm mounting plate-Mk3.

Table 5.2 *Mass of prototype MEDUSA arm mounting plates.*

Mass of each components	MEDUSA-Mk1	MEDUSA-Mk2	MEDUSA-Mk3
1 Arm-mounting plate	11 g	15 g	36 g
5 Capturing arm	130 g	130 g	130 g
5 Protection Cover	9 g	9 g	9 g
Total	150 g	154 g	175 g

A set of preliminary capture and release tests was conducted in the laboratory environment to determine which of the prototypes could satisfy the basic requirements. The test results recorded during the tests are listed in Table 5.3.

Table 5.3 *Functional performance test results for MEDUSA Mk1, Mk2, Mk3 arm mounting plate prototypes.*

Prototype	Open and Close	Anomaly Occurred	Comments
Mk1 Polyamide	Unable to complete both open and close operations.	Insufficient rigidity to support the capturing arms firmly.	Polyamide is too soft and thus unsuitable to be used for the arm mounting plate.
Mk2 Bamboo	Able to complete both operations.	No problems noted.	This material has high thermal resistance, however, due its rigidity, a complex arm mounting plate design cannot be manufactured from this material.
Mk3 PLA	Able to complete both operations.	Material seems to soften as temperature rises above a certain level.	This material is easy to work with, but has poor heat resistance. Fine for mechanical prototyping, but should investigate alternative heat-resistant materials that can also be 3-D printed.

The advantages of using 3-D printing are shortened manufacturing time and ease of manufacturing. PLA is the best 3-D printing material to make the arm mounting plate, but it only offers limited heat resistance. As for other components such as the square base, it is also advisable to manufacture them using material that tolerates higher temperatures than PLA.

Based on our test results we selected MEDUSA-Mk3 as our prototype for further development.[1] Our selection was based on ease of manufacture, the time taken to complete the manufacturing process and the ability to support the capturing arms. Figure 5.13 shows the integrated base unit mounted on a 1U CubeSat. Figure 5.14 shows the fully

[1]The Mk2 version was used to perform the simulated capture test shown in Fig 6.6.

integrated MEDUSA-Mk3 prototype with arms attached. This prototype was used in the tests reported in Chapter 6.

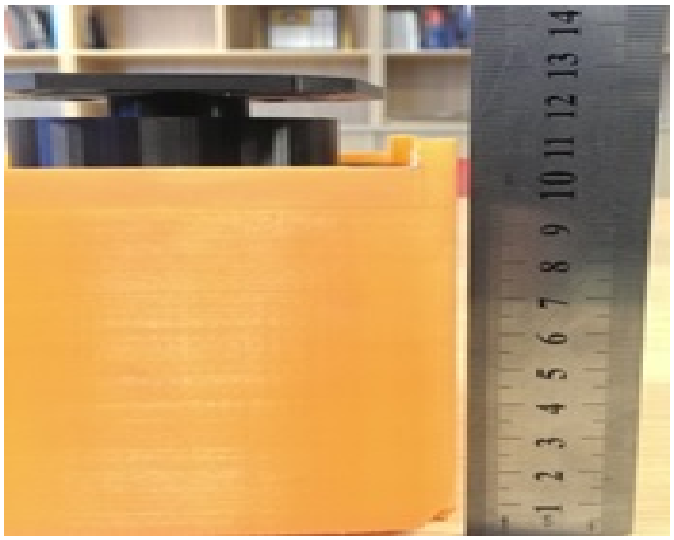

Figure 5.13 3-D printed PLA integrated base shown fitted to a mock-up of a 1-U CubeSat. Total height 131 mm.

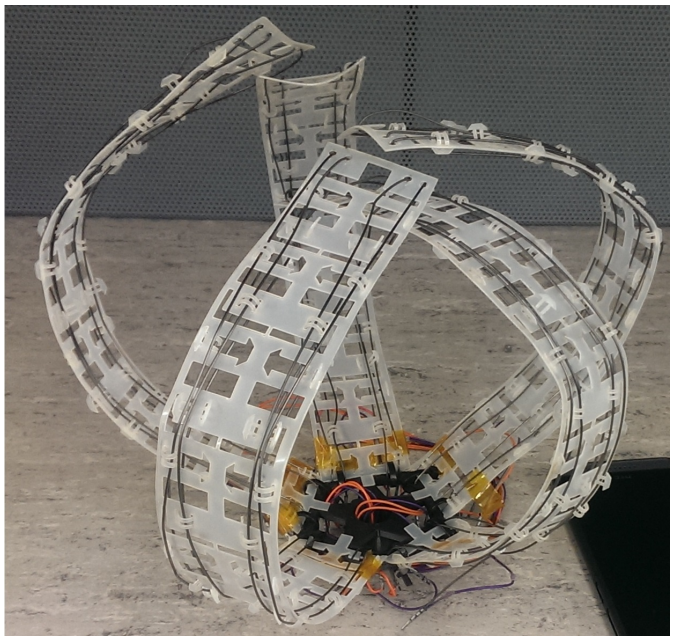

Figure 5.14 Final fully integrated MEDUSA – Mk3 in capture mode.

Chapter 6

Testing results

In this chapter we describe a series of tests that were conducted on the MEDUSA system. In Section 6.1 we describe a detailed single-arm test that was carried out to evaluate the performance of the arms of MEDUSA. In Section 6.2 we discuss tests to simulate capture and release operations of MEDUSA in a laboratory environment. In Section 6.3 we describe a test to determine the mechanical force generated during the state transition in nitinol while performing a closing action of a MEDUSA arm.

In Sections 6.4 to 6.10 we describe the tests conducted in a vacuum chamber at the Institut für Raumfahrtsysteme (IRS) at the University of Stuttgart. Data from vacuum tests provide valuable insights on the behaviour of MEDUSA when it is operated in the vacuum of space. In Section 6.10 we describe motion data captured during vacuum tests that allows detailed analysis of the movement of a capture arm of MEDUSA while executing capture and release actions.

6.1 Single capture arm test

The aim of this test is to record the time taken for a single capturing arm to fully restore to the programmed capture and release shapes. The test rig shown in Figure 6.1a consists of a base on which MEDUSA can be supported firmly during the test and a graduated backboard for measuring the positions of points along a capturing arm. The backboard is in the shape of a quarter of a circle and is made out of a perspex sheet to which a paper sheet with a grid is fixed. The grid squares on the sheet are 1 cm by 1 cm and are marked in white and grey for improved visibility. Also highlighted for improved visibility is the 45° line, which was used as the starting/ending arm position for the closing/opening tests respectively.

To set up the test, the third capturing arm (Arm 3) of MEDUSA was placed right below the 45° line shown in Figure 6.1a. To begin the test, power was supplied to the Capture-circuit (C-circuit) of Arm 3 and we recorded the time taken to complete the capture action when the tip of Arm 3 touched the vertical line shown in Figure 6.1b. We then waited for a cool-down period of 50 seconds. (The 50 seconds cool-down time ensures the residual recovery force in the nitinol decays as its temperature drops). After the cool down period

we then supplied power to the Release-circuit (R-circuit) until the entire Arm 3 was below the 45° line and back to the starting position again. We repeated the test with various input voltages and currents to the C-circuit (Table 6.1) and to the R-circuit (Table 6.2). The power supply used was a Topward DC power supply, model 33010D. The voltage and current measurements were acquired using an Agilent 34405A $5\frac{1}{2}$ digital multimeter with measurement uncertainty of 0.058 Ω over the range of resistance measured.

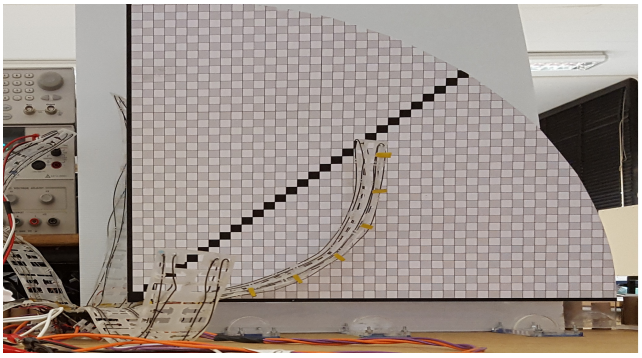

(a) Starting open configuration of the arm at the start of the test.

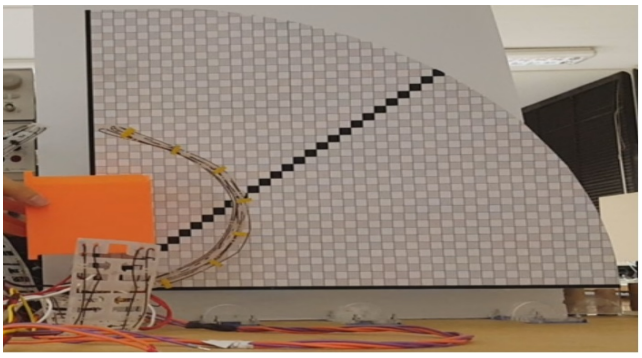

(b) Fully closed configuration, $Tc_{100\%}$.

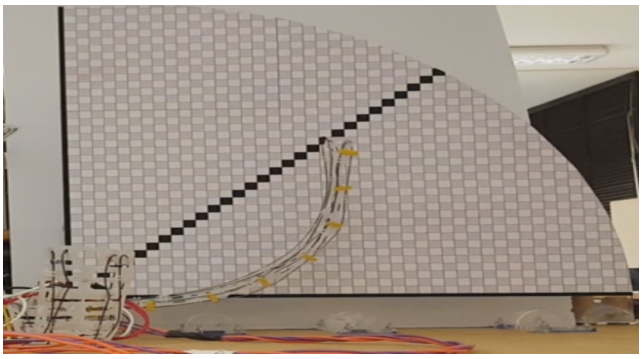

(c) Fully open configuration at the end of the test, $Tr_{100\%}$.

Figure 6.1 The entire test procedure of the single-arm test. The test commences with the open starting configuration (a). Power is supplied to the MEDUSA arm until it reaches the closed configuration (b). After a cool-down period of 50s, power is applied to reopen the arm to the release position shown in (c).

We conducted a series of tests with input voltages in the range of 1-10 V. These tests were performed in order to decide the input current and voltage to be used for the actual operation of MEDUSA in space. Owing to the length of the power cable used in this test, we observed voltage losses along the cable from the power supply to Arm 3 and from Arm 3 to the instrumentation. Voltage loss occurred during these tests because of resistance induced over the lengths of power cables used. The voltage loss is the numerical difference between **Input Voltage** and **Voltage** shown in Table 6.1 and Table 6.2. In Table 6.1 the voltage loss was 17.64% on average and in Table 6.2 voltage loss was 25.57% on average. Voltage losses were in the range of 0.15 - 1.91 V in Table 6.1 and 0.28 - 2.09 V in Table 6.2.

Table 6.1 *Closure times of the C-circuit for various voltages and currents. Average resistance of C-circuit: 1.45 Ω.*

Input Voltage (V)	**Voltage (V)**	**Current (A)**	**Resistance (Ω)**	**Error (%)**	$Tc_{100\%}$ **(s)**
1	0.85	0.58	1.461	3.1	No Movement
2	1.69	1.17	1.446	0.0	No Movement
3	2.45	1.75	1.403	2.9	No Movement
4	3.23	2.24	1.440	0.4	No movement
5	4.15	2.84	1.460	1.0	117
6	4.96	3.38	1.456	0.7	27
7	5.76	3.98	1.446	0.0	14.8
8	6.55	4.55	1.439	0.5	13.2
9	7.29	4.97	1.468	1.5	8.4
10	8.09	5.61	1.443	0.2	6.7

Table 6.2 *Opening times of the release circuit for various voltages and currents. Average resistance of R-circuit: 1.29 Ω.*

Input Voltage (V)	**Voltage (V)**	**Current (A)**	**Resistance (Ω)**	**Error (%)**	$Tr_{100\%}$ **(s)**
1	0.72	0.86	1.210	6.2	No Movement
2	1.24	1.52	1.224	5.2	No Movement
3	2.39	1.73	1.397	8.2	No Movement
4	2.80	1.80	1.414	9.6	No movement
5	3.84	2.90	1.325	2.7	40
6	4.45	3.64	1.222	5.3	28
7	5.22	4.40	1.186	8.1	13
8	5.91	5.02	1.177	8.8	12
9	7.29	5.22	1.381	7.0	9.6
10	8.02	5.85	1.370	6.2	3.1

For the C-circuit we recorded the input voltage (**Input Voltage**), the voltage drop across the C-circuit of Arm 3 (**Voltage**), the input current and the time taken for the arm to fully restore to the programmed capture shape $Tc_{100\%}$. We also calculated the resistance for each test and its percentage of deviation from the average resistance calculated based on data obtained to verify measurement accuracy. The same parameters were recorded for the R-circuit listed in Table 6.2, where $Tr_{100\%}$ denotes time taken for the arm to restore to the programmed release shape[1].

Figure 6.2 shows the relationship between the input current and the nitinol resistance of the C-circuit, calculated based on data in Table 6.1 using Ohm's law. The purpose of this test is to check for temperature-induced variation in nitinol resistance subject to different input currents. Figure 6.3 shows the same relationship for the R-circuit using data from Table 6.2.

Theoretically, resistance values change at different temperatures based on material characteristics. Temperature is a crucial factor for the operations of MEDUSA as it decisively changes the response time of shape restoration due to the fact that movement is driven by the raising of temperature in the nitinol wires and thus input current directly effects the response time.

Figure 6.2 shows that the resistance value did not differ significantly for the range of input voltage and current used in this test (Table 6.1). The average resistance value of the C-circuit was 1.45Ω. The numerical differences between individual resistance values and the averaged resistance value was not substantial. This leads to the conclusion that temperature variation within the nitinol driven by different current strengths has no significant effect on resistance at the voltage and current levels of these tests.

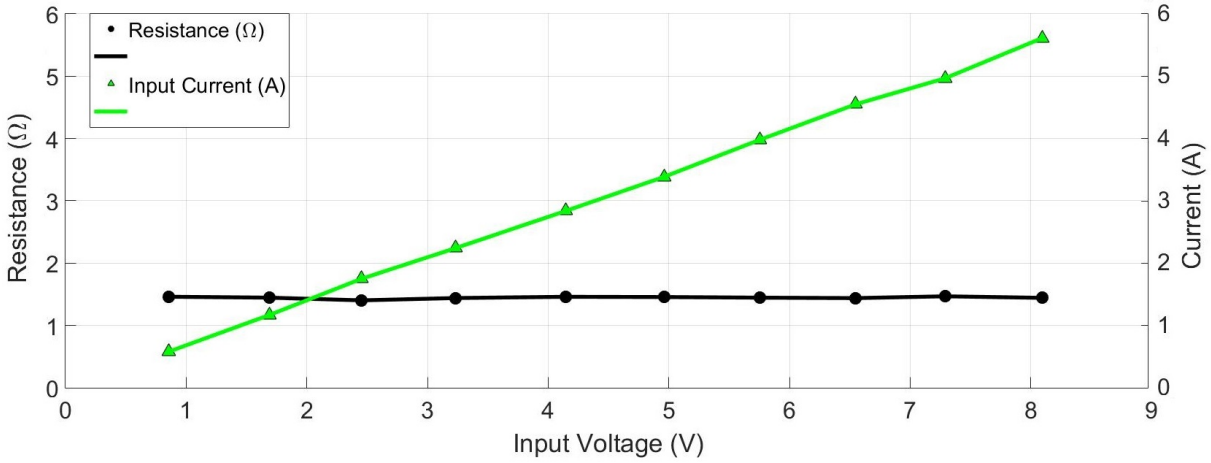

Figure 6.2 Current and resistance behaviour of the C-circuit as a function of input voltage in an atmospheric environment.

[1]After several executions we observed that the capture arm will not fully restore the "L" shape, especially in the distal part of the arm, which remain curved upwards after a "C" shape restoration. Nevertheless, as seen in Figure 6.1c the opened up capturing volume was large enough for a next capture attempt.

Figure 6.3 shows the relationship between resistance of the R-circuit over the range of input voltage and current listed in Table 6.2. The R-circuit has an average resistance value of 1.29Ω, which is 11% less than the C-circuit resistance, because the nitinol used in the R-circuit is 3.15 cm shorter than the nitinol wires used in the C-circuit. Also, the R-circuit exhibited a slightly higher variation in resistance value compared to C-circuit. The reason for this anomaly is not understood at present.

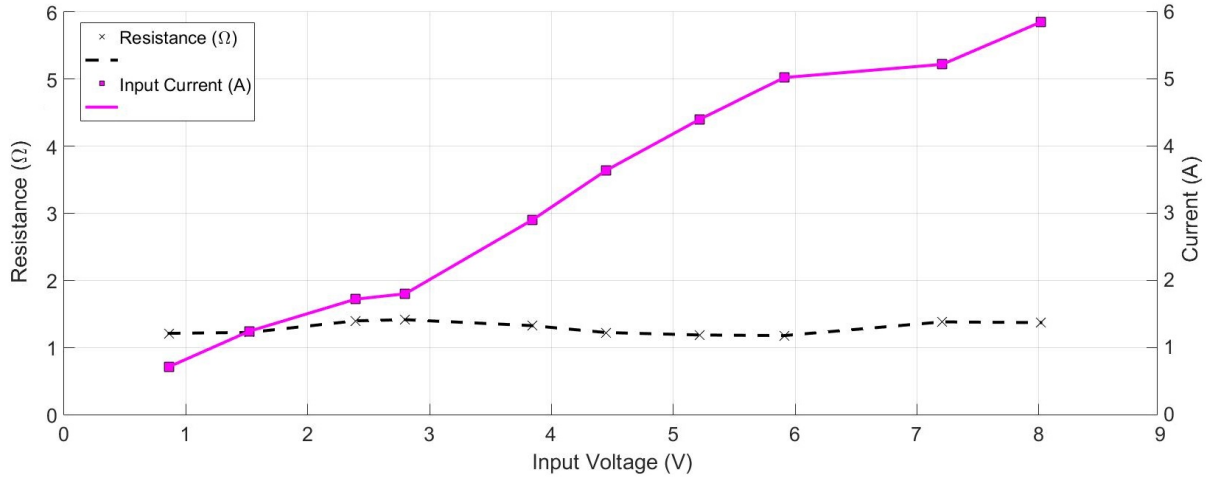

Figure 6.3 Current and resistance behaviour of the R-circuit as a function of input voltage in an atmospheric environment.

In the single-arm test the largest difference between individual resistance values and averaged resistance value was 3.1% for the C-circuit and 9.56% for the R-circuit. These ranges of resistance variation do not impose a significant change in shape restoration response time as no variations in resistance were higher than 10%. From these two series of measurements we can conclude that the resistance values of the C-circuit and R-circuit have been accurately determined. The Resistance values of C-circuit and R-circuit as a function of input voltage are compared in Figure 6.4.

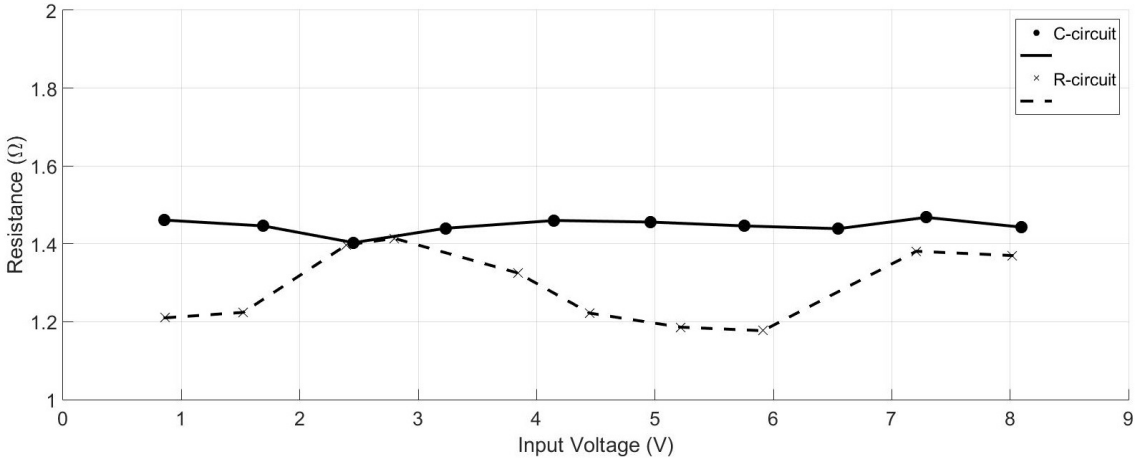

Figure 6.4 Resistance values of the C-circuit and R-circuit at various input voltages in a room temperature atmospheric environment at sea-level.

Data extracted from Table 6.1 and Table 6.2 plotted in Figure 6.5 shows the time taken to complete shape restoration as a function of the input current. In Figure 6.5 we can see that no shape recovery occurs below 2.8A. The capturing arm begins to move smoothly at about 3.5A and takes 27 seconds to restore the capture shape and 28 seconds to restore the release shape, which does not satisfy the capture time requirement of completing the capturing action within 10 seconds. From the test data we concluded that the 10-second time requirement could not be fulfilled by any current below 5A.

From all data obtained we conclude that the supply voltage must be at 9V, which gives a 7.25V drop across each capturing arm that draws 5A of input current to fully enclose the capturing volume in 8.4 seconds and to fully open up the capturing volume in 9.6 seconds. These current and voltage values were set as the default supply for further tests and operations.

It is possible to open and close the MEDUSA arms in a shorter time than this, but a balance must be found between the current drawn, the ability of the materials to withstand high temperatures and the ability of a CubeSat power system to supply the required power levels. For example, a supply voltage of 10V that gives a 8V drop across the capturing arm while drawing 5.61A allows for a quicker response of 6.7 seconds for capture and 3.1 seconds for release, but such a high current supply required from a CubeSat power system may not be feasible during space missions. Moreover, high current input could result in damage to the polyamide body of the arm because high temperature nitinol could melt through polyamide to permanently damage the hardware and negatively influence further operations.

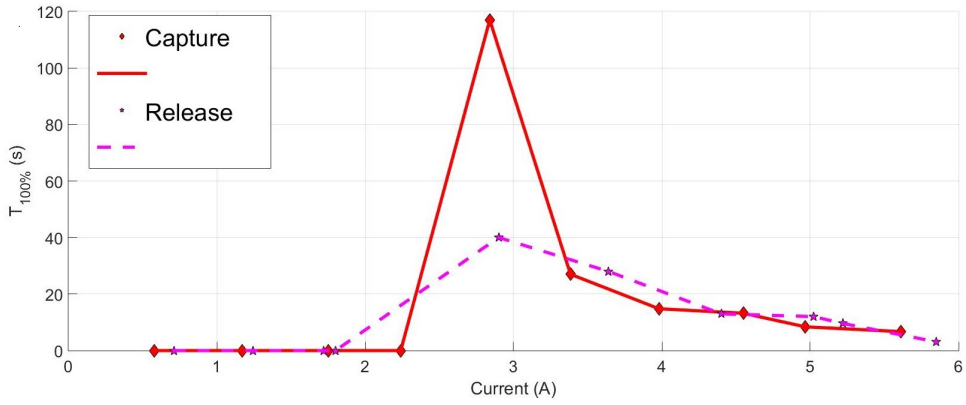

Figure 6.5 Time taken to complete the capture action by the C-circuit and the release action by the R-circuit per current increment in a room temperature atmospheric environment at sea-level. Below 2.8A no shape recovery occurred in either the C-circuit or the R-circuit. Higher current input leads to shorter time required for shape recovery.

6.2 Simulations of capture and release of a target by MEDUSA in atmospheric conditions

The capture and release test was performed in a 1g laboratory environment to obtain a preliminary view of a simulated debris capturing mission using MEDUSA. The simulated target was a 3-D printed 1-U CubeSat model, suspended on a nylon fishing line. During the test, the target was tumbled by hand to simulate rotation on a fixed axis.

From the single-arm tests it was established that 5A is needed for a single arm to transition from the fully open configuration to the fully closed configuration within 10 seconds. Since the five capturing arms are wired into two parallel branches, each branch requires 5A. Thus the total input current used was 10A.

The recording of capturing time began when the power supply to the C-circuit was switched on and ended when the target was fully enclosed. The recording of release time began when power supply to the R-circuit was switched on and ended when full shape restoration was completed.

During the capture and release test the cool-down time was also recorded. Cool-down is used to describe the time required for the nitinol temperature to decay below its activation temperature until no residual force is exerted by the nitinol wires. Residual forces are exerted while nitinol stays in the Austenite state A_s when its temperature is above the activation temperature. During the cool-down time thermal exchange between the nitinol and the ambient background continues until an equilibrium temperature is reached. In the laboratory where the capture and release tests were conducted the ambient temperature was approximately 24°C.

The capture and release test procedure was as follows:

Step one- The target was held 1 metre away and tumbled by hand.

Step two- We slowly approached the target and switched on the DC power supply connected to the C-circuit to capture the tumbling target.

Step three- After approximately 8s the target was trapped inside the capturing volume. We then waited for a 40-second cool-down period.[2]

Step four- To test the release action we supplied current to the R-circuit.

Step five- After the R-circuit opened the arms to the open configuration, the capture and release test was complete.

The capture and release test was repeated three times. The capture time, release time and cool-down time, recorded together with input voltage and current for these three tests, are listed in Table 6.3.

[2]The astute reader may notice that this cool down time is shorter than the 50s cool-down time described in Section 6.1. The test described here was conducted before the test described in Section 6.1 and the cool down time was determined by trial and error. We tried cool down times of 40s, 50s and 60s. In various tests and eventually settled on a cool-down time of 50s as optimal for this application.

Test results were satisfactory as two test criteria were successfully fulfilled. Firstly, the capture and release actions were executed successfully several times. Secondly, the times taken to complete the three capture / release actions were consistent. The times recorded for the capture and release actions in all three tests did not deviate from each other significantly. This consistency is important for predictable and reliable operation of MEDUSA in space.

Table 6.3 *Data from capture and release test.*

Measurement	**Test 1**	**Test 2**	**Test 3**	**Average**
Input Voltage	18 V	18 V	18 V	18 V
Input Current	10.2 A	10.2 A	10.2 A	10.2 A
Time for Capture Test	9.4 s	8.2 s	7.7 s	8.4 s
Time for Release Test	13.1 s	12.6 s	14.2 s	13.3 s
Cool-Down Time	45 s	50 s	50 s	48.3 s

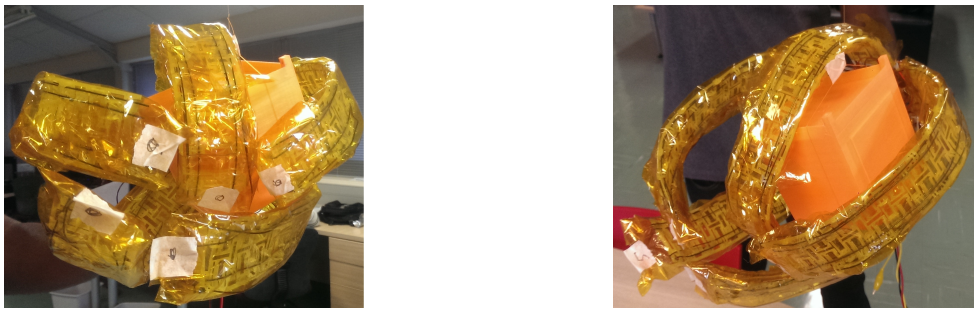

Figure 6.6 The capturing mode executed smoothly several times during the tests and successfully trapped the target inside the capturing volume. The image on the left shows the front view of MEDUSA-Mk2 in the fully closed configuration and the image on the right shows the side view of MEDUSA-Mk2 in the fully closed configuration.

Figure 6.7 The release mode executed smoothly several times during the tests and the opened capturing volume was large enough for the target to escape and available for a second capturing attempt. The image on the left shows the front view of MEDUSA-Mk2 in its open configuration. The image on the right shows the side view of MEDUSA-Mk2 in its open configuration.

6.3 An investigation into the force generated by the C-circuit in capture actions

The purpose of this test was to determine the intrinsic force produced by the C-circuit during a state transition while executing a capture action. To set up the test, we attached a spring k_s onto the 5th yellow marker of the third capturing arm (Arm 3) as shown schematically in Figure 6.8. The position of the 5th yellow marker corresponds to the "Deviation point" in Figure 5.4 discussed in Chapter 5. It is the point beyond which the hysteresis effects in the distal part of the arm become significant. The tension profile of spring k_s is shown in Figure 6.9. The spring constant for k_s was obtained by conducting several spring extension measurements using a series of known masses. After several measurements we calculated spring constant k_s of 0.1262 N/mm.

The pulley-and-fishing line arrangement k_f was used to transmit the force from the moving measurement point $\boxed{5}$ on the MEDUSA test arm to the horizontally mounted spring k_s. This was designed to have negligible effect on the measurements. The gauge of the fishing line used stretches 0.47 mm for every 15.91 kg load attached onto it, this yields a spring constant k_f of 332.08 N/mm. The value of k_f is thus 12769 times larger than the spring constant k_s which is 0.026 N/mm. Hence the extension caused by the spring constant k_f is negligible compared to the measurements of the extension from spring k_s.

The extension of the spring was measured physically with a vernier calliper and each extension was measured three times to compensate for random measurement errors. To determine the time taken for the capturing arm to induce maximum force we recorded the time taken for the index pointer fixed on the spring to attain its final length where no further movement occurred by reading off the position of the index pointer against a steel ruler engraved with 0.5 mm graduations. The physical set up for this test is shown in Figure 6.10.

The measurement point on Arm 3 was chosen to be the 5th yellow marker, where the maximum bending force is induced to enclose the capturing volume. The voltage supplied in the test ranged from 1-10 V in increments of 1 V. Between every test a one-minute cool-down time was applied. Test data from the strength test is tabulated in Table 6.4. Parameters documented are: input voltage, current, time, final spring length, maximum extension and maximum force induced by the C-circuit calculated based on the spring constant of k_s.

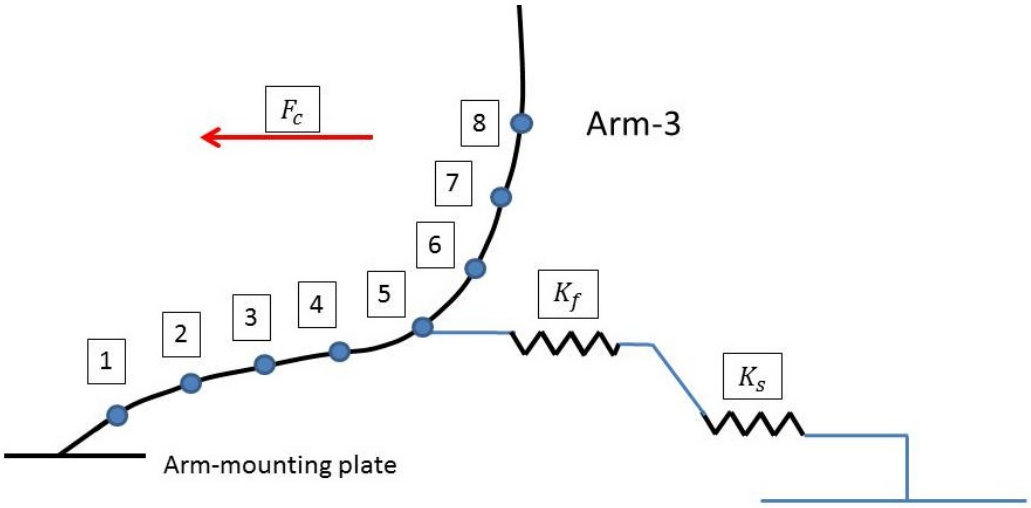

Figure 6.8 Schematic of the experimental set-up for the strength test. The numbers in the squares are the numbers of yellow markers placed evenly along the length of Arm 3 to facilitate observation of the arm's motion along its length. The same numbers are marked onto the yellow tags attached onto Arm 3 in the same order shown in Figure 6.10. F_c is the force generated by the C-circuit while enclosing the capturing volume.

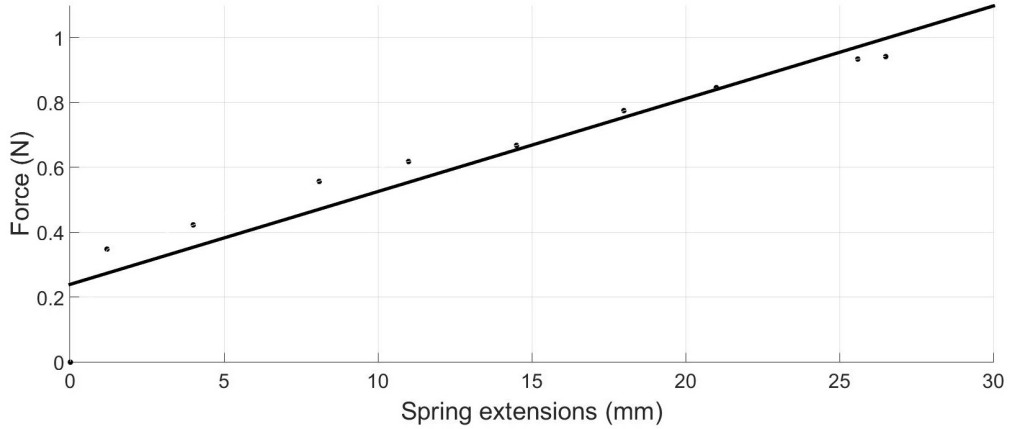

Figure 6.9 Determination of spring constant k_s.

The values in the **Time** column in Table 6.4 were determined based on videos of each test recorded by the Video Recorder shown in Figure 6.10. We inspected the videos to determine when no further movement occurred beyond a given spring extension length while electrical power was supplied. The final spring length was measured physically with a vernier calliper instead of readings from the video footage, because of parallax errors that occurred during filming with video recorder.

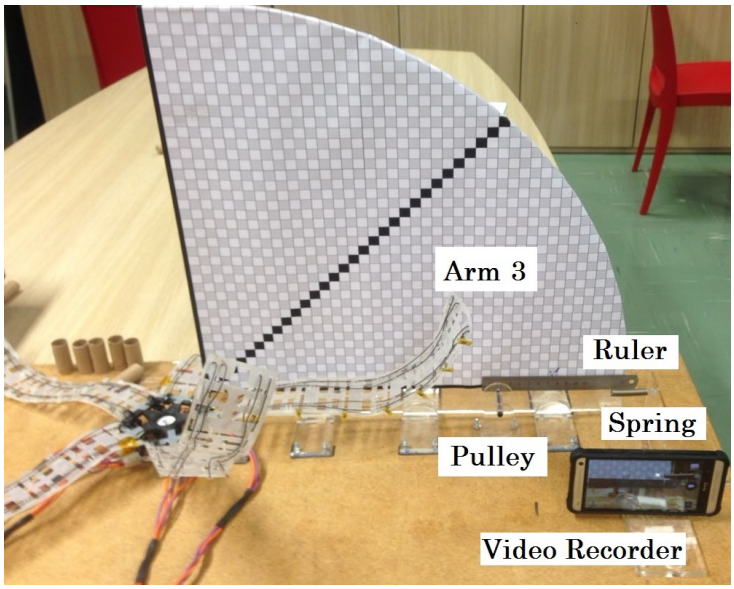

Figure 6.10 The physical test rig set-up for measuring the force generated by the programmed nitinol wires in the capture arms.

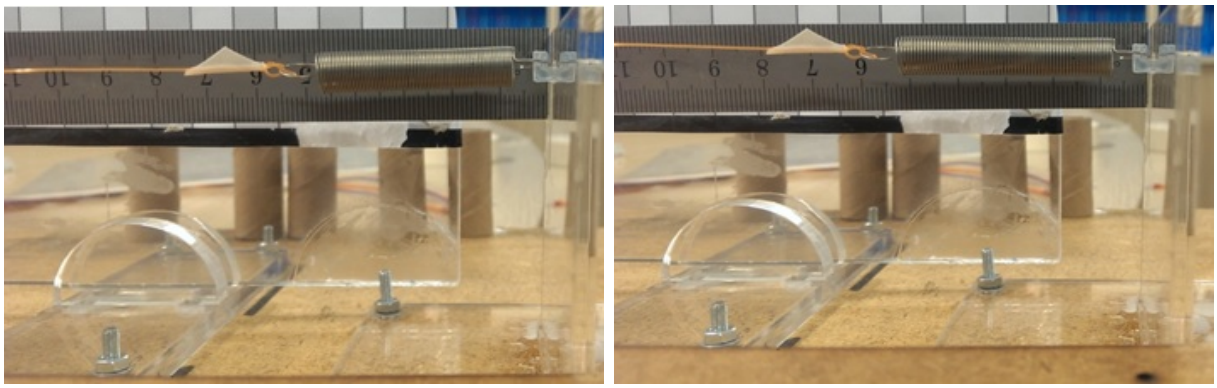

Figure 6.11 The extension of spring k_s in a strength test. The image on the left shows the spring length before power is supplied, the image on the right shows same spring with extension after power is supplied.

The free standing length of spring k_s was 33 mm and it was stretched to 37 mm after being placed on the test rig. That resulted in the spring holding a force of 0.104 N before voltage was applied, which means the C-circuit had to provide a restoring force larger than 0.104 N to have any further extension of k_s.

The forces induced by the C-circuit ranged between 0.156 N to 0.221 N for a range of supplied current from 2.37 A to 6.62 A. Considering the capturing arm has a mass of 26 grams the force it generated was approximately 86% of its own weight in 1 g.

The operational current selected in Section 6.1 to control MEDUSA was 5.61 A, which generates a maximum enclosing force of 0.221 N in the arm within 20 seconds. The forces generated while the capturing shape is restoring at different levels of input current are

Table 6.4 *Determination of force generated by the C-circuit for a range of input voltages and currents. The value in Extension (5th column) was measured on further extension on top of the 37 mm extension caused by physical placement of the spring in the test rig. Referring to the spring profile in Figure 6.9, the reader would have to add 4 mm to get the actual K_s value.*

Input Voltage (V)	Current (A)	Time (s)	Final spring length (mm)	Extension (mm)	Force (N)
1	0.60	60	37	0	-
2	1.12	60	37	0	-
3	1.68	60	37	0	-
4	2.37	60	39	2	0.156
5	2.89	44	40	3	0.182
6	3.56	44	41	4	0.208
7	4.40	33	41.5	4.5	0.221
8	4.90	23	41.5	4.5	0.221
9	5.50	20	41.5	4.5	0.221
10	6.62	11	41.5	4.5	0.221

shown in Figure 6.12. Once the maximum force is reached the induced force saturates regardless of the input current.

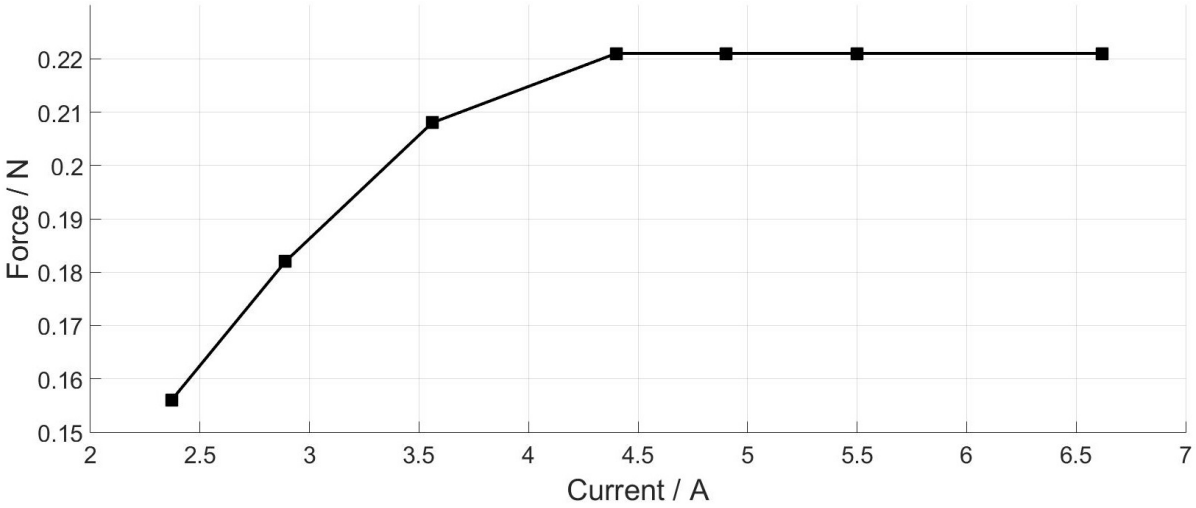

Figure 6.12 Force induced by the C-circuit at a range of input currents.

The amount of time taken to reach maximum force is inversely proportional to the input current, as higher current supplied to the C-circuit decreases the time taken to reach the maximum force, as shown in Figure 6.13.

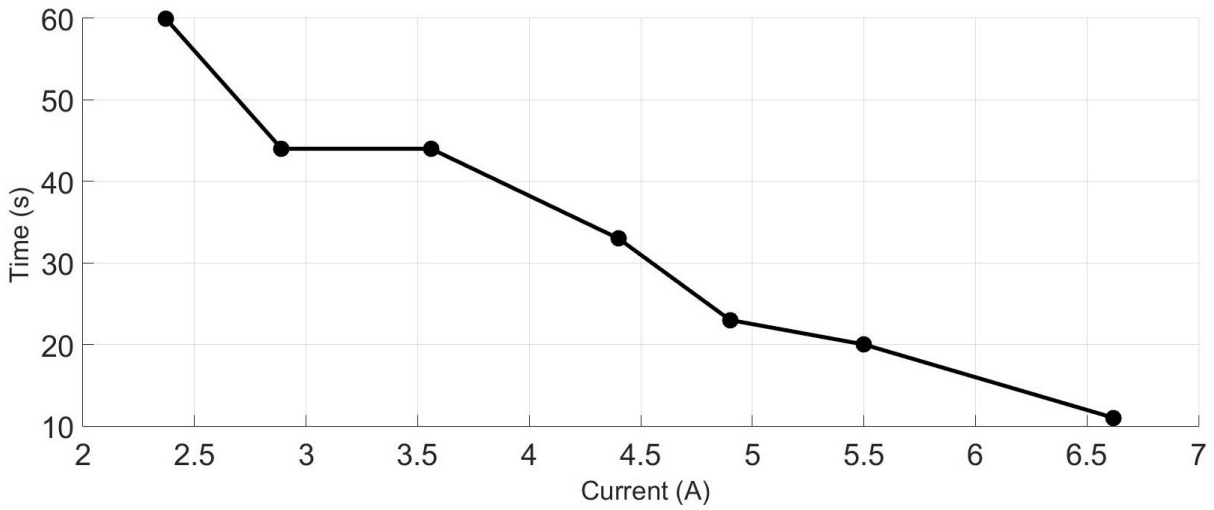

Figure 6.13 Time taken to induce full force for a range of input currents.

6.4 Vacuum chamber set-up for conducting tests in section 6.5 to section 6.10.

In order to investigate the operations of MEDUSA under vacuum conditions, a series of tests were performed in the vacuum chamber PWK1 [32] at the Institut für Raumfahrtsysteme (IRS) at Stuttgart University in Germany. (Figure 6.14)

To support MEDUSA inside the vacuum chamber during the test, a support structure was built using a set of Bosch modular strut profiles with MEDUSA bolted onto it firmly as shown in Figure 6.15.

The first step was to close the PWK1 vacuum chamber door via the built-in mechanical control panel. Once PWK 1 was completely sealed, we started pumping down PWK1 and turned on data logging. When the tank air pressure dropped below 20 hPa, we switched on the camera and we were ready for vacuum tests. The types of data obtained during these tests are listed in Table 6.5.

The atmospheric test set-up was identical to the vacuum tests, except PWK1 was not evacuated after it was sealed; instead we began data logging and started the test while tank pressure was at approximately 1000 hPa.

Before each test began we had to ensure that the residual air pressure was at the desired level. The air pressure of PWK 1 during the vacuum tests was maintained at less than 20 hPa.

Figure 6.14 Vacuum Chamber PWK1 at the Institute for Space Systems (IRS), in Stuttgart University.

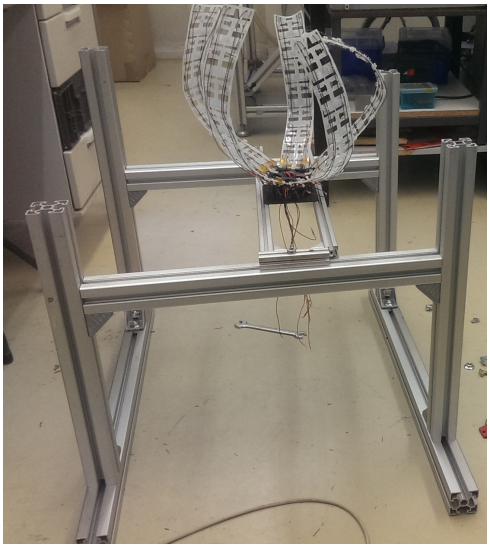

Figure 6.15 Supporting frame constructed from Bosch strut profiles. The frame was used to adjust the height of MEDUSA to be visible through the observation windows of PWK1.

Table 6.5 *Data obtained from vacuum chamber PWK1.*

Readings	**Units**
Voltage Drop Across MEDUSA	V
Current Passed Through MEDUSA	A
Tank Pressure	hPa
Temperature of Capture Nitinol	°C
Temperature of Release Nitinol	°C
Time	s

Figure 6.16 shows a schematic view of the test set-up. Fig 6.17 shows the schematic of the voltage divider and shunt resistor elements in greater detail.

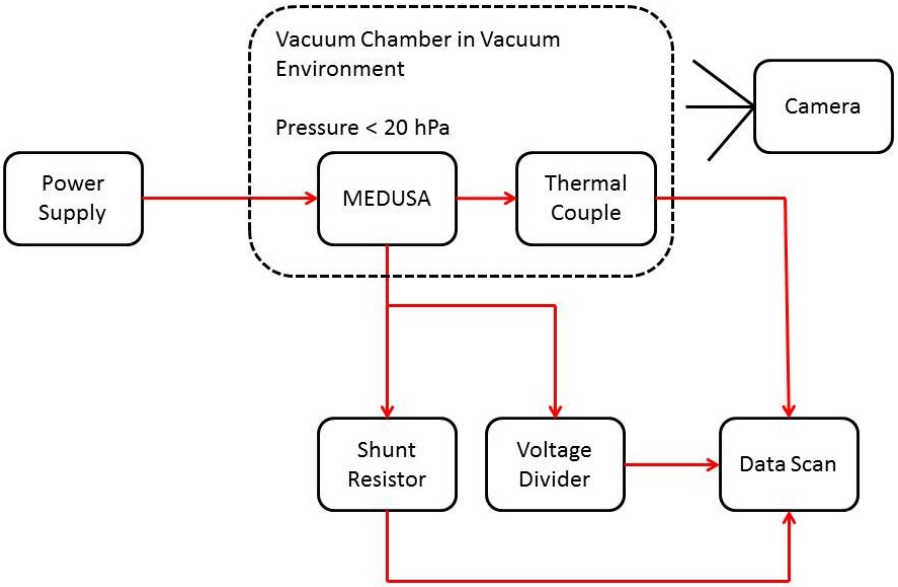

Figure 6.16 Schematic of instrumentation for data logging of the operation of MEDUSA Arm 2 in vacuum tests and atmospheric tests. Components shown in this schematic include: Voltage divider at a ratio of 1/3; Shunt resistor for current measurement; Thermocouple K1 and K2; Data scan built-in PWK 1 (timer included); Camera.

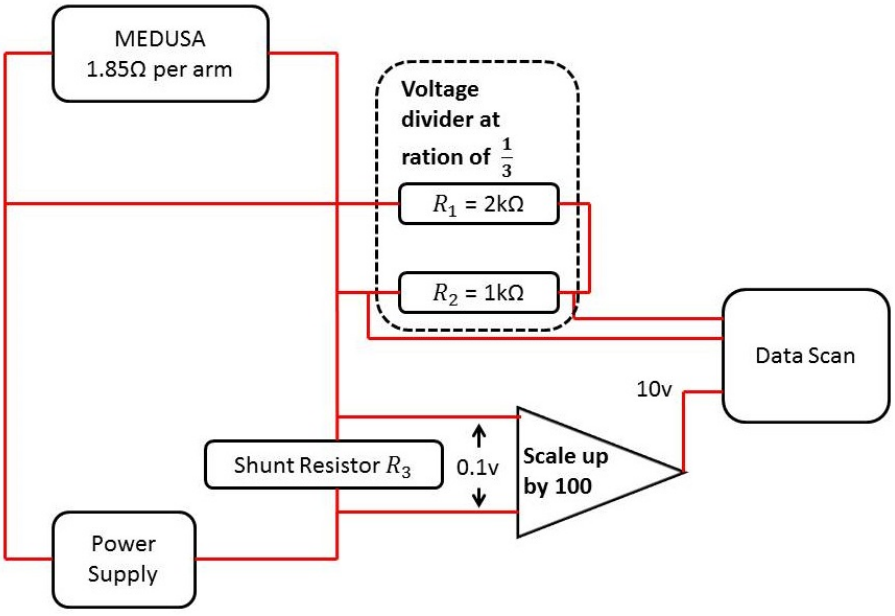

Figure 6.17 Detailed schematic of electrical instrumentation.

The experiment was designed to investigate the thermal behaviour of MEDUSA before, during and after capture and release operations in vacuum and atmospheric conditions. The temperature of MEDUSA Arm 2 was recorded at 0.1 second intervals while the nitinol

was were being actuated and therefore heating up, and also in the cooling down phase after actuation. A baseline reference temperature of 25°C was chosen as the starting/ending temperature for actuation (heating) or cooling phases, respectively.

Thermocouples K1 and K2 were installed on the nitinol wires of the C-circuit and R-circuit, respectively, to measure temperature changes in the nitinol wires.

To ensure uniform thermal conditions for the various tests, the test was started when the thermocouple K1 attached to the C-circuit read 25°C. If the nitinol wires were below 25 °C an impulse of current was supplied to heat up the nitinol wire to approximately 30°C, and then we waited until the temperature dropped to 25°C to start the experiment.

The test procedure was as follows:

Step 1: Supply 10 V with a corresponding current of 5A to the C-circuit in Arm 2 until the thermocouple K1 reads 50°C.

Step 2: Switch off input voltage.

Step 3: Wait for K1 to drop to 25°C.

Step 4: Supply 10 V and 5 A to the R-circuit in capturing arm.

Step 5: Switch off input voltage and current when thermocouple K2 attached to the R-circuit shows 50°C.

Step 6: Wait for K2 to drop to 25°C.

This cycle was repeated three times to average out random measurement errors. Readings from thermocouples K1 and K2 may be subjected to a lag based on the hardware limitation of the thermocouples. Also, volume differences between K1 and K2 could absorb heat from the nitinol via conduction as additional volume resulted from the patch surface joining K1 and K2 to Arm 2 acting as a heat sink. This could affect the temperature readings from K1 and K2.

6.5 Arm motion test and analysis

In this section we describe the motions of the capture arm during capturing and release actions conducted in both vacuum and atmosphere. A MATLAB script named "Particle Tracker 2.0" [33] was co-developed with Michael Dropmann from IRS. Particle Tracker 2.0 was developed for image processing and detailed analysis of the motion of the arms of MEDUSA.

A series of tests were carried out to observe the capturing motion and release motion in vacuum and atmosphere. The aim of these tests was to obtain measurements of the arm's trajectory as well as its velocity, percentages of shape recovery per second and total accumulated shape recovery. Data from capture and release actions carried out in both vacuum and atmosphere were compared to learn the differences when conducting these arm motions in the two different environments.

We first demonstrate the software architecture of Particle Tracker 2.0 in Section 6.5.1. Then we discuss the motion analysis of three capturing test conducted in vacuum in Section 6.5.2. We then discuss the motion analysis of a capture test conducted in atmosphere in Section 6.5.3. In Section 6.5.4 we discuss the comparison of capture motion data in the two different environments. The motion analysis of the release action conducted in vacuum is discussed in Section 6.5.5 and a similar release action conducted in atmosphere discussed in Section 6.5.6. Finally, in Section 6.5.7 we compare the release actions conducted in the two environments.

In all the tests listed above, the capture arm (Arm 2) did not manage to fully restore the programmed shape; instead it only restored up to roughly 65% to 75% of the programmed shape. The deficiencies were due to hysteresis effects that resulted from a large amount of undocumented preliminary testing that was conducted to learn the behaviour of MEDUSA in vacuum before any testing procedures were established. The MEDUSA system underwent approximately 40 to 45 tests in vacuum and thereafter a series of effective testing procedures was established to test the MEDUSA system in vacuum as shown in Section 6.4. The testing procedure established and shown in Section 6.4 should be used for testing the next generation of MEDUSA. Unfortunately, the large number of early tests degraded the performance of both capture and release nitinols in Arm 2. Also during these tests the arm mounting plate used to anchor the capture arm to the base was damaged from over-heating.

Despite the hysteresis effect in the nitinols and the damaged arm mounting plate, the data documenting the pattern of shape recovery was still valuable and worth a thorough study. Also the motion data provided insights into state transitions while the capture arm are executing capture and release actions in vacuum and atmospheric environments. Lastly, observations documented in different stages during tests also provided recommendations for upgrading the next generation of MEDUSA.

6.5.1 Software architecture of Particle Tracker

In this section we describe the software architecture of the particle tracker algorithm, which was used to extract motion data from the capture arm.

The physical test set-up was identical to the vacuum tests described in Section 6.4. Additionally, capture arm motions were filmed using a standard camera. Eight yellow markers were attached at equal intervals along Arm 2 as shown in Figure 6.18 to define fixed points on the arms for processing motion data in Particle Tracker 2.0. The markers help to isolate Arm 2 from the background to have less random noise in the data extractions.

Pixels of yellow markers were extracted from the first frame of each video containing either capture or release actions, as shown in Figure 6.19.

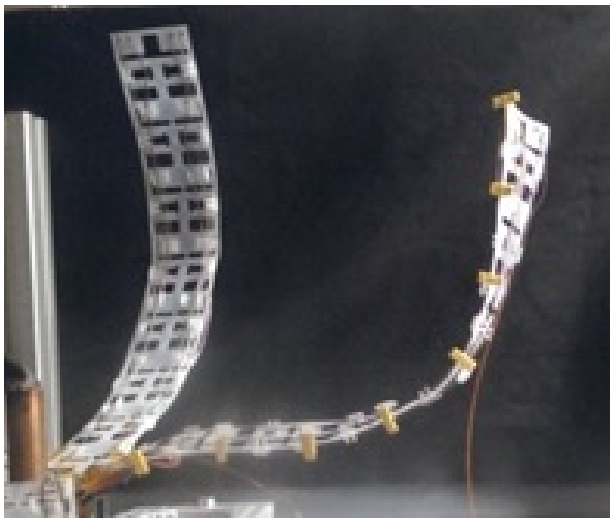

Figure 6.18 MEDUSA Arm 2 in the vacuum chamber with markers to trace the motion of the arm. A black cloth was placed behind MEDUSA to reduce the amount of background light and to strengthen color contrast in order to eliminate random noise in color filtering when the marker positions were extracted from the images.

Figure 6.19 Since the marker tags were not exactly perpendicular to the line of sight of the camera, and since they also experienced an illumination gradient, we sampled a small number of pixels from the top and bottom edges of each marker. These sample regions were crapped using the image processing tool ImageJ then pasted into a new image with black background in Paint to simplify the filtering process in a subsequent stage of Particle Tracker algorithm.

The RGB values of pixels of the yellow markers were extracted from Figure 6.19 to form a three-dimensional colour-filter matrix in pixel space, shown in Figure 6.20, that would be used to locate all the marker pixels in subsequent image frames. Variations in RGB values in pixels can be quite significant if illumination is not consistent. To counter this issue a best-fit curve was calculated to obtain an averaged value that minimized distortions from illumination. A three-dimensional color filter was made separately for each capture and release motion sequence.

All image frames representing capture and release actions were filtered to extract the locations of markers with a uniquely defined colour-filter matrix. The extracted locations were then passed to the next stage of Particle Tracker to produce two sets of imagery products. The first imagery product, shown in Figure 6.21, was produced by extracting the locations of the eight markers and plotting their pixel values at a rate of one frame per

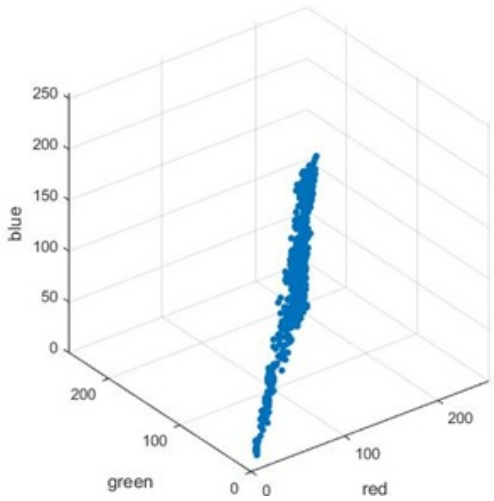

Figure 6.20 Colour-filter matrix: RGB value pixels were extracted from the yellow markers shown in Figure 6.19. These pixels form a colour filter matrix to locate all marker pixels in subsequent image frames.

second. Thus it shows the movement of the capture arm in each second and the number of frames depends on the time taken to complete one capture/release action.

To produce the second imagery product, Particle Tracker takes the pixels containing marker positions from the first imagery product and identifies a centroid in a cloud of pixel values which it then used as the representative point of each marker. In order to convert pixel values into linear dimensions (millimetres) a conversion ratio was needed. We obtained the conversion ratio by photographing a calibrator card with a rectangular 5 mm grid, which was placed inside the vacuum tank at the same distance and in the same plane as the motion of Arm 2. We then calculated the length between two end points on the sides of a square in pixels then compared it to the physical length of the same square printed on the background calibrator card. The Particle Tracker then applied the conversion ratio to the centroids to derive their physical co-ordinates.

The second imagery product contains derived physical co-ordinates of each marker and plots them in one image that shows the changing profile of the arm on a second-by-second basis in Figure 6.23. The software architecture of Particle Tracker is shown in Figure 6.22.

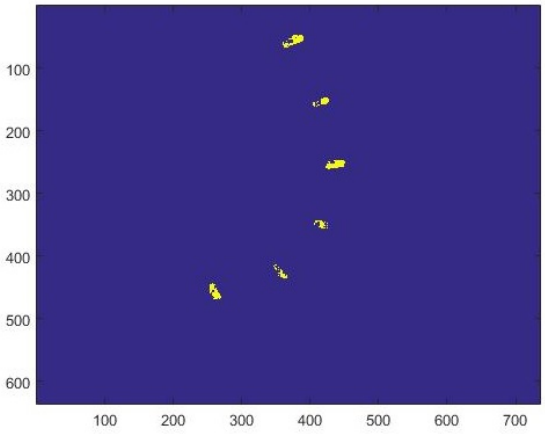

Figure 6.21 The first imagery product of Particle Tracker 2.0 shows movement per second measured in pixel values. Each video will result in a different number of images depending on the time taken to complete the capture/release motion. This image was sourced from the 6th second of the first capturing test in vacuum.

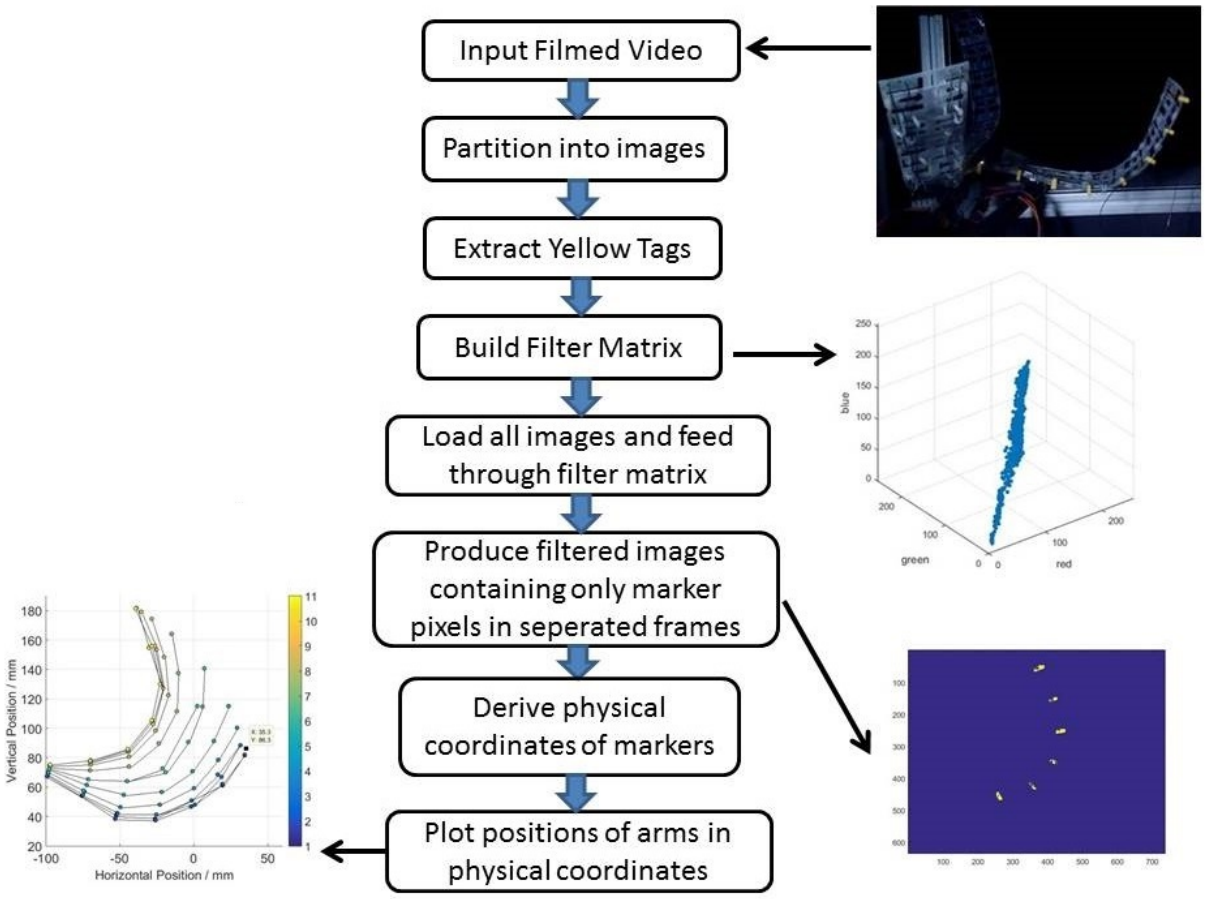

Figure 6.22 Sequence of operations carried out on image data by Particle Tracker 2.0, with corresponding end-products at each stage.

6.5.2 Capturing motion in vacuum

Figures 6.23, 6.24 and 6.25 below depict the capture motions recorded in the first three vacuum tests.

On average, Arm 2 took approximately 16 seconds to complete a capture action in vacuum. A capture action was deemed completed when the tip of the arm reached the vertical line marked as -50 mm on the x-axis. The time taken to complete the capture action was slightly longer than the 10 second requirement stated in System Requirement 2.

The second capturing motion, shown in Figure 6.24, was conducted for 11 seconds without fully reaching the -50 mm vertical line. Comparing Figure 6.23 to Figure 6.24, Arm 2 took an additional 5 seconds to complete the remaining 20% of the capture motion, which moved the arm 5 mm closer to the -50 mm vertical line on the x-axis.

The Figures show how the shape restoration progresses during the state transition from the Martensite state M_f to the start of the Austenite state A_s. The largest movement occured from the 2nd second to the 8th second, then the movement slowed down as nitinol state transformed from A_s toward the end of the Austenite state A_f.[3]

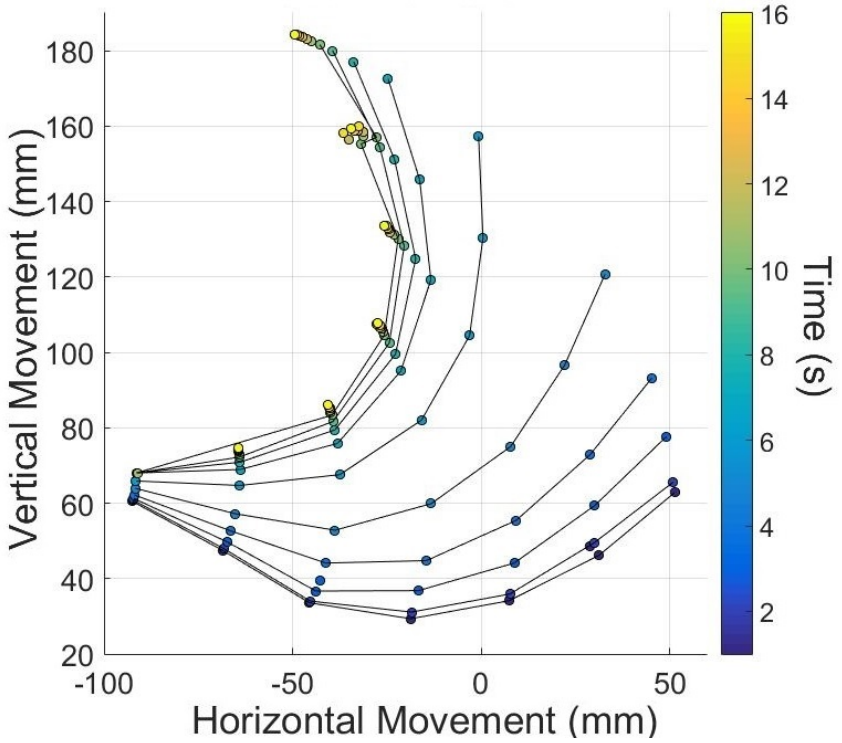

Figure 6.23 First capture motion in vacuum. The first yellow marker was buried in noise thus we only show markers from 2 to 8.

[3]We recognize during these capture tests non of the arms closed to the point that a 1-U target would have been captured, but this is because the nitinol in the capture arm was starting to become fatigued from repeated opening and closing motions that we carried out while we are practising and developing the test proceduers to collect the data presented in this section.

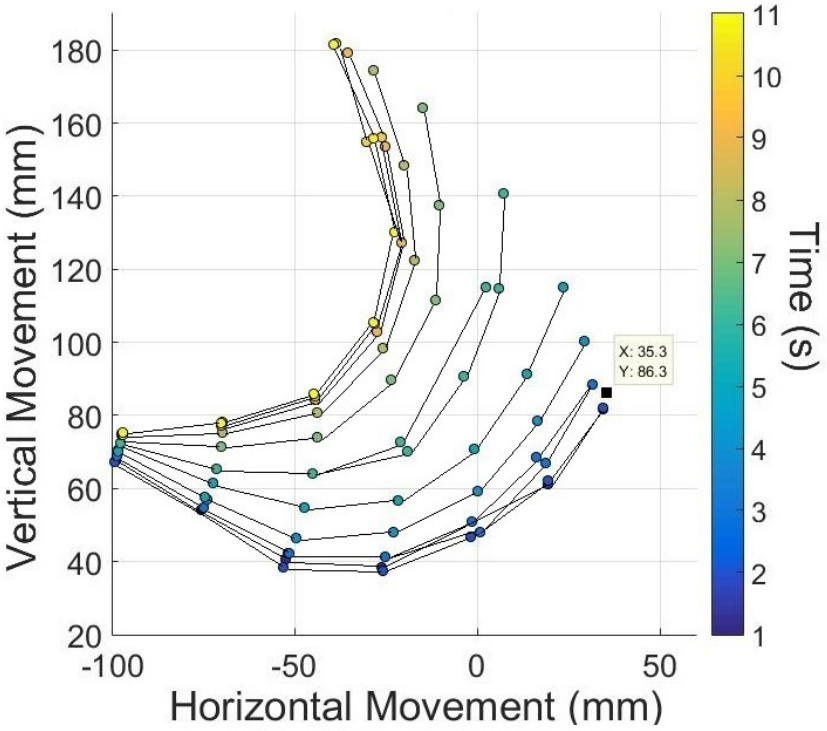

Figure 6.24 Second capture motion in vacuum. The first yellow marker was buried in noise thus we only show markers from 2 to 8.

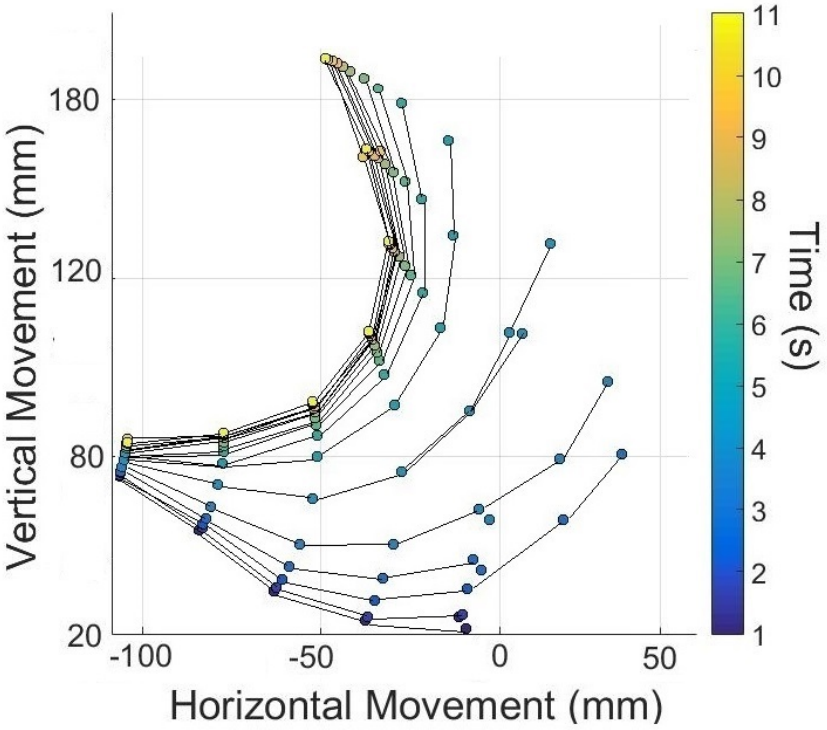

Figure 6.25 Third capture motion in vacuum. The first yellow marker was buried in noise thus we only show markers from 2 to 8.

The average time taken in these tests is 6 seconds longer than single arm test described in Chapter 6.1 and the simulated target capture test in atmosphere shown in Chapter 6.2. This is due to additional resistance added onto the MEDUSA system from the longer cables that were used to connect MEDUSA to the external power supply when it was placed inside the vacuum chamber. In its proper configuration MEDUSA will be connected directly to the chaser spacecraft's power supply where the cable length would be less than 10 centimetres so additional resistance from cables will not occur.

Figures 6.26, 6.27 and 6.28 depict the capturing trajectories of the 8th yellow marker on Arm 2 during the capture motions.

We used the 8th yellow marker placed near the tip of the arm instead of the others because it covered the largest displacement during the capture motions. The largest displacement occurred during the state transition from the Martensite state M_f to the Austenite state A_s, starting from the 4th second until the 8th second. Once state transition had moved towards the end of A_f, the capture motion slowed down and at the end of Austenite state A_f no further movement occurred.

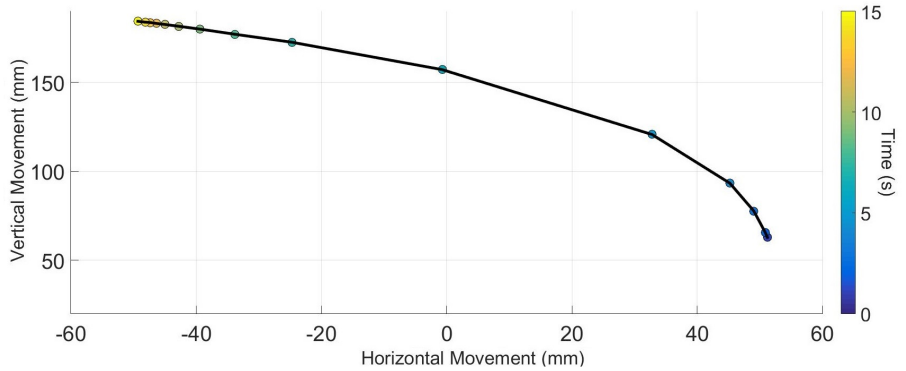

Figure 6.26 Trajectory of the 8th marker during the first capture motion.

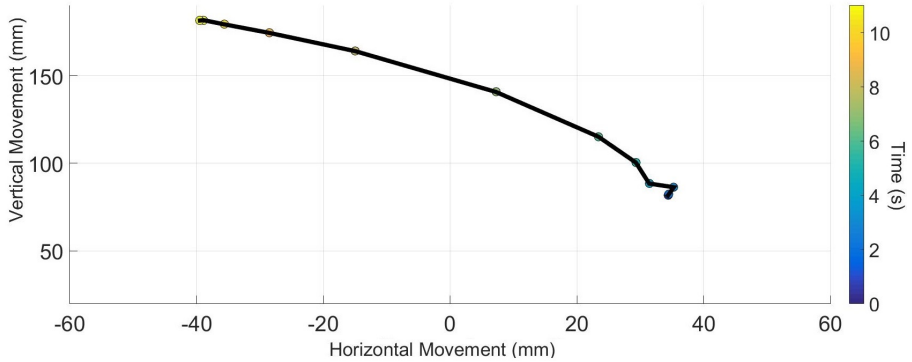

Figure 6.27 Trajectory of the 8th marker during the second capture motion.

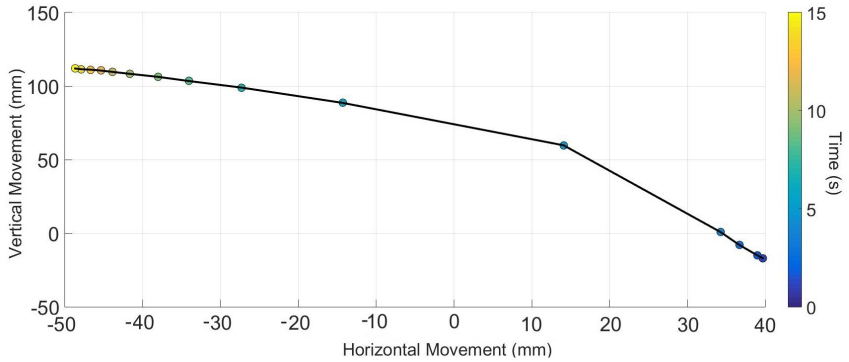

Figure 6.28 Trajectory of the 8th marker during the third capture motion.

Figures 6.29, 6.30 and 6.31 show the velocity of the 8th yellow marker during the three capture motions. The velocity values were obtained from the first derivative of the yellow-marker trajectories over time shown in Figure 6.26, 6.27 and 6.28. In Figures 6.29 and 6.31, the velocity increased slowly from zero to a peak velocity of 78 $\frac{cm}{s}$ at the 4th second and stayed at that value for 2 seconds before slowing down. The peak velocity corresponds to the period, when the state transition occurred from M_f to A_s and slowed down while the nitinol transformed from A_s towards A_f.

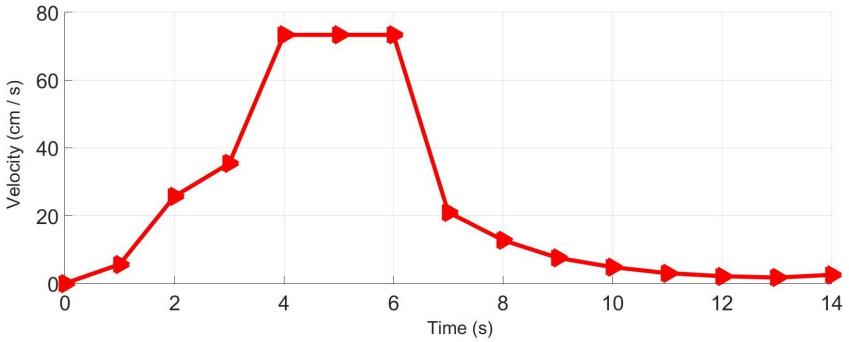

Figure 6.29 Velocity of the 8th yellow marker during the first vacuum capture motion.

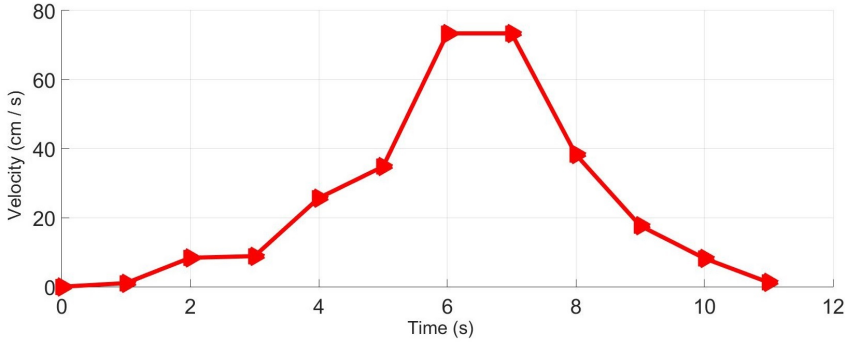

Figure 6.30 Velocity of the 8th yellow marker during the second vacuum capture motion.

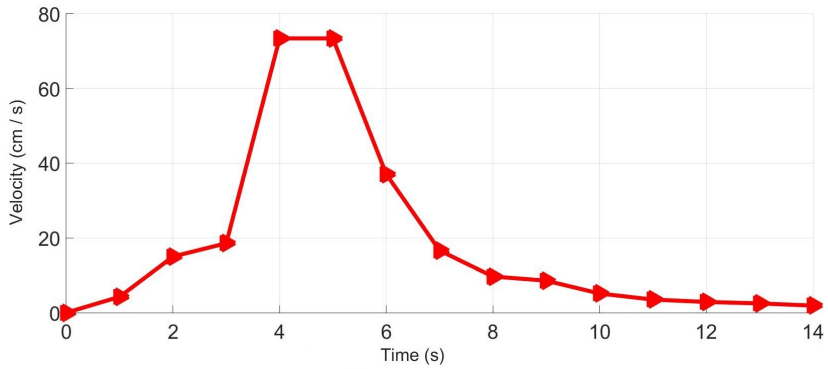

Figure 6.31 Velocity of the 8th yellow marker during the third vacuum capture motion.

The percentage of shape restored per second during the first, second and third capture tests in vacuum is shown in Figures 6.32, 6.33 and 6.34. To measure the percentage of shape restoration per second we calculated the length of the entire trajectory shown in Figures 6.26, 6.27 and 6.28. We then took the distance travelled by Arm 2 at each second divided by the total length of the trajectory to work out the percentage of shape restored per second. Although Arm 2 did not fully enclose the portion of the capturing volume it is responsible for, the pattern of shape restoration is the same irrespective of the presence of the hysteresis effect. Hence the shape restoration study shown in this section is still valuable in terms of helping us to understand the shape restoration behaviour of nitinol.

In Figure 6.32 an increasing trend in shape restoration is evident from the 1st second until the 5th second, when the peak 31% of shape restoration was reached. From the 6th second onwards the percentage of shape restoration per second started to decrease. From the 8th second until the 14th second Arm 2 performed a gradual dilatory shape restoration to complete the remaining 20% of shape restoration.

In Figure 6.33, the capturing test was stopped before Arm 2 reached the -50mm vertical line on the x-axis, which is why the dilatory shape restoration did not reflect on the graph. Such slow shape restoration typically happened during the state transition from Austenite start A_s to the end of the Austenite finish A_f phase. The peak of 25% shape restoration occurred at the 7th second, the latest in all three vacuum capture tests.

In Figure 6.34 a similar shape recovery pattern was observed, although a higher peak of 39% shape restoration occurred at the 4th second, which is one second earlier than in the first vacuum capture test in Figure 6.32.

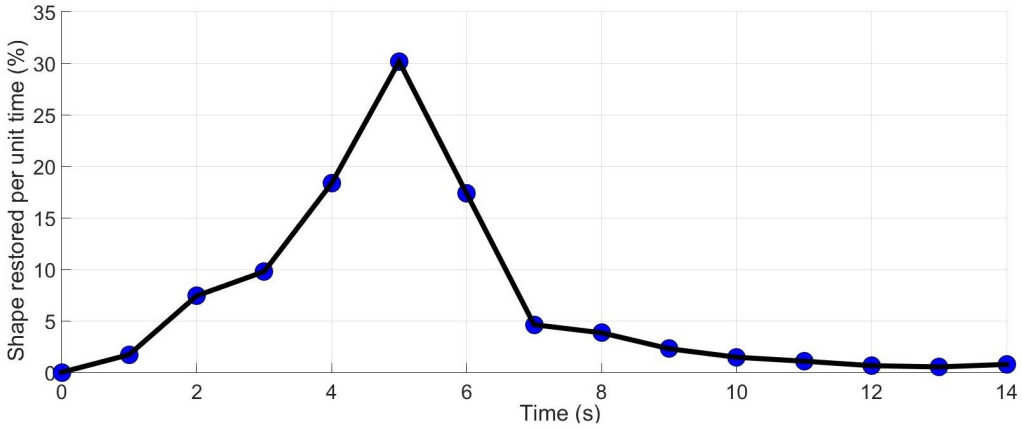

Figure 6.32 Percentage of shape restoration per second during the first vacuum capture test.

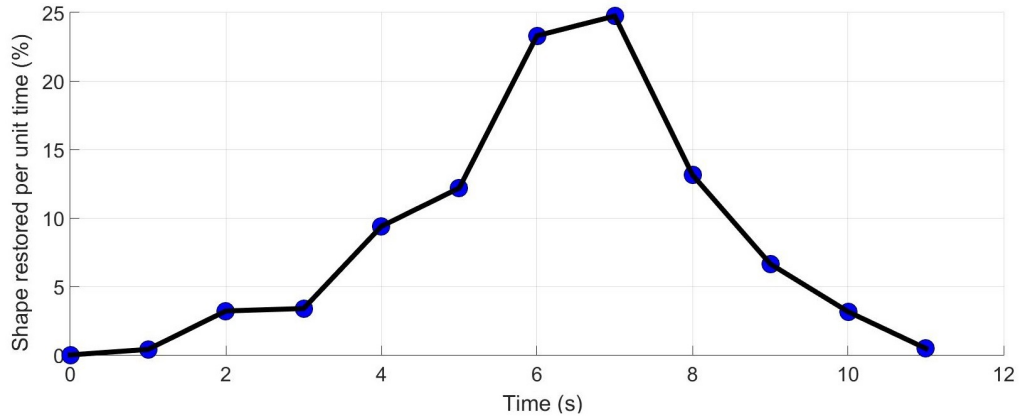

Figure 6.33 Percentage of shape restoration per second during the second vacuum capture test.

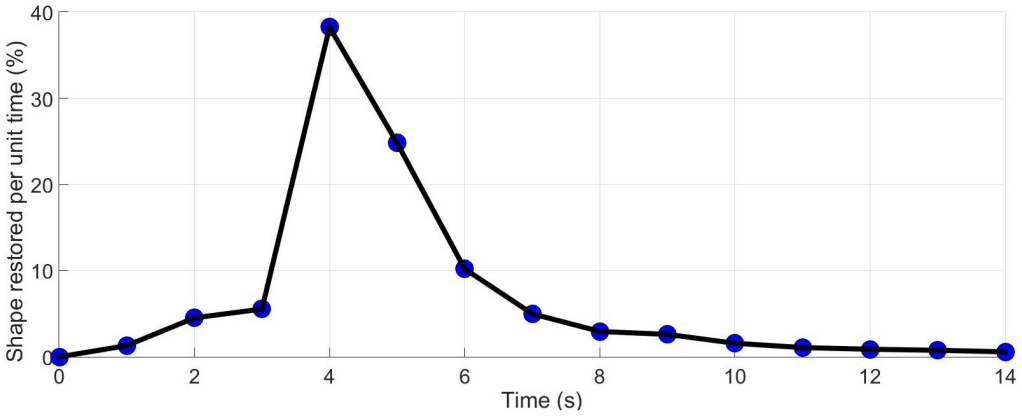

Figure 6.34 Percentage of shape restoration per second during the third vacuum capture test.

To get an overview of the pattern in which shape restoration occurs we present the accumulated shape restoration over time depicted in Figures 6.35, 6.36, and 6.37.

Figure 6.35 shows that more than 80% of shape restoration was completed within the first 6 seconds and it took a longer period of 8 seconds to complete the remaining 20% of shape restoration. The rapidly increasing parts of the shape restoration curve, from the 3rd to 6th second, occurred during the time when the nitinol was transforming from Martensite M_f to Austenite A_s. The 5th second in Figure 6.35 marks the point of inflection when the rate of shape recovery stopped increasing; at the 6th second the rate of shape recovery started to slow down. That is the point where the nitinol state was fully transformed from Martensite M_f to Austenite A_s. From the 7th second onwards the speed of shape restoration slowed down while the nitinol transitioned from Austenite start A_s to Austenite finish A_f.

Similar behaviour was observed in the second test (Figure 6.36) and third test (Figure 6.37). In Figure 6.36, 80% of shape restoration was also achieved within the first 6 seconds and the remainder took 8 seconds. In Figure 6.37, 80% of shape restoration was achieved within the first 7 seconds and the remainder took 5 seconds.

This behaviour of shape restoration in vacuum can be incorporated into future design enhancements of MEDUSA to reduce the total input current requirement and also to reduce the time required to complete a capture action in vacuum. The capture motion should be programmed within the 80% region where rapid shape recovery occurs to halve the time needed for shape recovery. A faster shape recovery leads to a faster capture motion, which decreases energy consumption. The electrical energy used to actuate MEDUSA over the required time is given by by the equation $E = I^2Rt$. During a capture or release action the input current stays constant and a slight change in resistance is expected due to the resistivity difference in the two states of nitinol. Cutting down one second of actuation time would save 181.74 J in consumed energy and that would alleviate pressure on the power supply system and enhance the chance of success in an actual debris capturing mission.

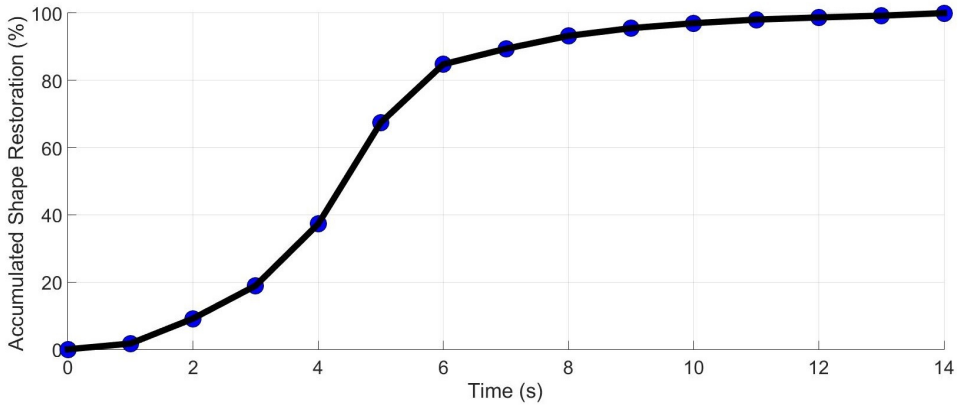

Figure 6.35 Percentage of shape restoration accumulated during the first vacuum capture test.

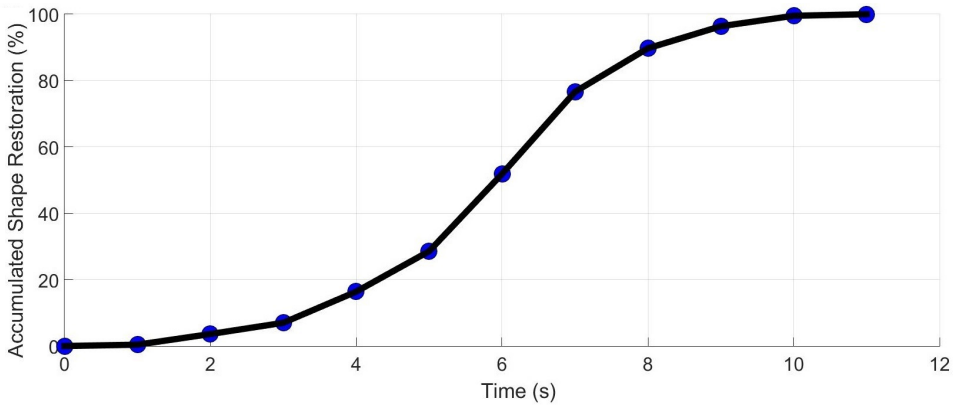

Figure 6.36 Percentage of shape restoration accumulated during the second vacuum capture test.

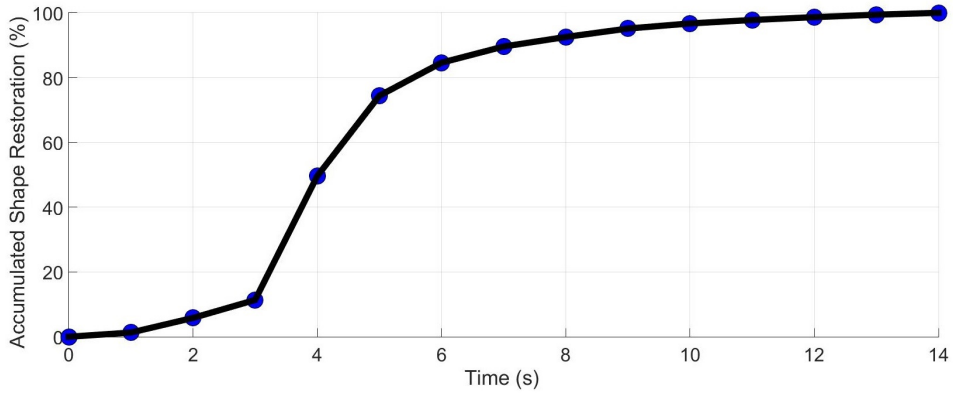

Figure 6.37 Percentage of shape restoration accumulated during the third vacuum capture test.

6.5.3 Capture motion in atmosphere

The capture action described in this section was conducted in the vacuum chamber PWK1 without evacuation, and is shown in Figure 6.38. The power supply was identical to that used for the vacuum tests shown in Section 6.5.2.

The capturing action took 22 seconds to complete in atmosphere, which is 6 seconds longer than a capturing action in vacuum. The capturing action in this test started at a different position compared to the capture tests in vacuum, and it ended when the tip of the arm reached the -60 mm vertical line on the x-axis, instead of the -50 mm line on the x-axis for the capture test conducted in vacuum.[4]

[4]A few human errors took place during the two experiments showed in Section 6.10.2 and Section 6.10.3 which caused the capture Arm 2 to start at two different positions. The offsets were approximately 70 mm in the vertical direction and 10 mm in the horizontal direction. Such error should be eliminated in the future experiments by match the 8th marker on capture Arm 2 to a fixed starting point engraved onto the backboard placed behind the capture arm.

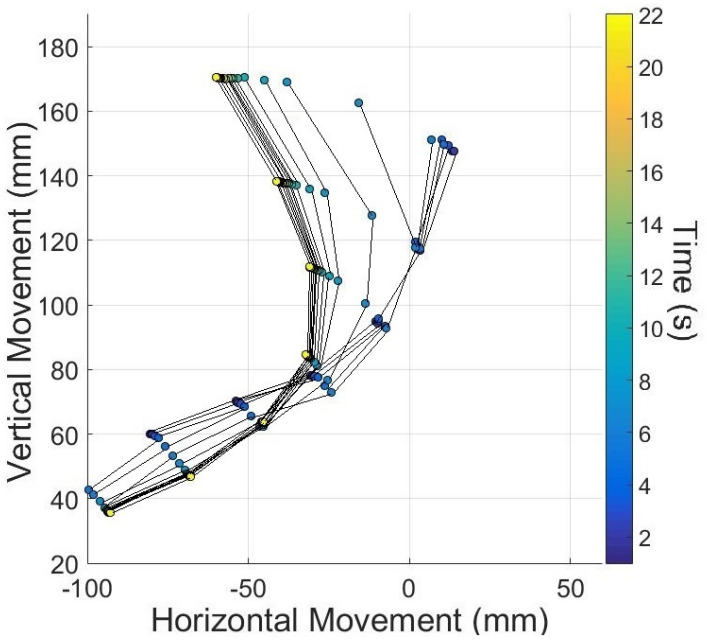

Figure 6.38 Capture motion conducted in atmospheric environment in PWK1.

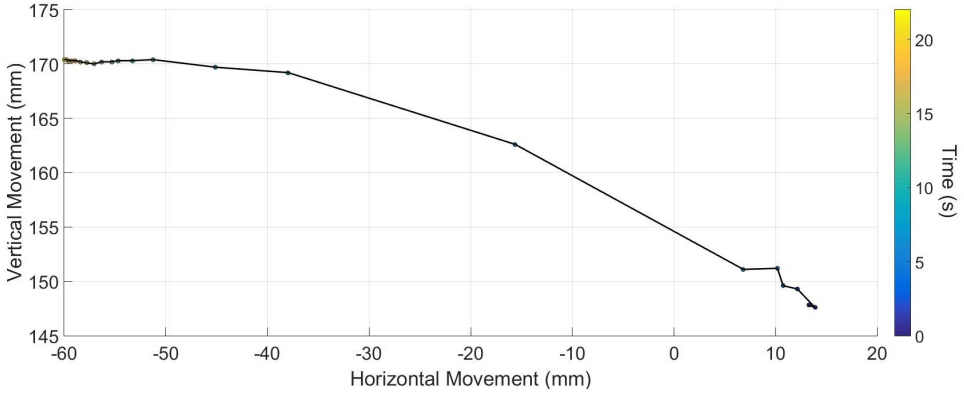

Figure 6.39 Trajectory of the 8th marker during the capture motion in atmosphere.

The peak velocity of 72 $\frac{cm}{s}$ was reached at the 6th second. It then dropped to 70 $\frac{cm}{s}$ one second later and then rapidly slowed down immediately after this. From the 10th second onwards the velocity of the capturing arm gradually declined towards zero as nitinol state transitioned from A_s to A_f. During this period the movements were insignificant.

The percentage of shape recovery achieved per unit time in atmosphere is depicted in Figure 6.41. The percentage of shape recovery shown in Fig 6.41 were calculated by dividing the trajectory covered in each second by the total trajectory length shown in Fig 6.39.

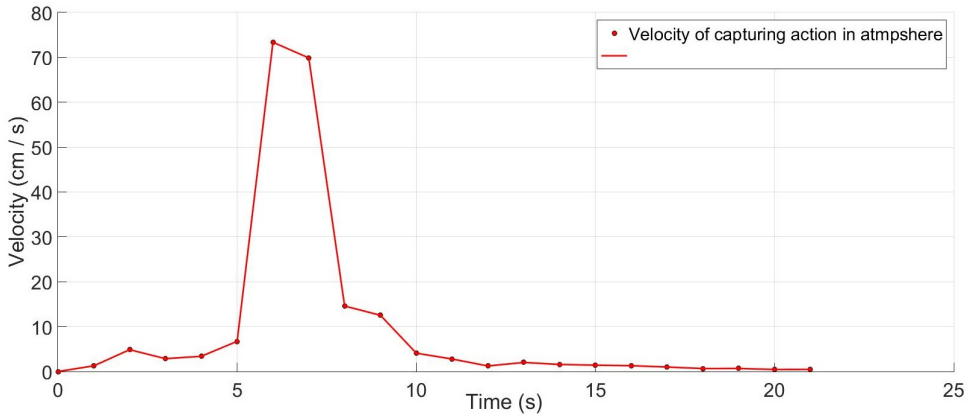

Figure 6.40 Velocity of the 8th yellow marker during the capture motion in atmosphere.

The total time taken to complete shape recovery in atmosphere was 21 seconds. The shape recovery increased slowly from zero and reached its peak value of 31 % at the 6th second. Thereafter the rate of shape recovery decreased from the 10th second onwards and stayed close to zero as the nitinol state transitioned from the Austenite state A_s to Austenite state A_f.

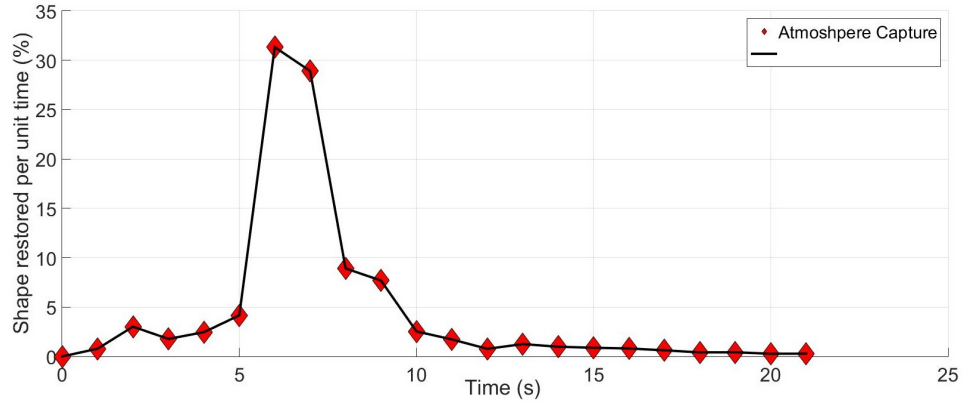

Figure 6.41 Calculated percentage of shape restored per unit time during the capture test in atmosphere.

The accumulated shape recovery shown in Figure 6.42 reveals that 80 % of the total capturing action was completed within the first 8 seconds, which took 2 seconds longer than the 80% fast shape recovery in a vacuum.

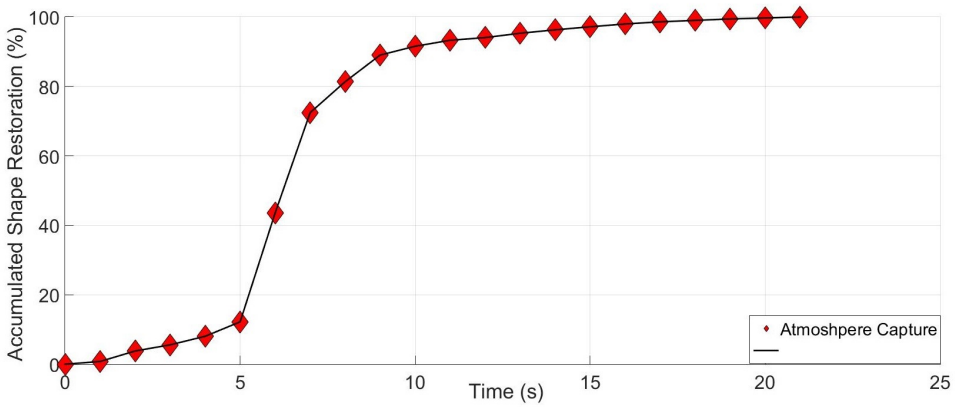

Figure 6.42 Percentage of shape restoration accumulated during the capture test in atmosphere.

6.5.4 Comparison of the capturing motion in vacuum and atmosphere

In this section we compare the capture motion data of the vacuum tests shown in Section 6.5.2 and atmospheric test shown in Section 6.5.3.

The input current supplied was identical for both tests in vacuum and atmosphere. Data logging started at 25 ^{0}C and finished at 50 ^{0}C. The first vacuum capture test shown in Figure 6.23 was compared to the capture test in atmosphere shown in Figure 6.38. The trajectories described by the arm in both tests are plotted in Figure 6.43.

In vacuum, the 8th marker on Arm 2 was positioned at (51;61) at the start of the test and ended at (-50;181) after 15 seconds. The same marker on the same arm in atmosphere started at (14;147) and ended at (-60;171) after 22 seconds.

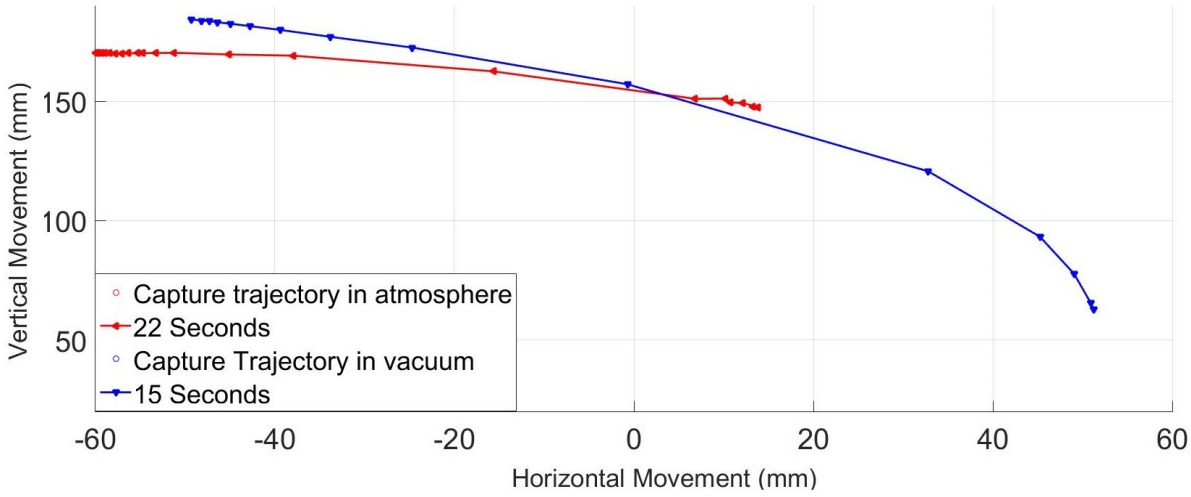

Figure 6.43 Comparison of the capture trajectory described by the tip of Arm 2 in vacuum and atmosphere.

A comparison of the velocity of capture motion in vacuum and atmosphere is shown in Figure 6.44. In vacuum a peak velocity of 72 $\frac{cm}{s}$ was reached within four seconds after the input current was supplied and the peak velocity was maintained for another 2 seconds from 4th to the 6th second. In atmosphere, it took 6 seconds to reach a peak velocity of 72 $\frac{cm}{s}$ and this was not sustained for any length of time.

The nitinol wires took longer to reach the activation temperature in atmosphere because heat exchange with ambient surroundings occurred through conduction with the arm support base and polyamide, through convection by air particles and through radiation, whereas in vacuum heat transport was limited to radiation into the ambient environment and conduction with the arm support base and polyamide body.

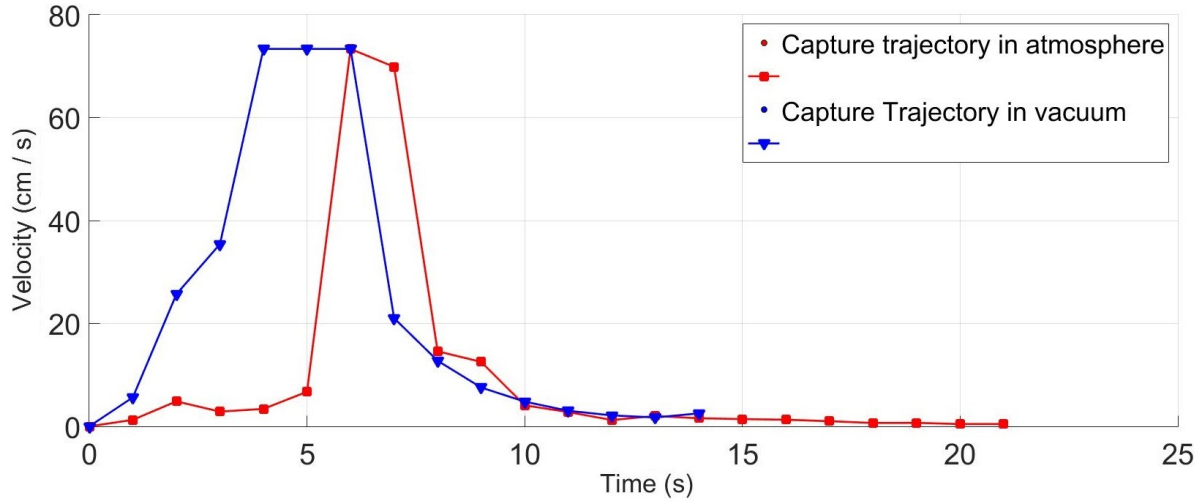

Figure 6.44 Comparison of velocity of the tip of the capture arm for capture operations in vacuum and atmosphere.

Overall, the capture motion in vacuum was much smoother and more repeatable than in atmosphere. Shape restoration completed within a shorter time leading to less input power consumed.

The shape recovery rates in vacuum and atmosphere are compared in Figure 6.45. The three capturing tests done in vacuum are marked in blue. The first and third "C" shape restorations in vacuum have very similar patterns. In both tests the "C" shape restored within 14 seconds, although the third vacuum capture had a higher peak of 39% shape recovery rate in the 4th second. The atmospheric capture motion took 8 seconds longer to complete a similar action compared to the average time taken in a vacuum environment.

The capture action in an atmospheric environment took 3 seconds longer to reach peak shape restoration (31%) compared to capture actions conducted in vacuum, meaning that the state transition took longer to occur due to greater heat losses in the atmospheric test.

The accumulated percentage of shape restoration for vacuum and atmosphere is plotted in Figure 6.46. The first and third capture actions in vacuum completed 80% of shape restoration 2 seconds faster than the a similar capture action carried out in an atmospheric environment.

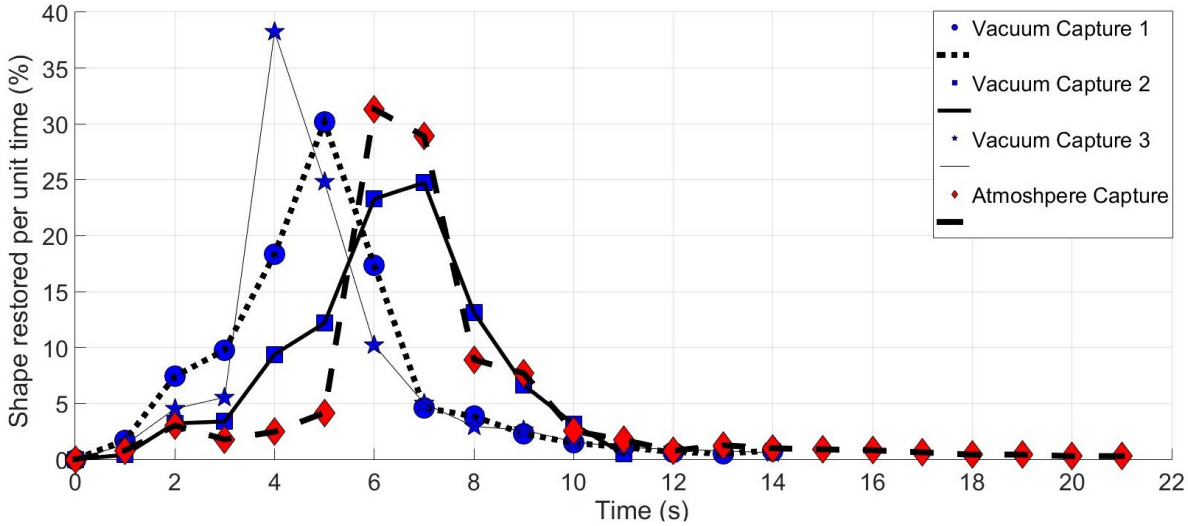

Figure 6.45 Percentage of shape recovery rate calculated and displayed in seconds for capture actions in vacuum and atmosphere.

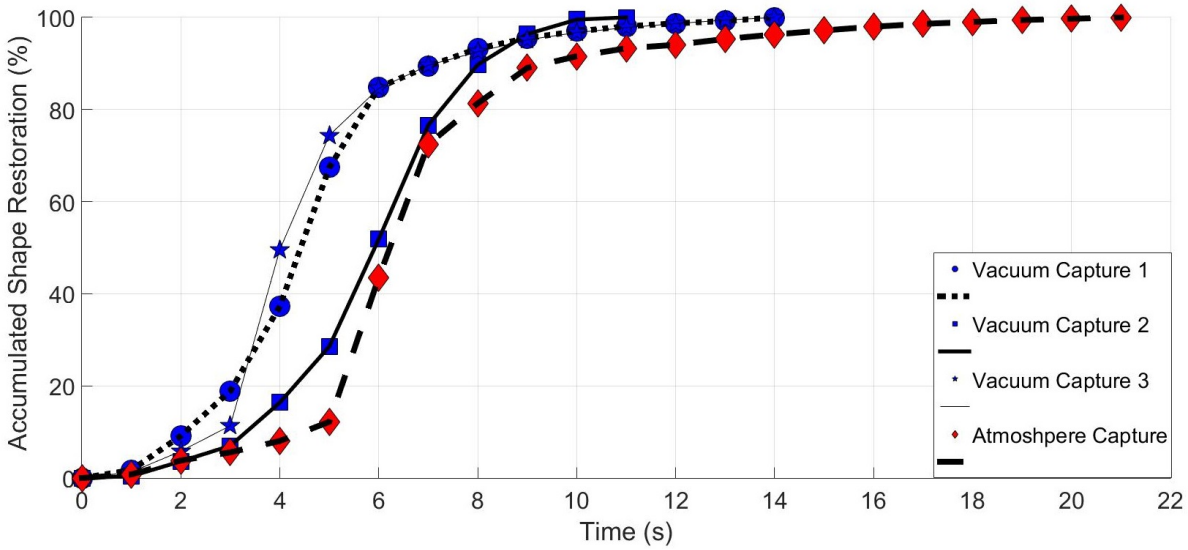

Figure 6.46 Accumulated percentage of shape restoration in vacuum and atmosphere.

6.5.5 Release motion in vacuum

Two release tests were conducted in vacuum, but only the first release motion data set was usable. The images acquired during the second test suffered from large discrepancies in the RGB values of the pixels, which made it difficult to extract data for the markers, especially during the first 8 seconds. The power input was identical to that of the capture motion tests.

Displacement during the release action was not as obvious as during the capture motions due to shorter trajectories achieved during the release motions. Arm 2 took 26 seconds to

complete the release action in vacuum, double the time needed to complete the capture action in vacuum.

The longer time required to complete the release action can be explained by the differences in curvature between the capture shape “C” and release shape “L” nitinol circuits, which fundamentally changed shape restoration time.

The motion of Arm 2 during the release action is depicted in Figure 6.47 and the velocity of the 8th yellow marker during the release action is depicted in Figure 6.49. The velocity of this marker increased slowly within the first three seconds, followed by a sharp increase during the 4th second.

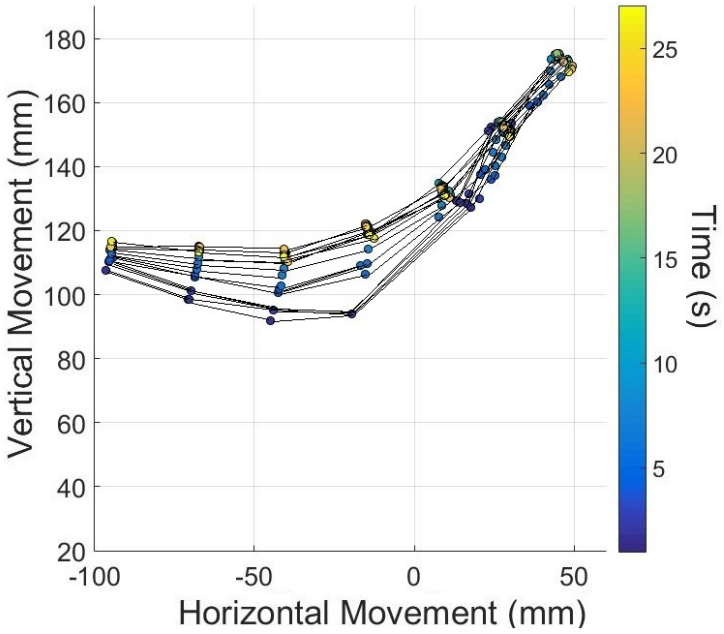

Figure 6.47 Release motion in vacuum. It was not possible to extract data for the first yellow marker due to noise; thus we only show data for markers 2 to 8.

In Figure 6.50 we see that the rate of shape restoration was not as fast as during the capture motions. Shape restoration increased from the 1st second to the 4th second and a peak value of 14% was reached at the 4th second. The accumulated shape restoration over time is plotted in Figure 6.51, which shows that 80% of shape restoration was achieved within the first 14 seconds.

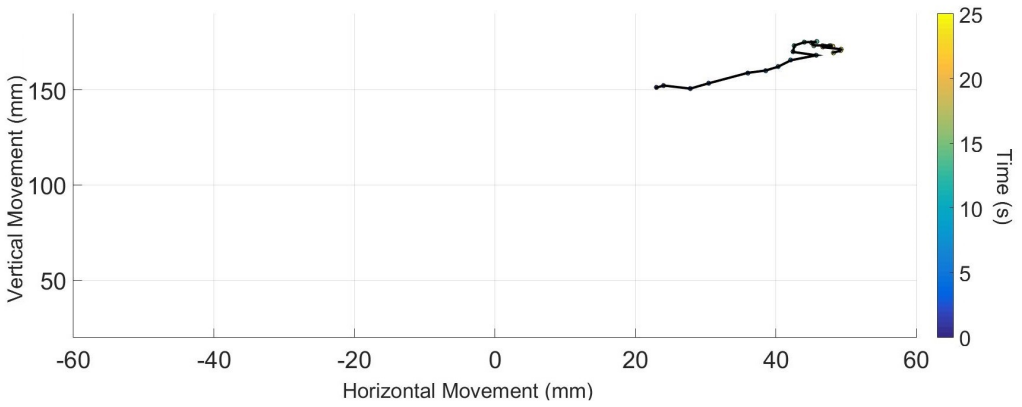

Figure 6.48 Trajectory of the 8th yellow marker during the release motion in vacuum. The marker displayed a linear trajectory in the first 14 seconds, followed by a curved motion from 15th second until the 25th second.

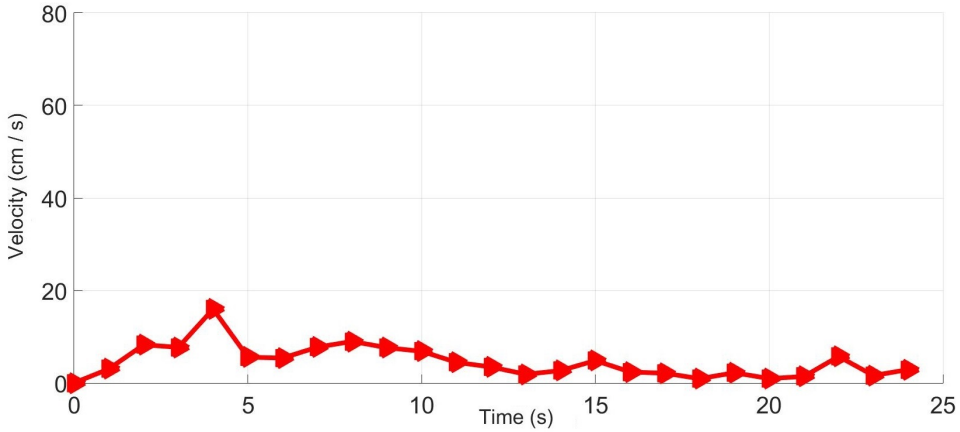

Figure 6.49 Velocity of the 8th marker during the release motion in vacuum.

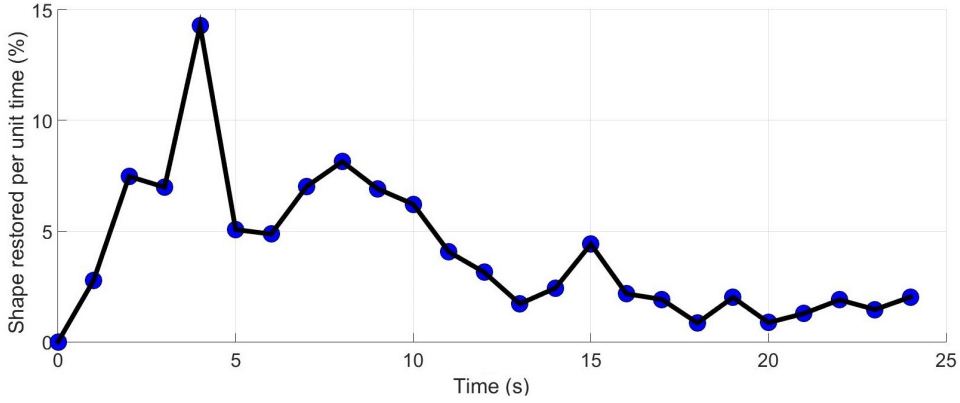

Figure 6.50 Shape recovery rate of the release action in vacuum.

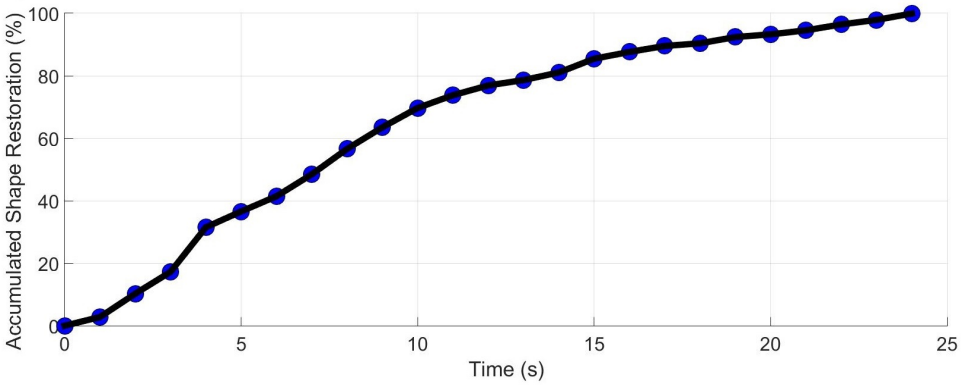

Figure 6.51 Accumulated shape recovery of the release action in vacuum, calculated as a percentage of total recovery.

6.5.6 Release motion in atmosphere

After conducting a release test in vacuum, we then conducted a release test in atmosphere, as shown in Figure 6.52. The test results from both release tests in the two environments were not repeatable due to the heat-damaged arm mounting plate causing the capture arm to start at different positions. We could not get repeatable results from both tests as the capturing arm could not return to identical starting positions, which resulted in the trajectory in both tests being completely different. However, the trajectory described in this test was closer to the programmed shape, compared to the release test in vacuum.

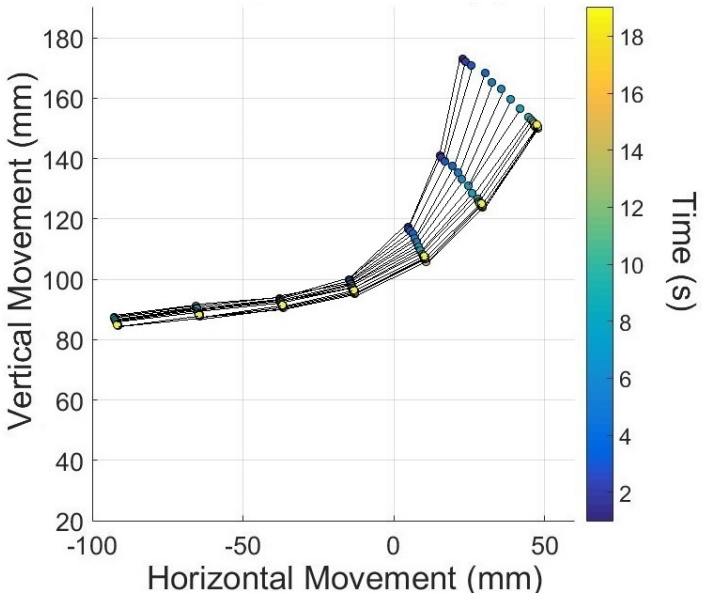

Figure 6.52 Release motion conducted in an atmospheric environment. The first yellow marker was buried in noise; thus we only show markers from 2 to 8.

The trajectory described by the 8th marker on Arm 2 during this test is shown in Figure 6.53. It started at a higher position, then moved to a lower position symbolizing the

opening up of the capturing volume for the next capture attempt. The duration of the release action in atmosphere took 19 seconds.

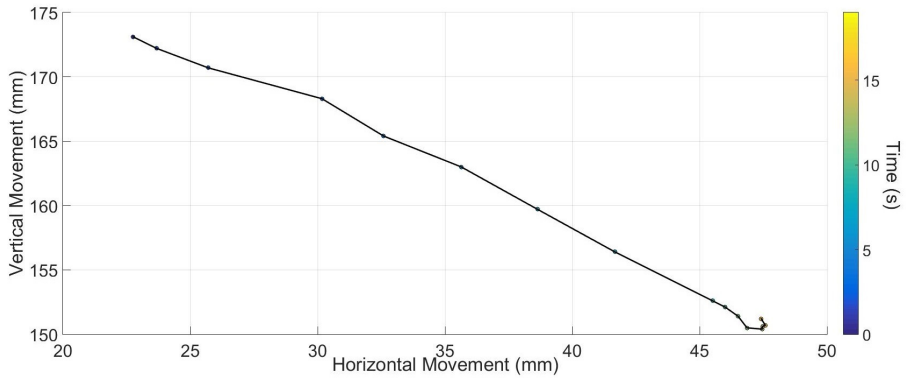

Figure 6.53 Trajectory of the 8th yellow marker during the release motion test in atmosphere. The marker displayed a linear motion starting from the top left and ended at the bottom right.

The velocity of the release motion in atmosphere is depicted in Figure 6.54. The velocity pattern did not follow that observed in the release test in vacuum. Usually the capture arm would require 2 to 3 seconds to warm up before it starts moving. Instead the velocity increased from the first second and reached a first peak at the 3rd second and a second peak at the 8th second. This pattern does not match the velocity trend in vacuum when the capturing arm slowly increased to its peak velocity and declined immediately after the state transition from Martensite state M_f to Austenite state A_s.

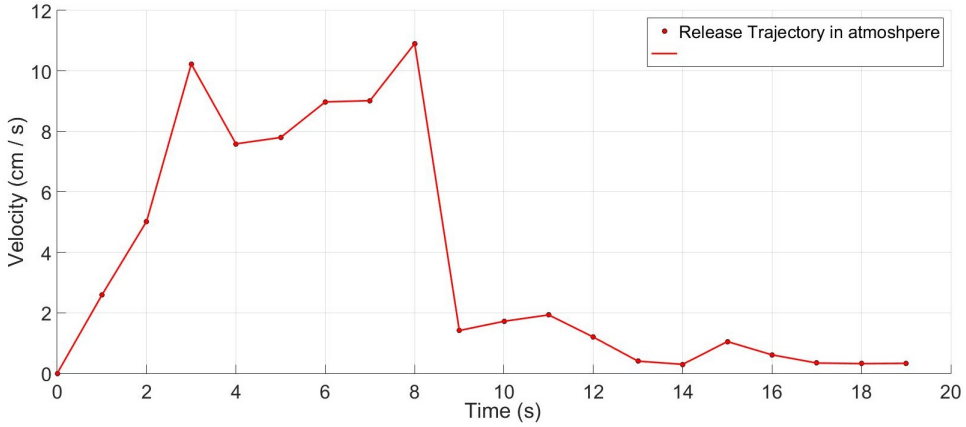

Figure 6.54 Velocity of the 8th yellow marker during the release motion in atmosphere.

The shape restoration pattern shown in Figure 6.55 is very similar to the velocity trend shown in Figure 6.54 because the percentage of shape recovery was calculated by dividing the trajectory completed per second by the total trajectory it covered. This calculating method would be feasible if the trajectory covered was large enough as shown in Figures 6.26 , 6.27 and 6.28. However in the case of the release motion shown in Figure 6.52 this calculation could not accurately reflect the detail of the shape recovery rate.

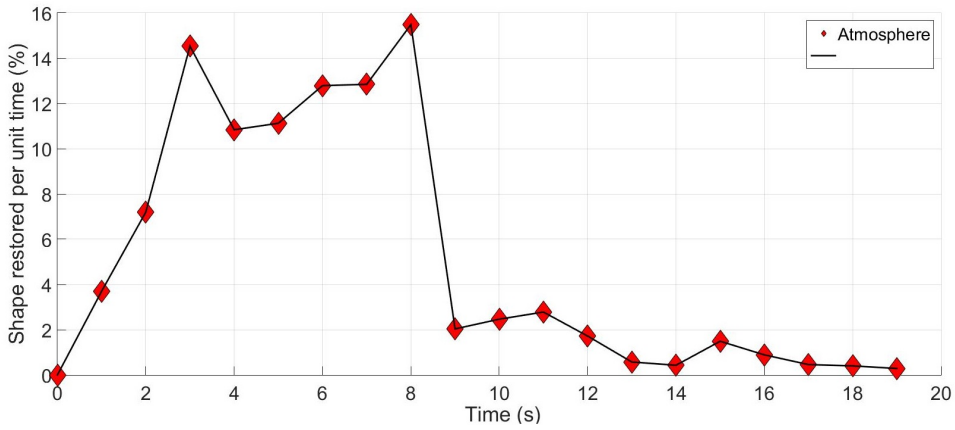

Figure 6.55 Shape recovery rate of the release action in atmosphere.

The accumulated shape restoration calculated in percentages is shown in Figure 6.56, which shows that 80 % of shape restoration was completed during the first 8 seconds and the remaining 20% took 11 seconds to complete.

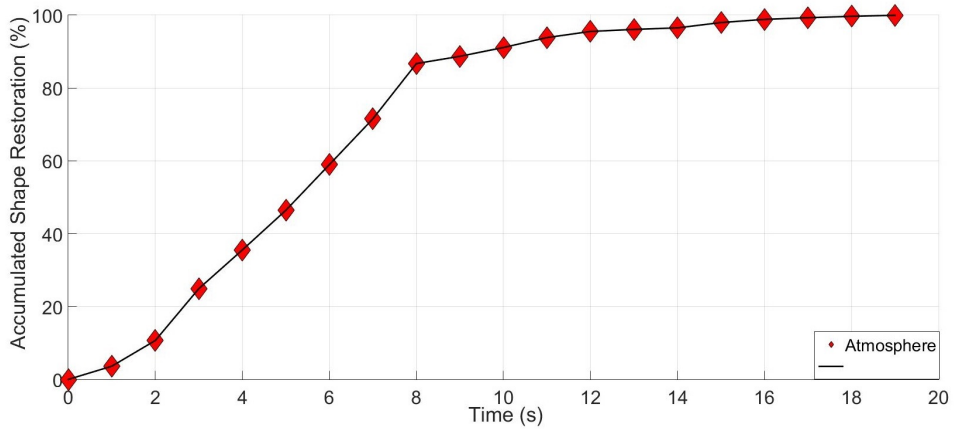

Figure 6.56 Accumulated shape recovery rate of the release action in one atmosphere.

6.5.7 Comparison of release motion in vacuum and atmosphere

We conducted two release tests, one in vacuum and one in atmosphere. However we could not compare the data from these two tests for two reasons. Firstly, the capturing arm started at two significantly different positions, and secondly, the trajectory of the arm was very different in the two tests.

Arm 2 was supposed to restore back to the “L” shape from the capture position, however the arm mounting plate was damaged in previous tests, which made it difficult for Arm 2 to stay in the capture position after the capture motion had executed.

The connection point between Arm 2 and the arm mounting plate was damaged due to over-heating and the arm drooped under its own weight. Nevertheless, Arm 2 managed to recovered back to the ”L” shape sufficiently within 26 seconds in vacuum, which shows that the release actions executed successfully despite the damages to the arm mounting plate.

Comparing the duration of the release test conducted in vacuum to the duration of the release action in atmosphere, which took 19 seconds, that is 7 seconds shorter in atmosphere than in vacuum. This result is likely spurious and caused by the problems described above.

For future development of MEDUSA it is recommended to prototype the arm mounting plate with a more heat resistant material and to conduct the same tests again to obtain better experimental data for analysis.

Chapter 7

Conclusions & Recommendations

7.1 Conclusions

The aim of this thesis was to investigate the potential application of shape memory alloys for space debris remediation applications. For this purpose, we developed the MEDUSA (Mechanism for Entrapment of Debris Using Shape memory Alloy), a proof-of-concept prototype designed to capture a 1U-sized target. The prototype was required to be developed up to a Technology Readiness Level of 4, which meant that it had to be validated in a laboratory environment.

We began by identifying a set of functional requirements to guide the design of MEDUSA and the prototype was also required to have reversible operational ability to allow several capture attempts in a single space mission. After examining existing capturing mechanisms, four different design concepts were considered, and we used the Pugh concept selection method to determine which concept would be most suitable. The fourth conceptual design, "Starfish", was selected for further development. The selected design concept encompasses five capturing arms with protective covers integrated with a free rotating base to rotationally decouple the capturing mechanism from the chaser spacecraft.

The capturing arms were designed to be rectangular and four 1 mm Nitinol wires were chosen to provide the force needed to actuate the capturing mechanism. Polyamide was selected as the material to manufacture the capturing arm body due to its tolerance of high temperature, damping ability and ease to process. The protective sheaths were made out of Kapton HN, which is suitable for this application. A method to construct the capturing arms was conceived and documented. Different programming methods were investigated. Through these investigations we established that a certain amount of "over-programming" could compensate for incomplete shape restoration due to the hysteresis effect in nitinol. A correction factor was calculated and applied to improve the capturing arm's shape restoration ability.

A rotating base unit was designed to mount the five capturing arms and to decouple the MEDUSA system rotationally from the chaser spacecraft. The base unit comprised a square base with a 1U form factor at the bottom and a free rotating ball-bearing

which was connected to a pentagonal arm mounting base on to which the capturing arms are mounted, one per facet. The square-base is the mechanical interface between MEDUSA and the chaser spacecraft that allows the user to install MEDUSA onto a CubeSat standard compliant chaser spacecraft with ease. The ball-bearing was designed to absorb the rotational energy of a captured tumbling space object and prevent it from disturbing the attitude of the chaser spacecraft.

Two test rig were designed and built to support the various laboratory tests. The first test rig was designed to measure resistance and shape restoration time in an atmospheric environment. The second allows us to measure the force generated by MEDUSA during nitinol state transitions while conducting a closing action.

Different tests were conducted as part of the design process and to prove that the prototype would work as intended. These tests included determining the nitinol resistance and current required to execute the capturing function as well as the release function. Following this, various tests were performed with MEDUSA to determine the force it generates during the nitinol state transition when capturing a target. Also a simulated target capturing mission was conducted to demonstrate the capturing application of MEDUSA. A 3-D printed 1U CubeSat was used as a tumbling target in a simulated debris capturing test based in a laboratory environment.

The vacuum chamber PWK1 at the Institute for Space Systems (IRS) at Stuttgart University in Germany was used for vacuum tests of MEDUSA. We documented fourteen capturing tests and thirteen release tests in total to compare the motion and behaviour of MEDUSA when operated in atmospheric and vacuum conditions.

The capturing arms took less time to reach the transition temperature in vacuum due to less heat exchange with ambient background (i.e. no convection), which resulted in the shape restoration actions being completed approximately 5 seconds faster in vacuum than in an atmospheric environment. In vacuum, the temperature of nitinol maintained at 53 ^{0}C within 2 seconds after the input power was switched off due to the lack of air particles needed for heat exchange through convection. Because heat was only transported by radiation and conduction in vacuum, the nitinol wires in capturing arms underwent a higher gradient of temperature increase which produced a faster response with less input power used.

The motions of the capture arms were analysed to establish (i) Movement per second; (ii) Continuous movement during tests; (iii) Trajectories; (iv) Velocity; (v) Calculated percentage of shape restoration per second; and (vi) Accumulated shape restoration during all tests.

Through analysis of physical data obtained we found that the state transition from a Martensite state M_f to an Austenite state A_s was completed 6 seconds faster in vacuum then atmosphere due to the lack of convective cooling in vacuum. The other important observation was that in general 80% of the programmed shape was recovered within 7 seconds while the nitinol was transitioning from the Martensite state M_f to the Austenite state A_s and the remaining 20% took 8 seconds on average to restore when the nitinol state transitioning from the start of the Austenite state A_s to the end of the Austenite

state A_f. If the nitinol wires used to enclose the capturing volume were to be programmed within the 80% fast recovery region it is should be possible to halve the response time and input electrical power.

7.2 Recommendations for future work

Although we have successfully demonstrated the concept validation of the MEDUSA system, there are a number of improvements that could be implemented in the next generation of the device. Some of the recommendations for the next generation prototype are simple material substitutions and others include design changes for practical operational reasons or for performance enhancements. All of these recommendations should be considered during the process of advancing the MEDUSA system to a Technology Readiness Level (TRL) of 5.

7.2.1 Material substitution recommendations

Arm mounting plate material substitution The arm mounting plate was made of 3-D printed PLA and could not withstand the high temperature generated in the nitinol wires during operations. This resulted in deformation of the connection points in the PLA, which caused spurious test results.

There are alternative on 3-D printable polymers that could be considered for prototyping the arm mounting plates. The first option is FDM PPSF (Polyphenylsulfone), a material with high heat and chemical resistance. Its heat deflection temperature is 153 ^{0}C. The second 3-D printable substitute material is ABS Acrylonitrile Butadiene Styrene. ABS is known for higher operating temperature than PLA; its melting point is at 200 ^{0}C, which is 50 ^{0}C higher than PLA. ABS is also a low cost material, allowing for cost-effective prototyping.

Ideal non-polymer substitutes for the arm mounting plate material would be ceramic, because of its high melting temperature and non-conducting nature.

Rotational-decoupler material substitution The metal ball-bearing used in the base unit could be subjected cold-welding in vacuum. The ideal substitution is a ceramic ball-bearing which is immune from cold-welding effects and has a higher long-term service temperature range.

Arm material substitution During the vacuum tests the polyamide used in the body of the capturing arm was burned several times due to the high temperatures reached by the heated nitinol, which were close to the melting temperature of polyamide. Good substitutions would be Polytetrafluroethylene, also known as Teflon, which is commonly used inside vacuum systems with good electrical insulation. The long-term service temperature of Teflon ranges from -73 ^{0}C to 204 ^{0}C.

Sheath material substitution The Kapton 50HN used to manufacture the sheaths in the MEDUSA system was transparent and we recommend to have a metal coated surface that is more light reflective than the uncoated Kapton 50HN. Reflecting

solar radiation would decrease thermal disturbances acting on nitinol wires in the capturing arms.

For higher light reflectivity two possible space-graded substitutes are either Kapton 50HN coated in TiO or space blanket material, which is made out of a thin sheet of plastic (often PET film) that is coated with a metallic reflecting agent, making it metallized polyethylene terephthalate (MPET), usually gold or silver in colour, which reflects up to 97% of incident radiation.

7.2.2 Next generation upgrade recommendations

Increase activation temperature of nitinol In order to decrease the possibility of interference brought about by unexpected thermal disturbances which could deploy MEDUSA without command, we suggest using nitnol with a higher activation temperature than was used in our prototype. The transition temperature of the nitinol used in MEDUSA was specified at 70^0C, but laboratory tests showed that the actual measured transition temperature to be 60^0C. Hence the activation temperature of 95 ^{0}C should be tested upon delivery to make sure the supplier meets the activation temperature requirement.

Design of a Pulse-Width-Modulation (PWM) circuit While activating the nitinol wires with DC current is simple, it is easy to overheat and potentially damage nitinol wires. An investigation into the design of a Pulse-Width-Modulation (PWM) circuit is recommended to regulate the electrical input fed into the nitinol wires in the capture arms. The design of a PWM circuit for MEDUSA may be found in Appendix C and this design should be integrated into the next generation of the MEDUSA system to prolong the lifespan of the nitinol wires by allowing heat to distribute more evenly during activation.

Development of an independent power supply system MEDUSA requires a fairly high power electrical supply for capture and release operations. However it does not require the electrical input continuously. In order to not interfere with the onboard electronic system of a chaser spacecraft an independent power supply system should be developed using super-capacitors to form a power bank which charges up with the energy needed for capture and release motions. One possibility could be to cover the arms of MEDUSA with a flexible photovoltaic material.

7.2.3 Design considerations for the implementation of MEDUSA on a chaser spacecraft

Design a specific ADCS for the chaser spacecraft Due to the possibility of the chaser spacecraft experiencing unbalanced forces while executing capture and release actions, an ADCS system should be developed specifically for the chaser spacecraft on which MEDUSA is installed. When the attitude of chaser spacecraft is perturbed, the ADCS should respond by applying torque to restore the attitude of the chaser spacecraft.

Development of machine vision software for target recognition
Development of a machine vision system for target recognition, together with a binocular vision system would enhance the autonomous capability of the MEDUSA system. The machine vision system should have the capability to determine tumbling rate and tumbling axis of a target object. It must also determine the velocity and the distance between the target and the chaser spacecraft. A machine vision system would allow preliminary visual confirmation of target recognition as well as confirm execution of capturing actions. A camera could be placed in the central open space of the integrated-base unit.

References

[1] Kjetil Wormnes, Ronan Le Letty, Leopold Summerer, Rogier Schonenborg, Olivier Dubois-Matra, Eleonora Luraschi, Alexander Cropp, Holger Krag, and Jessica Delaval. ESA technologies for space debris remediation. In *6th European Conference on Space Debris, Darmstadt, Germany*, pages 22–25, 2013.

[2] Brian Weeden. Overview of active debris removal. In *2010 Beijing Orbital Debris Mitigation Workshop. Secure World Foundation*, 2010.

[3] NASA. Orbital debris - quaterly news. 21(1), February 2017.

[4] Darren S.McKnight Christophe Bonnal. *IAA Situation Report on Space Debris -2016*. International Academy of Astronautics, 2017.

[5] Michael Swartwout. Cubesat database. `https://sites.google.com/a/slu.edu/swartwout/home/cubesat-database`, March 2015. Accessed: October 2017.

[6] Antonio Rinalducci and et al. Guidance, navigation, and control techniques and technologies for active debris removal. `http://iaassconference2013.space-safety.org/wp-content/uploads/sites/28/2013/06/1600_Ortega.pdf`, 2013. Accessed: November 2016.

[7] J-C Liou. An active debris removal parametric study for leo environment remediation. *Advances in Space Research*, 47(11):1865–1876, 2011.

[8] Inter-Agency Space Debris Coordination Committee et al. Iadc space debris mitigation guidelines. *IADC-02-01 Revision*, 1, 2007.

[9] UNCOPUOS. Space debris mitigation guidelines of the committee on the peaceful uses of outer space. Technical Report A/62/20, United Nations Commitee on the Peaceful Uses of Outer Space, 2008.

[10] J-C Liou and Nicholas L Johnson. A sensitivity study of the effectiveness of active debris removal in LEO. *Acta Astronautica*, 64(2):236–243, 2009.

[11] John Wayland Campbell. Project Orion: orbital debris removal using ground-based sensors and lasers. *National Aeronautics and Space Administration, George C. Marshall Space Flight Center, National Technical Information Service, distributor*, 1996.

[12] Brian Weeden. Overview of the legal and policy challenges of orbital debris removal. *Space Policy*, 27(1):38–43, 2011.

[13] Claudio Bombardelli and Jesus Pelaez. Ion beam shepherd for contactless space debris removal. *Journal of guidance, control, and dynamics*, 34(3):916–920, 2011.

[14] Federico Rizzitelli, Marcelo Valdatta, Niccolo Bellini, Paolo Candini Gian, Davide Rastelli, Fedrico Romei, Alfredo Locarini, Antonio Spadanuda, and Sara Bagassi. Active debris removal system based on polyurethane foam. In *ESA Special Publication*, volume 723, page 169, 2013.

[15] D Reintsema, J Thaeter, A Rathke, W Naumann, P Rank, and J Sommer. Deos–the german robotics approach to secure and de-orbit malfunctioned satellites from low earth orbits. In *Proceedings of the i-SAIRAS*, pages 244–251, 2010.

[16] A Wayman, A Ractcliffe, S Barraclough, J Lurie, I Fernandez-Nunez, M Lupsa, S Aziz, K Wormnes, M Zwick, N Taylor, A Jardine, and J Campbell. Design and testing of a full scale harpoon capture system. In *Proceedings of the 7th European Space Debris Conference*, 2017.

[17] Oluwaseun A Araromi, Irina Gavrilovich, Jun Shintake, Samuel Rosset, Muriel Richard, Volker Gass, and Herbert R Shea. Rollable multisegment dielectric elastomer minimum energy structures for a deployable microsatellite gripper. *IEEE/ASME Transactions on Mechatronics*, 20(1):438–446, 2015.

[18] Thomas Wolf. Deutsche orbital servicing mission. `http://robotics.estec.esa.int/ASTRA/Astra2011/Presentations/Plenary202/04_wolf.pdf`, 2013. Accessed: November 2016.

[19] Thomas Rupp, Toralf Boge, Reinhard Kiehling, and Florian Sellmaier. Flight dynamics challenges of the german on-orbit servicing mission deos. In *21st international symposium on space flight dynamics*, volume 22. Citeseer, 2009.

[20] J Reed, J Busquets, and C White. Grappling system for capturing heavy space debris. In *2nd European Workshop on Active Debris Removal*, 2012.

[21] John C Mankins. Technology readiness levels. *White Paper*, 6(6):1995.

[22] Anne Dorothy Marinan. *From CubeSats to constellations: systems design and performance analysis*. PhD thesis, Massachusetts Institute of Technology, 2013.

[23] Encyclopedia Magnetica. Supra50. `http://www.encyclopedia-magnetica.com/doku.php/supra_50`. Accessed: March 2017.

[24] Cubespace. Cubespace adcs. `https://www.cubespace.co.za/cubetorquer`. Accessed: February 2017.

[25] Sutart Pugh. Concept selection - based on the work of professor stuart pugh: “design decision - how to succeed and know why”. `http://edge.rit.edu/edge/P10505/public/Pugh%20Concept%20Selection.pdf`, 1987. Accessed: August 2017.

[26] National Aeronautics and Space Administration NASA. Outgassing data for selecting spacecraft materials online. `https://outgassing.nasa.gov/`, 2008. Accessed: July 2016.

[27] JOHNSON MATTHEY MEDICAL COMPONENTS. Measuring transformation temperature in nitinol alloys. http://jmmedical.com/resources/211/Measuring-Transformation-Temperatures-in-Nitinol-Alloys.html. Accessed: Jan. 25,2009.

[28] Marek Novotny and Juha Kilpi. Shape memory alloys (sma). *on: http://www. ac. tut. fi/aci/courses/ACI-51106/pdf/SMA/SMA-introduction. pdf*, 2001.

[29] TiNi Alloy Company. Introduction to shape memory alloys. http://www.tinialloy.com/pdf/introductiontosma.pdf. Accessed: March 2017.

[30] M and T(Taiwan) Co.Ltd. Measuring transformation temperature in nitinol alloys. http://www.twmt.url.tw/product_494324.html. Accessed: February 2017.

[31] Irina Gavrilovich. Study of a dielectric elastomer gripper for cleanspace one, 2013.

[32] G Herdrich, M Fertig, and S Löhle. Experimental simulation of high enthalpy planetary entries. *Open Plasma Physics Journal*, 2:150–164, 2009.

[33] Michael Dropmann, Mudi Chen, Hannah Sabo, Rene Laufer, Georg Herdrich, LS Matthews, and Truell W Hyde. Mapping of force fields in a capacitively driven radiofrequency plasma discharge. *Journal of Plasma Physics*, 82(04):615820401, 2016.

[34] Hunter Song, Eric Kubica, and Rob Gorbet. Resistance modelling of sma wire actuators. In *International Workshop Smart Materials Structures & NDT in Aerospace*, pages 2–4, 2011.

Appendix A

Data sheet of capturing arm components

A.1 Nitinol datasheets - The skeleton of capturing arms

Material Data Sheet

Shape Memory Nitinol Alloys*

	SM495	SM500
PHYSICAL PROPERTIES		
Melting Point:	1310℃	1310℃
Density:	6.5 g/cm^3	6.5 g/cm^3
Electrical Resistivity:	76 µohm-cm	76 µohm-cm
Modulus of Elasticity:	28 – 41 GPa	28 – 41 GPa
Coefficient of Thermal Expansion:	6.6 x 10^{-6} / ℃	6.6 x 10^{-6} / ℃
MECHANICAL PROPERTIES		
Ultimate Tensile Strength:	≥ 1070 MPa	≥ 1070 MPa
Total Elongation:	≥ 10%	≥ 10%
SHAPE MEMORY PROPERTIES		
Loading Plateau Stress @ 3%	≥ 100 MPa	≥ 100 MPa
Shape Memory Strain	≤ 8.0%	≤ 8.0%
TRANSFORMATION TEMPERATURE		
Ingot Austenite Finish (A_f)	75 to 110℃	45℃ to 80℃
Finished Product A_f	50 to 80℃	30℃ to 50℃
COMPOSITION (Meets ASTM F2063 requirements)		
Nickel (nominal):	54.5 wt.%	55.0 wt.%
Titanium:	Balance	Balance
Oxygen:	≤ 0.05 wt.%	≤ 0.05 wt.%
Carbon:	≤ 0.02 wt.%	≤ 0.02 wt.%
Inclusion Area Fraction:	≤ 2.8%	≤ 2.8%
APPLICATIONS		
	SM495 is our standard shape memory wire that is malleable at room temperature and returns to shape in boiling water or autoclave. Typical applications for the material are actuators and surgical tools.	SM500 exhibits shape memory such that it is malleable at room temperature and returns to shape just above body temperature. Typical applications for SM500 are for dental products such as archwires and springs.

* These values should only be used as guidelines for developing material specifications. Properties of Nitinol Alloys are strongly dependent on processing history and ambient temperature. The mechanical and shape memory properties shown here are typical for standard shape memory Nitinol at room temperature tested in uniaxial tension. Bending properties differ, and depend on specific geometries and applications. Modulus is dependent on temperature and strain. Certain shapes or product configurations may require custom specifications. Materials are also available in the cold-worked or annealed conditions.

Nitinol Devices & Components • 47533 Westinghouse Drive • Fremont, California 94539
(510)683-2000 • Fax: (510)683-2001 • sales@nitinol.com • www.nitinol.com

We are Nitinol.™

A.2 Polyamide datasheets - The flesh of capturing arms

POLYAMIDE - SUSTAMID 6G NYLON

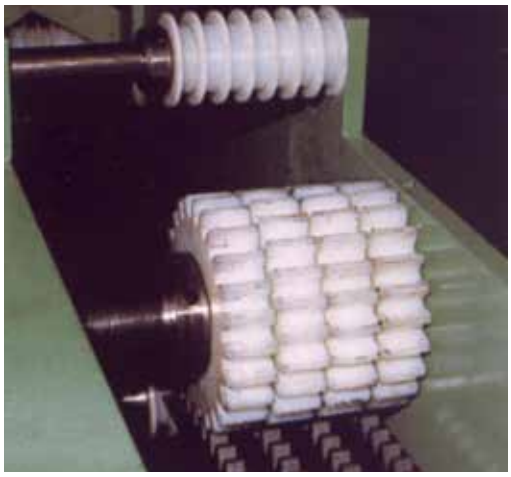

The casting process used to manufacture Sustamid 6G produces in a high-molecular and highly crystalline polyamide type 6 material with outstanding physical properties. Sustamid PA6 G has similar mechanical properties and chemical resistance to a standard Nylon 66. Stock shapes are available in sheet, rod or tube form in a wide selection of sizes.

PROPERTIES:

- Good sliding properties.
- Extremely high abrasion resistance.
- High mechanical strength coupled with high impact strength.
- Good machinability.
- High mechanical damping ability.
- Working temperature range of -40°C to 110°C continuous.
- EU & FDA approved for direct food contact applications.
- High absorption of moisture (of up to 3 % in standard atmosphere) results in increased impact resistance.

Please note: In thin-walled parts, reduced mechanical strength and dimensional stability.

APPLICATIONS:

Sustamid is frequently used as a substitute for aluminium, brass or bronze. Used for a wide range of industrial components both for Original Equipment Manufacture and maintenance.

Mechanical engineering: e.g. sliding parts, rollers, bushes, slide bearings, wear pads, support and guide wheels, sprockets tension rollers.
Offshore: e.g. bogies, cable winches, sheaves.
Vehicle construction: e.g. sliding parts, hoisting gear, rope pulleys.
Foodstuffs industry: e.g. sliding parts, conveyor stars wheels, spiral conveyors, feed screws.

DELIVERY PROGRAMME

Ex Stock from Maizey branches:
Rods | Sheets | Tubes |
Finished Parts | Custom Castings

maizey
ENGINEERING PLASTIC PRODUCTS

Stock Shapes and Finished Components
NATIONAL DISTRIBUTION - 086 110 0420

Maizey Engineering Finished Components Only
Tel: (011) 824-2751 | Fax: (011) 824-1829
Email: epp@maizey.co.za | Web: www.maizeyepp.co.za

SUSTAMID 6G NYLON (POLYAMIDE)					
PROPERTIES	TEST METHOD	UNIT OF MEASURE	SUSTAMID		
			6 G	6 G MO	6 G OL
GENERAL					
DENISTY	DIN EN ISO 1183-1	g/cm³	1,15	1,15	1,14
WATER ABSORPTION	DIN EN ISO 62	%	2,5	2,5	2
FLAMABILITY 3mm	UL 94	3mm	HB	HB	HB
FLAMABILITY 6mm	UL 94	6mm	V2	HB	HB
MECHANICAL					
TENSILE STRENGTH	DIN EN ISO 527	MPA	75	82	70
ELONGATION AT BREAK	DIN EN ISO 527	%	>45	>35	>50
E MODULUS	DIN EN ISO 527	MPA	3 400	3 500	3 300
NOTCHED IMPACT STRENGTH	DIN EN ISO 179	kJ/m²	>3.0	>2.5	>4.0
BALL INDENTATION HARDNESS	DIN EN ISO 2039-1	MPA	180	185	165
SHORE HARDNESS	DIN EN ISO 868	SCALED	83	83	82
THERMAL					
MELTING TEMPERATURE	ISO 11357-3	°C	260	216	213
THERMAL CONDUCTIVITY	DIN 52612-2	W/(m.K)	0,25	0,25	0,25
SPECIFIC THERMAL CAPACITY	DIN 52612	kJ/(kg.K)	1,7	1,7	1,7
COEFFICIENT OF LINEAR THERMAL EXPANSION	DIN 53752	10^{-6} K-1	80	80	80
LONG TERM SERVICE TEMPERATURE	GUIDELINE ONLY	°C	- 40 TO 110	- 40 TO 110	- 40 TO 110
SHORT TERM SERVICE TEMPERATURE	GUIDELINE ONLY	°C	170	170	160
HEAT DEFLECTION TEMPERATURE	DIN EN ISO 75.VERF.A	°C	95	95	90
ELECTRICAL					
DIELECTRIC CONSTANT	IEC 60250	N/A	3,7	N/A	N/A
DIELECTRIC DISSIPATION FACTOR	IEC 60250	N/A	0,02	N/A	N/A
SPECIFIC VOLUME RESISTIVITY	IEC 60093	Ω.cm	10^15	N/A	N/A
SURFACE RESISTIVITY	IEC 60093	Ω	10^13	N/A	N/A
DIELECTRIC STRENGTH	IEC 60243	kV/mm	20	N/A	N/A

When machining thermoplastic stock shapes, remember…

- Thermal expansion is up to 10 times greater with plastics than metals.
- Plastics lose heat more slowly than metals, so avoid localized overheating.
- Softening (and melting) temperatures of plastics are much lower than metals and plastics are much more elastic than metals.

Getting started

- Positive tool geometries with ground peripheries are recommended.
- HSS/Tip tooling with polished top surfaces is suggested for optimum tool life and surface finish.
- Use adequate chip clearance to prevent clogging.
- Adequately support the material to restrict deflection away from the cutting tool.

Coolants

Coolants are generally not required for most machining operations, but are strongly suggested during drilling operations, especially with notch sensitive materials such as Nylon, PET-P, PAI, PBI and glass or carbon reinforced products.

In addition to minimizing localized part heat-up, coolants prolong tool life. For optimum surface finishes and close tolerances, non-aromatic, water soluble coolants are suggested. General purpose petroleum based cutting fluids, although suitable for many metals and plastics, may contribute to stress cracking of amorphous plastics such as Polycarbonate.

Because of these differences, you may wish to experiment with fixtures, tool materials, angles, speeds and feed rates to obtain optimum results.

GENERAL NOTE:

The data shown fall within the normal parameters of product properties. They should only be used as a guide to initial material selection for the relevant application and for material specification limits. Further technical information is available for specific application requirements. When no value is listed, insufficient details were available to present a usable value.

A.3 Kapton HN datasheets - The skin of capturing arms

DUPONT™ KAPTON® HN

POLYIMIDE FILM

DESCRIPTION

DuPont™ Kapton® HN general-purpose film has been used successfully in applications at temperatures as low as -269°C (-452°F) and as high as 400°C (752°F). HN film can be laminated, metallized, punched, formed or adhesive coated. Kapton® HN is the recommended choice for applications that require an all-polyimide film with an excellent balance of properties over a wide range of temperatures.

APPLICATIONS

- Mechanical parts
- Electronic parts
- Electrical Insulation
- Pressure sensitive tape
- Fiber optics cable
- Insulation blankets
- Insulation tubing
- Automotive diaphragms sensors and manifolds
- Etching
- Shims

PRODUCT SPECIFICATIONS

Kapton® HN is manufactured, slit and packaged according to the product specifications listed in H-38479, Bulletin GS-96-7.

CERTIFICATION

Kapton® HN meets ASTM D-5213 (type 1, item A) requirements.

DUPONT™ KAPTON® HN

Table 1 – Physical Properties of DuPont™ Kapton® HN at 23°C (73°F)

Property	Unit	1 mil 25µm	2 mil 50µm	3 mil 75µm	5 mil 125µm	Test Method
Ultimate Tensile Strength at 23°C, (73°F) at 200°C (392°F)	psi (MPa)	33,500(231) 20,000(139)	33,500(231) 20,000(139)	33,500(231) 20,000(139)	33,500(231) 20,000(139)	ASTM D-882-91, Method A*
Ultimate Elongation at 23°C, (73°F) at 200°C (392°F)	%	72 83	82 83	82 83	82 83	ASTM D-882-91, Method A
Tensile Modulus at 23°C, (73°F) at 200°C (392°F)	psi (GPa)	370,000 (2.5) 290,000 (2.0)	370,000 (2.5) 290,000 (2.0)	370,000 (2.5) 290,000 (2.0)	370,000 (2.5) 290,000 (2.0)	ASTM D-882-91, Method A
Density	g/cc	1.42	1.42	1.42	1.42	ASTM D-1505-90
MIT Folding Endurance	cycles	285,000	55,000	6,000	5,000	ASTM D-2176-89
Tear Strength-propagating (Elmendorf), N (lbf)		0.07 (0.02)	0.21 (0.02)	0.38 (0.02)	0.58 (0.02)	ASTM D-1922-89
Tear Strength, Initial (Graves), N (lbf)		7.2 (1.6)	16.3 (1.6)	26.3 (1.6)	46.9 (1.6)	ASTM D-1004-90
Yield Point at 3% at 23°C, (73°F) at 200°C (392°F)	MPa (psi)	69 (10,000) 41 (6,000)	69 (10,000) 41 (6,000)	69 (10,000) 41 (6,000)	69 (10,000) 41 (6,000)	ASTM D-882-91
Stress to produce 5% elong. at 23°C, (73°F) at 200°C (392°F)	MPa (psi)	90 (13,000) 61 (9,000)	90 (13,000) 61 (9,000)	90 (13,000) 61 (9,000)	90 (13,000) 61 (9,000)	ASTM D-882-92
Impact Strength at 23°C, (73°F)	N·cm·(ft lb)	78 (0.58)	78 (0.58)	78 (0.58)	78 (0.58)	DuPont Pneumatic Impact Test
Coefficient of Friction, kinetic (film-to-film)		0.48	0.48	0.48	0.48	ASTM D-1894-90
Coefficient of Friction, static (film-to-film)		0.63	0.63	0.63	0.63	ASTM D-1894-90
Refractive Index (sodium D line)		1.70	1.70	1.70	1.70	ASTM D-542-90
Poisson's Ratio		0.34	0.34	0.34	0.34	Avg. three samples, elongated at 5, 7, 10%
Low temperature flex life		pass	pass	pass	pass	IPC-TM-650, Method 2.6.18

*Specimen size 25 x 150 mm (1.6 in); jaw separation 100 mm (4 in), jaw speed, 50mm/min (2 in/min). Ultimate refers to the tensile strength and elongation measured at break.

Table 2 – Thermal Properties of DuPont™ Kapton® HN Film

Thermal Property	Typical Value	Test Condition	Test Method
Melting Point	None	None	ASTM E-794-85 (1989)
Thermal Coefficient of Linear Expansion	20 ppm/°C (11 ppm/°F)	-14 to 38°C (7 to 100°F)	ASTM D-696-91
Coefficient of Thermal Conductivity, W/m·K $\frac{\text{cal}}{\text{cm·sec·°C}}$	0.12 2.87×10^{4}	296K 23°C	ASTM F-433-77 (1987)
Specific Heat, J/g•K (cal/g·°C)	1.09 (0.261)		Differential calorimetry
Heat Sealability	not heat sealable		
Solder Float	pass		IPC-TM-650 Method 2.4.13A
Smoke Generation	D_m=<1	NBS smoke chamber	NFPA-258
Shrinkage, % 30 min at 150°C 120 min at 400°C	0.17 1.25		IPC-TM-650 Method 2.2.4A; ASTM D-5214-91
Limiting Oxygen Index, %	37–45		ASTM D-2863-87
Glass Transition Temperature (T_g)	A second order transition occurs in Kapton® between 360°C (680°F) and 410°C (770°F) and is assumed to be the glass transition temperature. Different measurement techniques produce different results within the above temperature range.		

DUPONT™ KAPTON® HN

Table 3 – Typical Electrical Properties of DuPont™ Kapton® HN Film at 23°C (73°F), 50% RH

Property Film Gage	Typical Value		Test Condition	Test Method
Dielectric Strength	**V/m kV/mm**	**(V/mil)**		
25 µm (1 mil)	303	(7700)	60 Hz	
50 µm (2 mil)	240	(6100)	1/4 in electrodes	ASTM D-149-91
75 µm (3 mil)	205	(5200)	500 V/sec rise	
125 µm (5 mil)	154	(3900)		
Dielectric Constant				
25 µm (1 mil)	3.4		1 kHz	ASTM D-150-92
50 µm (2 mil)	3.4			
75 µm (3 mil)	3.5			
125 µm (5 mil)	3.5			
Dissipation Factor				
25 µm (1 mil)	0.0018		1 kHz	ASTM D-150-92
50 µm (2 mil)	0.0020			
75 µm (3 mil)	0.0020			
125 µm (5 mil)	0.0026			
Volume Resistivity	·cm			
25 µm (1 mil)	1.5 x 1017			ASTM D-257-91
50 µm (2 mil)	1.5 x 1017			
75 µm (3 mil)	1.4 x 1017			
125 µm (5 mil)	1.0 x 1017			

DIMENSIONAL STABILITY

The dimensional stability of DuPont™ Kapton® polyimide film depends on two factors–the normal coefficient of thermal expansion and the residual stresses placed in the film during manufacture. The latter causes Kapton® to shrink on its first exposure to elevated temperatures as indicated in the bar graph in **Figure 1.** Once the film has been exposed, the normal values of the thermal coefficient of linear expansion as shown in **Table 4** can be expected.

Figure 1. Residual Shrinkage vs. Exposure Temperature and Thickness, DuPont™ Kapton® HN

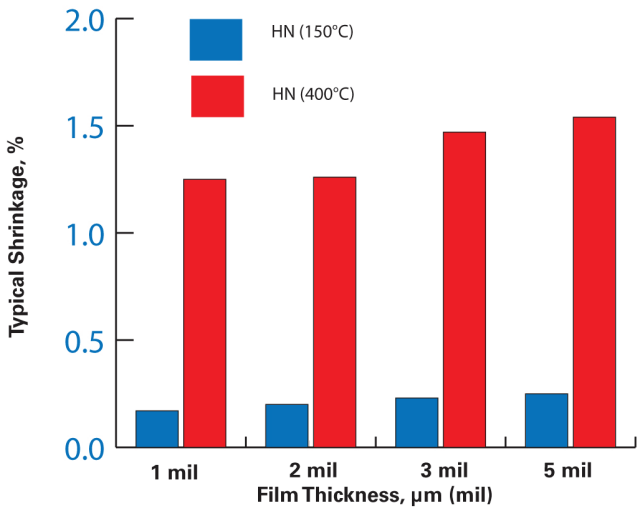

Table 4 – Thermal Coefficient of Expansion, DuPont™ Kapton® HN Film, 25 µm (1 mil), Thermally Exposed

Temperature Range, °C, (°F)	ppm/°C
30–100 (86–212)	17
100–200 (212–392)	32
200–300 (392–572)	40
300–400 (572–752)	44
30–400 (86–752)	34

DUPONT™ KAPTON® HN

FOR MORE INFORMATION ON DUPONT™ KAPTON® POLYIMIDE FILMS, PLEASE CONTACT YOUR LOCAL REPRESENTATIVE, OR VISIT OUR SALES & SUPPORT WEBPAGE FOR ADDITIONAL REGIONAL CONTACT INFORMATION.

kapton.com

K-15345-2 (12/16)

A.4 Kapton tape datasheets

K6338A

KAPTON® SILICONE TAPE

Description

K6338A is a Kapton® film coated with a silicone adhesive

Main Characteristics		
Adhesive Type		*Silicone*
Thermal Classification		*H (180°C)**
Backing Thickness	*(mm)*	*0.025*
Total Thickness	*(mm)*	*0.065*
Peel Strength	*(N/cm)*	*3.0*
Tensile Strength	*(N/cm)*	*45*
Elongation	*(%)*	*60*
Dielectric Strength	*(Volts)*	*6000*

* Short term 260°C

Kapton® is a DuPont registered trade mark

Lohmann Adhesive Tape Systems
25 Kelvin Drive, Knowlhill,
Milton Keynes, MK5 8NH
Tel: 01296 337 888
e-mail: info@lohmann-tapes.co.uk

Appendix B

Engineering drawing of Integrated-base unit

B.1 Integrated-base unit - Square Base

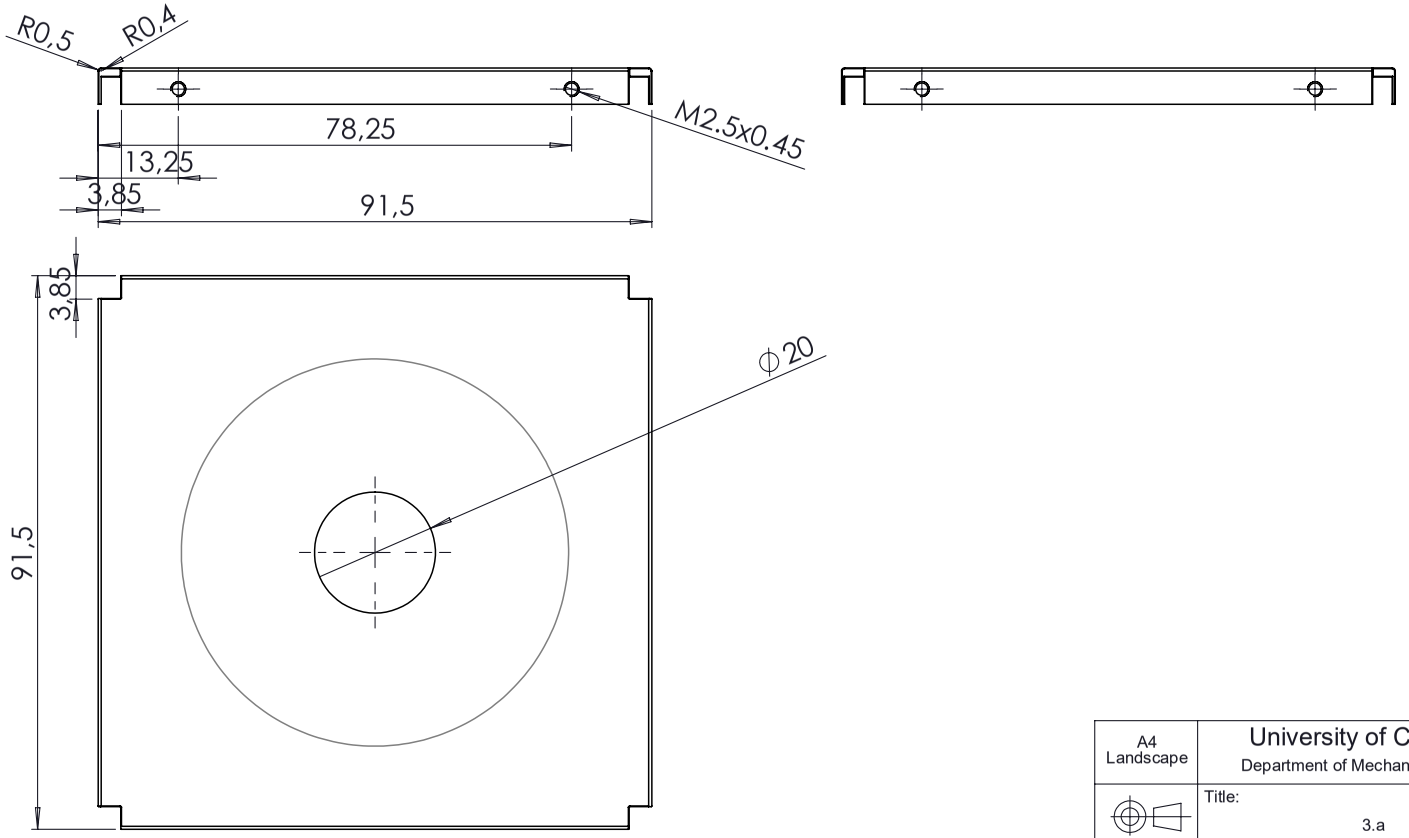

A4 Landscape	University of Cape Town Department of Mechanical Engineering				
	Title: 3.a				
Quantity: 1	Part Finish	Date: 2017/03/19	Scale: 1:2	Sheet1	of 1
Material:	Drawn By: Kai-Yu Feng			Drawing Number 1	

B.2 Integrated-base unit - Cylinder

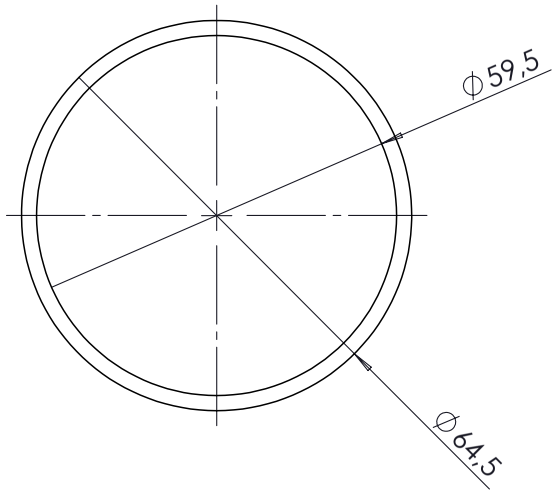

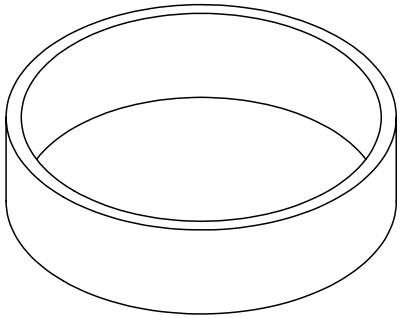

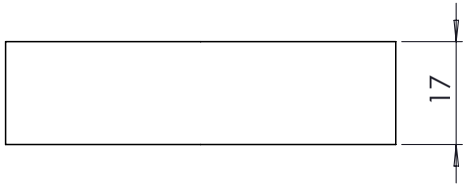

A4 Landscape	University of Cape Town Department of Mechanical Engineering				
	Title: 3.b				
Quantity: 1	Part Finish	Date: 2017/03/19	Scale: 1:2	Sheet1	of 1
Material:	Drawn By: Kai-Yu Feng			Drawing Number 3	

B.3 Integrated-base unit - Arm-mounting plate

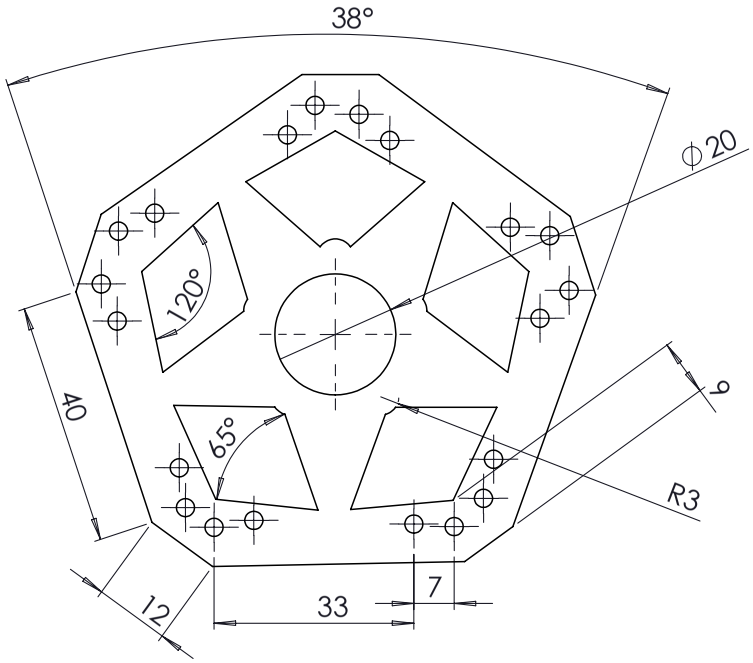

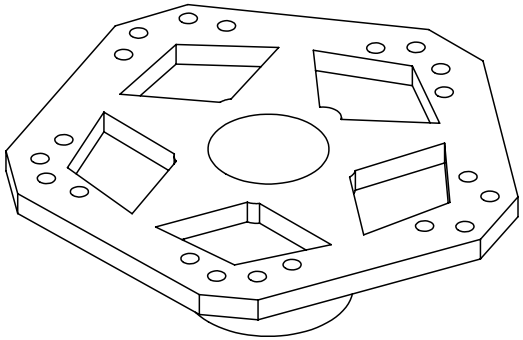

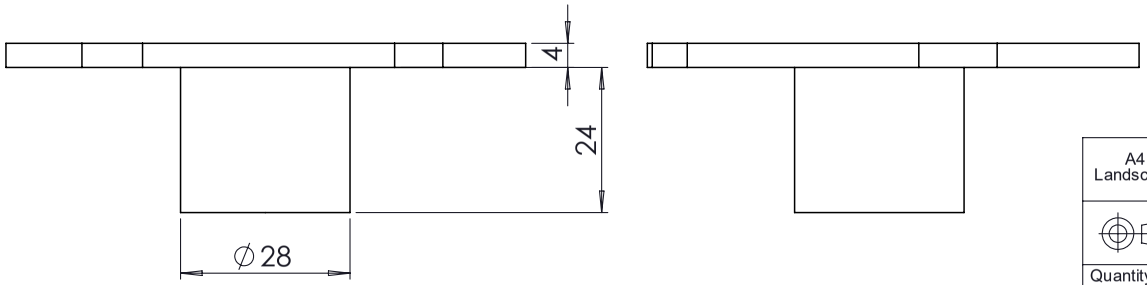

SOLIDWORKS Educational Product. For Instructional Use Only

A4 Landscape	University of Cape Town Department of Mechanical Engineering				
	Title: 5 sided lid				
Quantity: 1	Part Finish	Date: 2017/03/19	Scale: 1:2	Sheet1	of 1
Material:	Drawn By: Kai-Yu Feng			Drawing Number 2	

Appendix C

Design of a PWM circuit

While activating the nitinol with DC current is simple it is easy to overheat and potentially damage nitinol wires. The use of a PWM circuit has distinctive advantages by switching the input current on and off controlled by a duty cycle. Rate of switching is commonly denoted as duty cycle set by the user. The oscillating on-off reduces cold and hot spots by allowing heat distribute more evenly. The duty cycle of the square wave output can be varied from fully on (100%) to fully off (0%). These factors allow us to activate the nitinol wire with better control without causing heat damage to the crystalline structure and thus prolong the usable lifetime of nitinol wires.

A PWM circuit designed and simulated in MATLAB is shown in Figure C.1. We built the simulation model using the SIMULINK package to get detailed electrical input fed into MEDUSA shown in Figure C.2. Figure C.2 demonstrates how input current can be controlled via duty cycle. Parameters used for simulation are shown in Table C.1.

Table C.1 *MATLAB PWM circuit simulation parameters*

Parameters	**Value**
Supply Voltage	15 volts
Resistor (R1)	100 Ω
Resistor (R2)	1 kΩ
Capacitor (C1)	20 nF
Capacitor (C2)	10 nF
Potentiometer (P1)	1k Ω
Diode (D1)	Forward voltage 0,6 V
Diode (D2)	Forward voltage 0,6 V
Duty Cycle	65 %

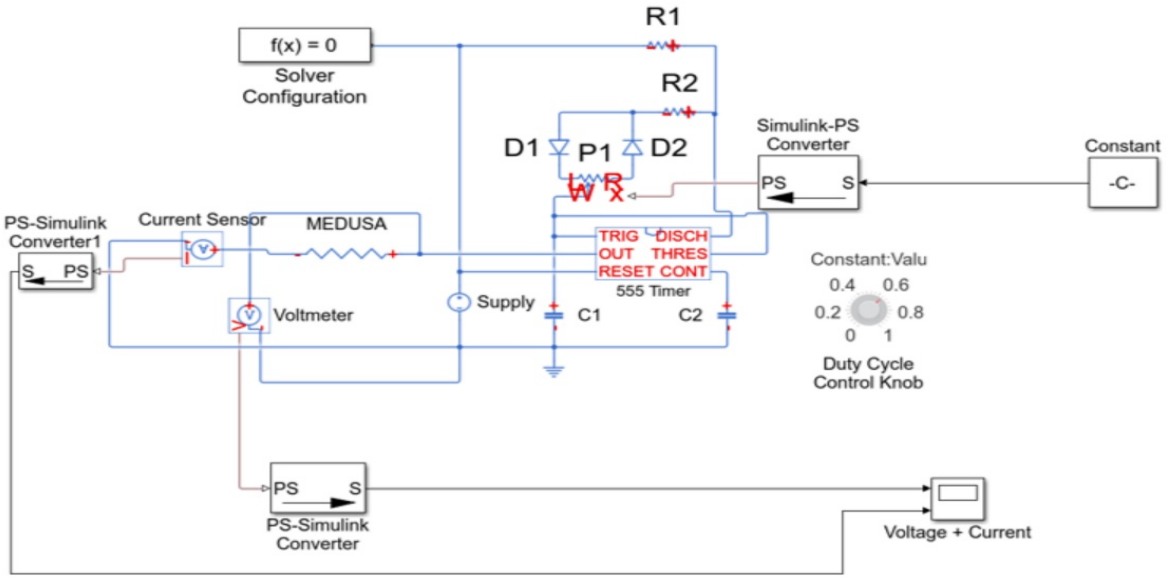

Figure C.1 PWM circuit simulation model built in MATLAB SIMULINK.

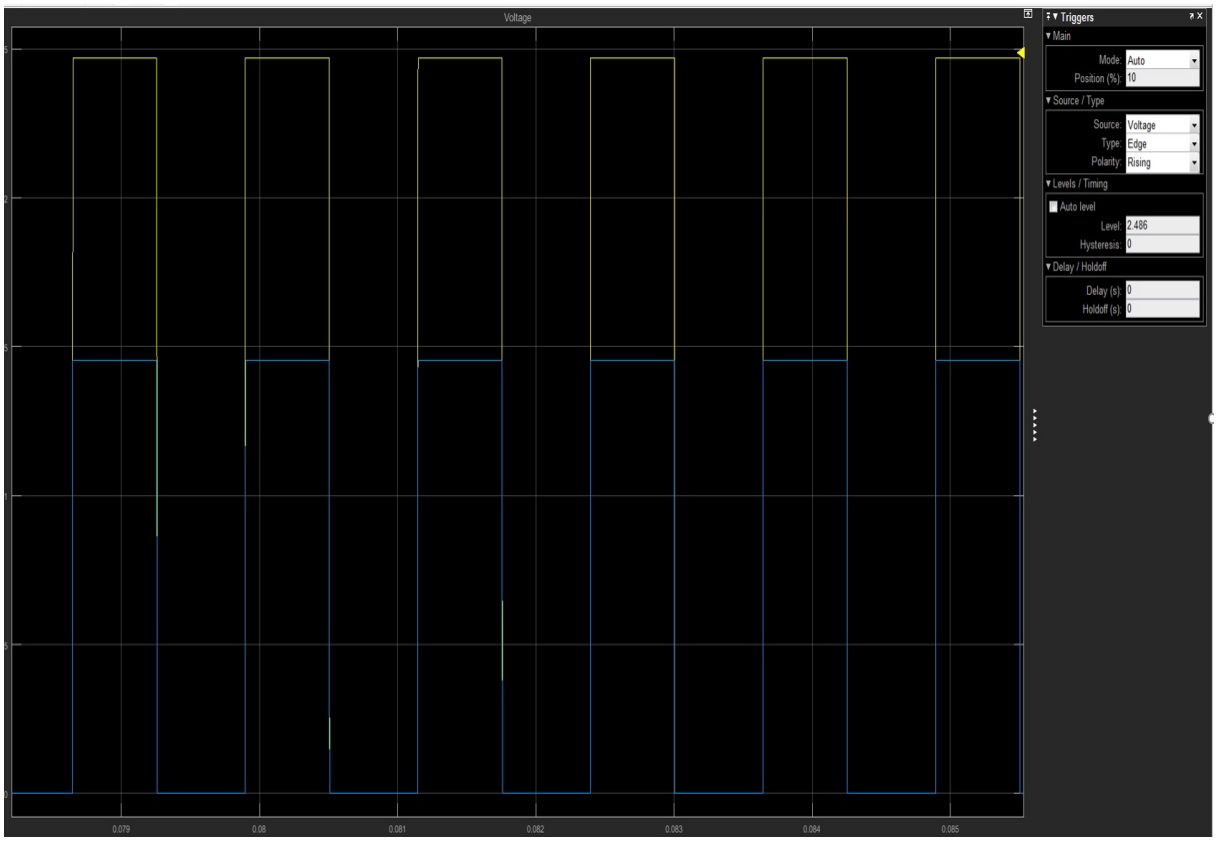

Figure C.2 Simulation results demonstrating input power in square wave format switching on and off at a duty cycle rate of 65 %.

Appendix D

Delayed temperature measurement using thermocouple K1 and K2

D.1 Delayed temperature measurement using thermocouple K1 and K2

D.2 Data obtained from vacuum chamber tests and atmospheric tests

Raw data obtained from vacuum chamber tests are shown in Figure D.1 and Figure D.2. In the vacuum tests four capture actions and three release actions were conducted. An extra capture action was conducted to test thermocouple response.

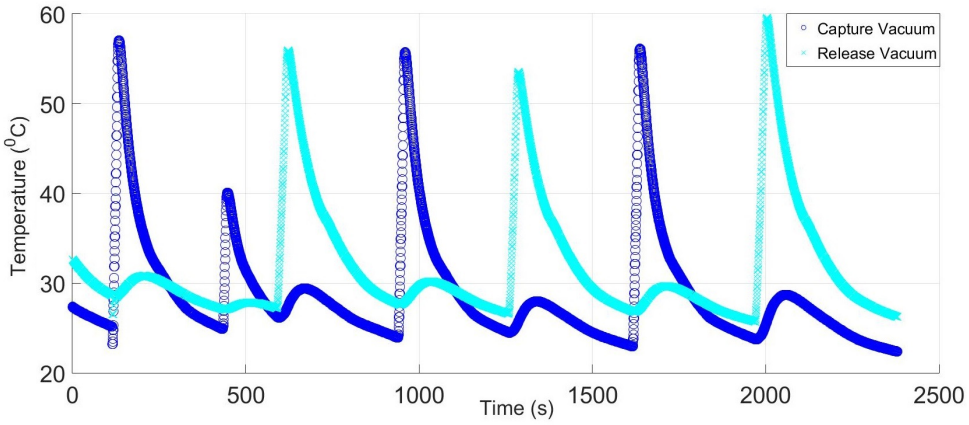

Figure D.1 C-circuit and R-circuit temperature data obtained during tests in a vacuum environment. These data originated from conducting four capture actions and three release actions of MEDUSA arm 2 in PWK1.

In the atmospheric tests, three capture actions and three release actions were conducted. A data analysis code was written in MATLAB to extract the desired data and put data in sets for comparisons.

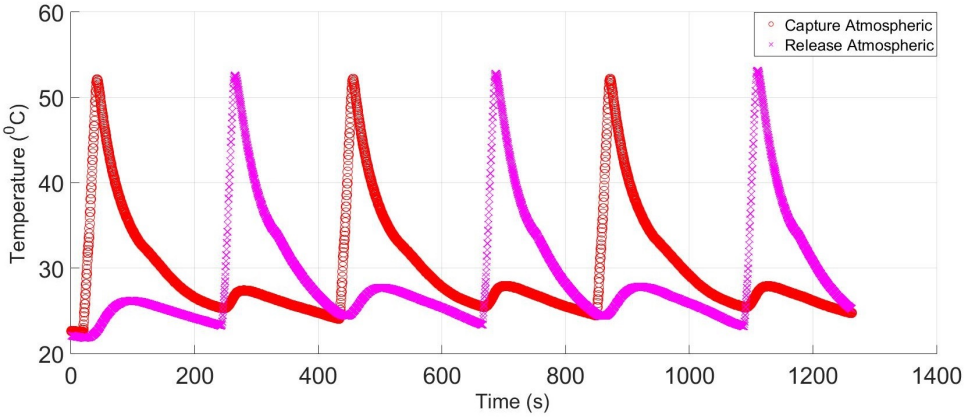

Figure D.2 C-circuit and R-circuit temperature data obtained during tests in an atmospheric environment. These data originated from conducting three capture actions and three release actions in PWK1.

D.3 Temperature rise of the C-circuit and R-circuit

In this section, we describe temperature data recorded during capture and release action tests conducted in vacuum and atmosphere. We supplied 9.89V and 5.2A to both the C-circuit and R-circuit in vacuum and atmospheric environments.

The data collected during these tests includes the time taken to reach a specific temperature as it determines the time required to complete capture actions and release actions in both atmosphere and vacuum environments. Less time taken to reach transition temperature ensures a faster response, thus improving the prospects of a successful debris capture operation in space.

The data sets shown in Figure D.3 compare the time taken for the capturing nitinol to reach the desired temperature in vacuum and in an atmospheric environment. The second data sets in Figure D.4 show the time taken to reach the desired temperature for the release nitinol in vacuum and atmosphere. The two programmed shapes exhibited different rates of shape recovery.

It is evident from both Figures D.3 and D.4 that the temperature in the nitinol circuits rises faster in a vacuum compared to that in an atmosphere. This is because in a vacuum heat is only transported by two effects, conduction and radiation, which causes heat to escape from nitinol at a slower rate in a vacuum than in an atmosphere. As less time is required to reach the desired temperature in a vacuum, less electrical power is required to operate MEDUSA in that environment.

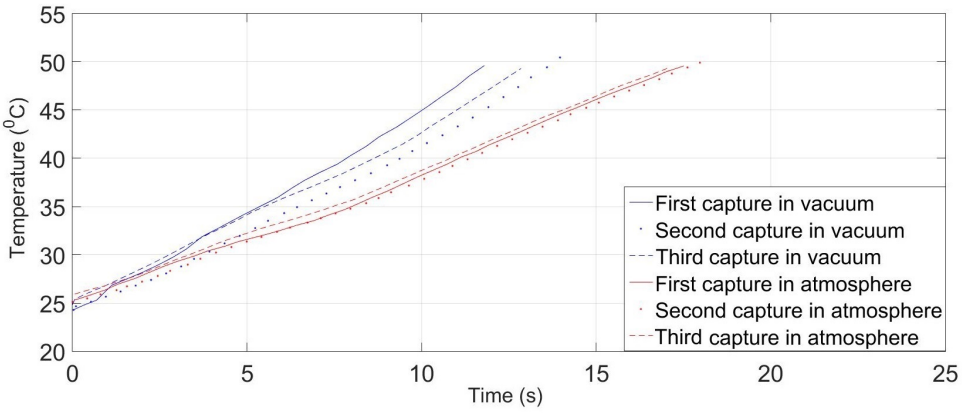

Figure D.3 Temperature rise recorded in the capture nitinol circuit in vacuum and atmosphere. Three capture actions were conducted in both environments.

Furthermore, in both Figures D.3 and D.4 a slight temperature gradient change was observed in the early stages of heating the nitinol as it was transforming from the Martensite state M_f to the Austenite state A_s. Thus we can conclude that the temperature gradient of the nitinol is different in the two states. Furthermore, a more prominent effect in temperature gradient change occurs when a small amount of energy is consumed during the state transition process.

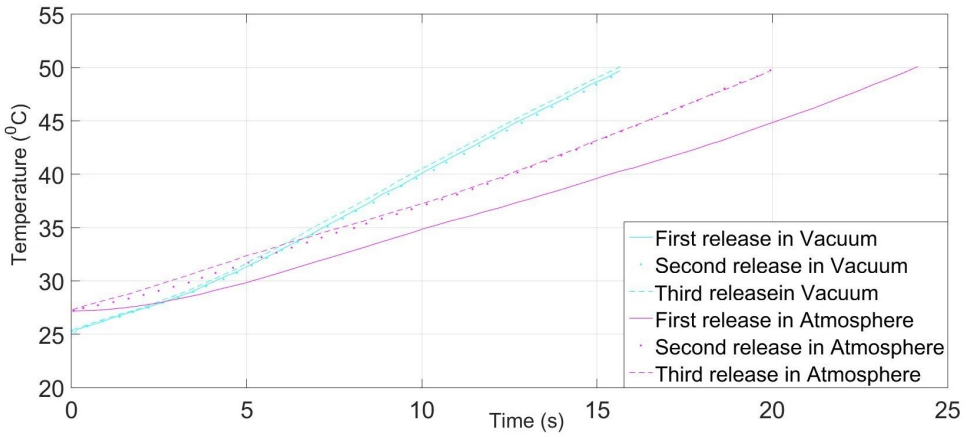

Figure D.4 Temperature rise recorded in the release nitinol circuit in vacuum and atmosphere. Three release actions were conducted in both environments.

In Fig D.5 we extracted the data set for the temperature gradient of the capturing circuit (C-circuit) in vacuum and highlighted the differences between two gradients marked as G_1 and G_2. G_1 represents the temperature gradient of the nitinol wires in the Martensite state where minor shape restoration occurs before the activation temperature (30°C) and G_2 is the temperature gradient above activation temperature in the Austenite state during which the shape restoration occurs. The average gradient of G_1 is 1.71 °C/sec and 2.15 °C/sec for G_2. The difference between G_1 and G_2 is 0.44 °C/sec.

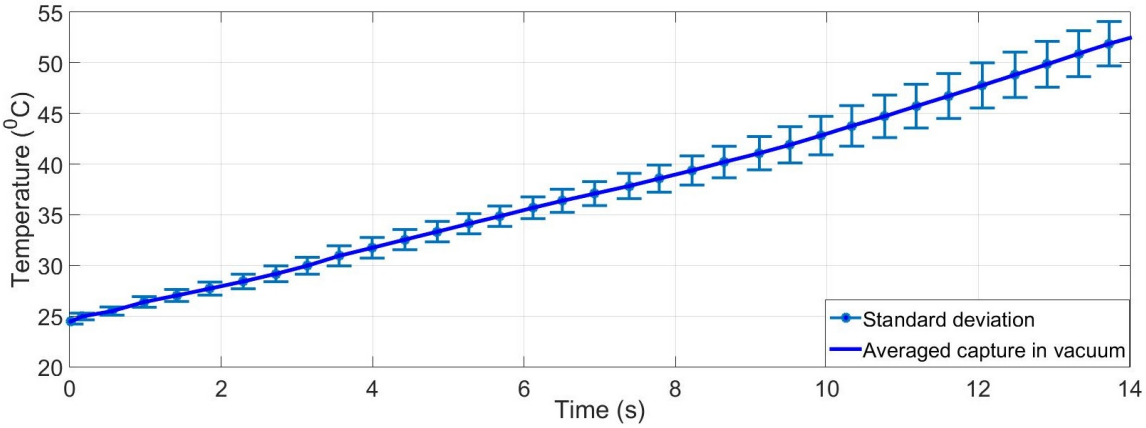

Figure D.5 Temperature rise of the C-circuit in Vacuum. The nitinol starts heating up in the Martensite state with gradient G_1. At 3.71 seconds, the transition temperature is reached and the nitinol begins to transform to the Austenite state with a temperature gradient G_2.

In Fig D.6 we extracted the data set for the temperature gradient of the release circuit (R-circuit) in vacuum and determined another two gradients marked as G_3 and G_4. G_3 represents the average temperature gradient of nitinol wires in Martensite state where minor shape restoration occurs before activation temperature (30°C) and G_4 is the averaged temperature gradient above activation temperature in Austenite state during which the

pre-programmed shape restoration occurs. The average gradient G_3 is 1.14 °C/*sec* and the average gradient G_4 is 1.75 °C/*sec* for G_4. The difference between G_3 and G_4 is 0.61 °C/*sec*.

Our data shows that the temperature of the nitinol wires increases at a higher rate after the activation temperature is reached. The increment in temperature gradient after the activation temperature is an average of 0.5 °C/*sec*. The slight difference of 0.17 °C/*sec* in temperature measurement between the C-circuit and the R-circuit could be due to the different patch surface areas between thermocouples K1 and K2 glued onto the C-circuit and R-circuit, respectively.

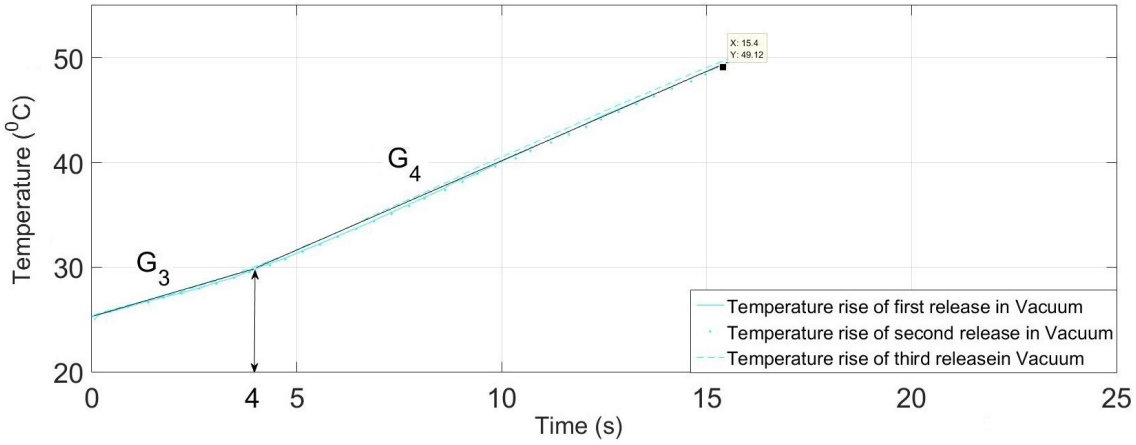

Figure D.6 Temperature rise of R-circuit in Vacuum. The nitinol starts heating up in the Martensite state with gradient G_3. At 4 seconds, the transition temperature is reached and the nitinol begins to transform to the Austenite state with a temperature gradient G_4.

D.4 Temperature rise vs. input voltage and current

In this section we describe two data sets comparing temperature rise in vacuum and atmosphere with respect to input current supplied, as shown in Figure D.7. The aim of these tests was to obtain a clear insight into the thermal behaviour of the capture and release nitinol circuits with respect to input power supplied to those circuits.

Figure D.7 shows that lower voltage and current was required in vacuum for the capturing nitinol to reach the transition temperature at 30 °C. In a vacuum the C-circuit took 14 seconds of continuous current supply to rise from 25°C to 50°C, and in an atmospheric environment it took 18 seconds. The energy required to operate MEDUSA in vacuum was 700 joules, compared to 900 joules required to complete the same operation in atmosphere.

A second observation made in the vacuum test data was that the temperature continued to rise for another 2 seconds after the input current was switched off, which resulted in an additional 8°C rise in nitinol temperature. This could be due to a lag in thermocouple response. The same phenomenon was observed in atmospheric test data where the temperature increased by 2°C after the input current was switched off.

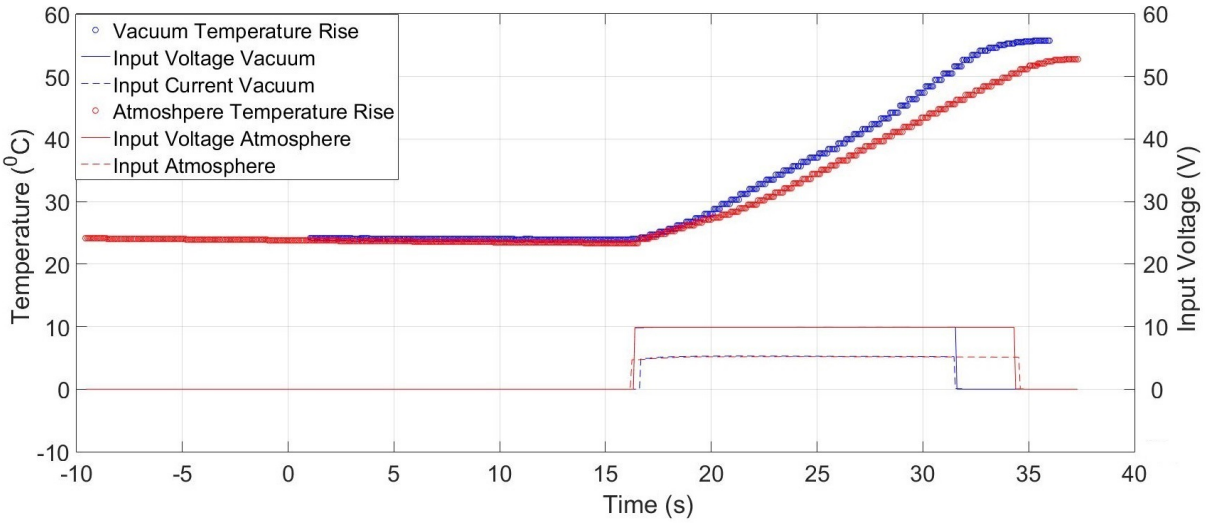

Figure D.7 Temperature rise of the capture nitinol in vacuum and atmosphere for an input voltage at 9.89V and an input current of 5.2A.

D.5 Temperature decay measurements in vacuum and atmosphere

In this section, we discuss two data sets comparing the temperature decay in the nitinol from 50 °C to 25 °C in order to determine the cool-down time needed between switching functionalities from capture mode to release mode, or vice versa.

According to the test results shown in Figure D.8 and Figure D.11, the average time taken for the capture nitinol to reach 25°C from 50°C was approximately 200 seconds in atmospheric conditions and 250 seconds in vacuum. The release nitinol took 150 seconds in atmosphere and 300 seconds in vacuum. The prolonged temperature decay period in vacuum is due to the absence of convective cooling in vacuum.

One can clearly see a change in the declining temperature gradient in both the C-circuit and R-circuit. For the C-circuit in vacuum, T_{V1} in Figure D.9 shows the interval during which the nitinol transitions from the Austenite state A_f back to the Martensite state M_s. For the C-Circuit in atmosphere, T_{A1} in Figure D.10 shows the same interval of state transition.

For the R-circuit in vacuum, T_{V2} in Figure D.12 shows the duration of the state transition from A_f to M_s. The same phenomenon for the R-circuit in atmosphere is denoted as T_{A2} in Figure D.13.

To further understand the temperature decay in a vacuum environment, a detailed analysis of temperature decay in vacuum through radiation is discussed in Section D.6.

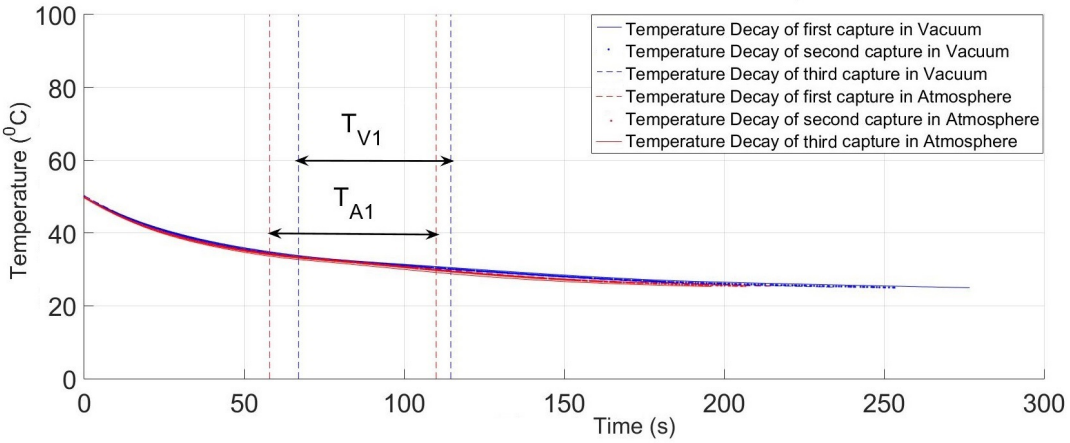

Figure D.8 Temperature decline of the C-circuit in vacuum and atmosphere right after a capture action has completed. T_{V1} denotes the temperature range during the transition from the Austenite state A_f to the Martensite state M_s in vacuum. T_{A1} denotes the temperature range during the transition from the Austenite state A_f to the Martensite state M_s in atmosphere.

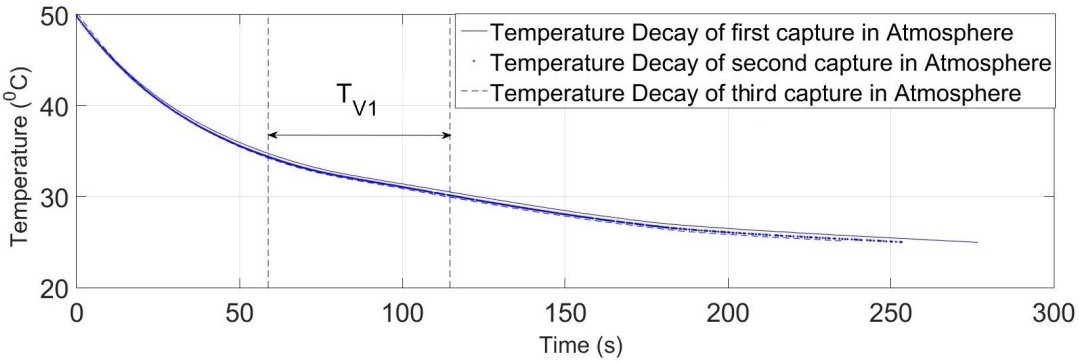

Figure D.9 Temperature decay recorded following three capture motions in vacuum. T_{V1} lasts 52 seconds from 34 °C to 30 °C.

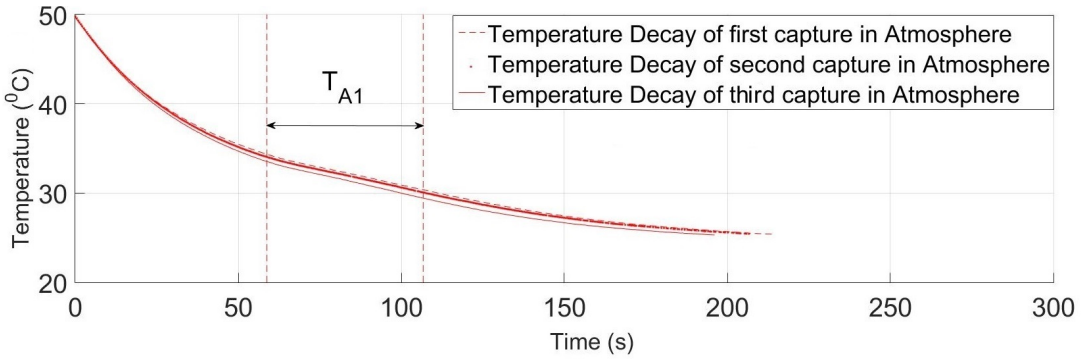

Figure D.10 Temperature decay recorded following three capture motions in atmosphere. T_{A1} lasts 47 seconds from 34 °C to 30 °C.

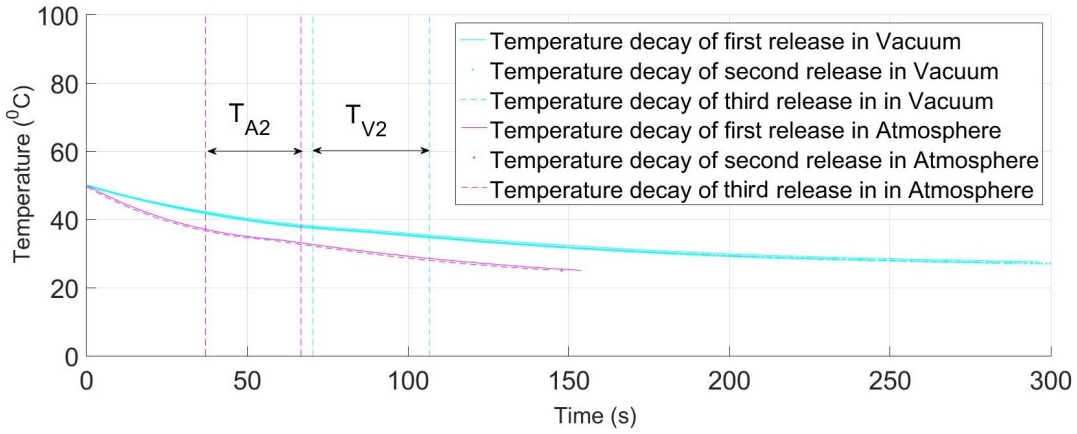

Figure D.11 Temperature decay of the R-circuit in vacuum and atmosphere right after a release action has completed. T_{V2} denotes the temperature range during the transition from the Austenite state A_f to the Martensite state M_s in vacuum. T_{A2} denotes the temperature range during the transition from the Austenite state A_f to the Martensite state M_s in atmosphere.

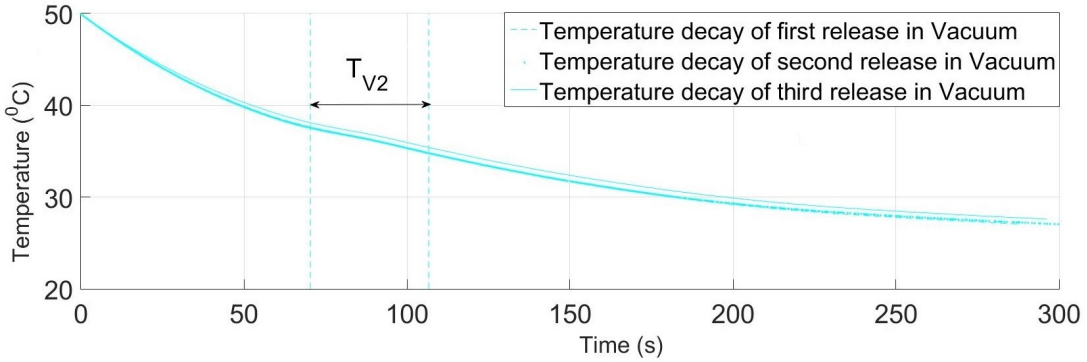

Figure D.12 Temperature decay recorded following three release motions in vacuum. T_{V2} lasts 37 seconds from 37 °C to 34 °C.

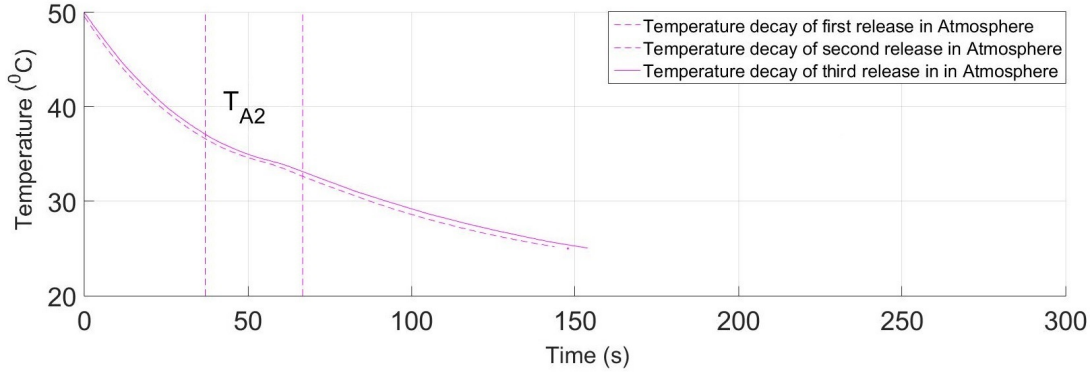

Figure D.13 Temperature decay recorded following three release motions in atmosphere. T_{A2} lasts 28 seconds from 37 °C to 34 °C.

D.6 An investigation into MEDUSA temperature decay in vacuum through radiation

Since MEDUSA relies on electrically induced heating of the nitinol wires in the arms, heat exchange with the surrounding environment is an important factor that must be taken into consideration. In an atmospheric environment heat is transported by three effects: conduction, convection and radiation. Heat exchange via convection with ambient particles does not occur in a vacuum due to the absence of particles needed for transmission. Radiation is thus the main mode of heat exchange. In this section we consider heat transport via radiation in a vacuum and derive an expression for temperature change as a function of time and the material properties of nitinol.

D.6.1 Radiation heat flux density

Temperature decay in nitinol due to radiation follows the Stefan-Boltzman law and is expressed as $\dot{q} = \sigma.T^4$. The radiation heat flux density denoted as $\dot{q}$ in Equation D.1 equates the radiation energy dissipated by a two-dimensional area per second and the rate at which this is occurs depends on nitinol surface temperature and its emissivity. The total radiated power is thus given by

$$\dot{q}.A = \sigma.\epsilon.A.T^4 \tag{D.1}$$

Where $\dot{q}$ stands for radiated heat flux density which is a function of surface temperature (T) of nitinol measured in Kelvin. The unit for $\dot{q}$ is watt per square meters $[W/m^2]$. A is the surface area of nitinol used, in this case it is 0.0465 square meter over 1.5 meters of nitinol wires used.

The definition of emissivity ϵ in Equation D.1 is a numerical value describing the effectiveness of a material in emitting energy as thermal radiation. Emissivity typically ranges from 0 (perfect white body) to 1 (perfect black body). Most organic and oxidized surfaces have emissivity values close to 0.95. A series of experiments by Song et al. [34] found that the emissivity of nitinol is 0.66 at 50^0C.

D.6.2 Heat balance equation of MEDUSA in vacuum

During operation of MEDUSA in vacuum, the input current supplied to the nitinol makes it a heat source and the temperature slowly decreases after a capture or release action has completed. A cool-down time is required to allow heat exchange between nitinol and the ambient environment in order for temperature to decay from 53°C to 25°C, which is below the transition temperature. The heat balance in the nitinol is defined by the heat loss through radiation to the ambient environment and the heat gained from radiation impinging on the wire from the ambient environment.

The heat loss per unit volume $[\frac{W}{m^3}]$ is given by:

$$\alpha(T) = \frac{-2.\epsilon.\sigma.T^4}{r} \tag{D.2}$$

where T is the surface temperature of the wire and the negative sign denotes heat loss.

The heat gain per unit volume $[\frac{W}{m^3}]$ is given by:

$$\beta = \frac{2.\epsilon.\sigma.T_0^4}{r} \tag{D.3}$$

where T_0 is the ambient temperature, which is set at 298 Kelvin in this analysis.

The resultant temperature change of the nitinol associated with its material characteristics is denoted as: γ. Where ρ is the density of nitinol used, C_p is the specific heat of nitinol and the resultant temperature gradient $\frac{dT}{dt}$ is end product we wish to attain. The derived $\frac{dT}{dt}$ is used in simulation results and compared to measurement data from the vacuum test shown in Figure D.14.

$$\gamma = \rho.C_p.\frac{dT}{dt} \tag{D.4}$$

The resulting heat balance is thus given by:

$$\rho.C_p.\frac{dT}{dt} = \frac{-2.\epsilon.\sigma.T^4}{r} + \frac{2.\epsilon.\sigma.T_0^4}{r} \tag{D.5}$$

Table D.1 *Parameters used in equation D.5.*

Parameters	**Definition**	**Value**	**Unit**
ρ	Density of Nitinol	6500	$\frac{kg}{m^3}$
C_p	Specific Heat of Nitinol	320	$\frac{J}{kg.K}$
$\frac{dT}{dt}$	Temperature Gradient	Function of Time	$\frac{K}{s}$
σ	Stefan-Boltzmann Constant	$5.670367 \cdot 10^{-8}$	$\frac{W}{m^2.K^4}$
ϵ	Emissivity	0.66	No Unit
r	Radius of Nitinol Used	0.005	m
T_0	Background Temperature	298	K

Integrating equation D.5 allows us to obtain an equation for the temperature of the wire as a function of time. Figure D.14 shows the theoretically determined temperature curve as a function of time compared to data obtained in vacuum tests.

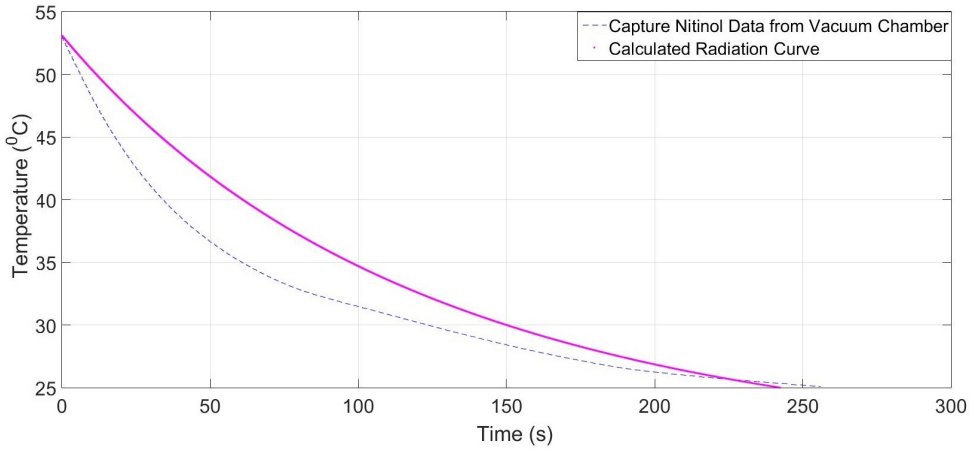

Figure D.14 Comparison between theoretical calculations and experimental data of temperature decay of nitinol in vacuum. Capture nitinol data obtained from the vacuum test was used to compare with values derived from Equation D.5.

According to Figure D.14 the two curves started at the same temperature and took approximately the same time to reach 25°C from 53°C. This agreed with the hypothesis stated earlier that radiation is the main effect of heat exchange in a vacuum. Also, calculations based on heat flux density had similar results to vacuum test data, which adequately described the temperature behaviour during decay.

However, the two curves did not match with the measured temperature being consistently lower than predicted by theoretical curve. The deviation between the two can be explained by two factors. Equation D.5 did not include the energy consumption during the state transition from the Austenite state A_f to the Martensite state M_s. Moreover, Equation D.5 did not include a factor that represents thermal conduction between the heated nitinol and the polyamide body of the arm.

In order to improve the match between theory and experiment our heat balance equation should incorporate terms addressing these two factors.